DIAGNOSING HIGH SINUOSITY REGIMES ASSOCIATED WITH ANOMALOUS GREENLAND ICE-MELT EVENTS USING SELF-ORGANIZING MAPS

By

Mansour El Riachy

A Thesis

Submitted to the University at Albany, State University of New York

in Partial Fulfillment of

the Requirements for the Degree of

Master of Science

College of Arts & Sciences

Department of Atmospheric and Environmental Sciences

May 2021

ABSTRACT

Sinuosity, a metric that describes the waviness of the circumpolar flow, is adapted to quantify modification of the tropospheric polar vortex within longitudinal sectors by localized incursions of warm, moist air from middle latitudes associated with Arctic cyclones (ACs). In this thesis, we identify four corridors of high AC track frequency, on which we center 90° longitudinal sectors comprising the following regions: Pacific, West of Greenland, Atlantic, and Asian. Sectorial sinuosity is calculated for the West of Greenland sector and is used to quantify the amplitude of the 300-hPa flow associated with anomalous Greenland ice-melt events.

A climatology of ACs was constructed for the 1979–2018 period using the cyclone climatology constructed by Sprenger et al. (2017) to identify favorable longitudinal corridors characterized by a high frequency of ACs tracking into the Arctic from middle latitudes. A sectorial sinuosity climatology was constructed for the 1979–2018 period using the European Centre for Medium-Range Weather Forecasts reanalysis ERA-Interim dataset to quantify disruptions of the tropospheric polar vortex according to sector for the equatorward boundary of the tropospheric polar vortex defined by a threshold geopotential height contour on the 300-hPa surface. A climatology of 129 anomalous Greenland ice-melt events is constructed that comprises events having a standardized anomaly in sigma units of +1 that last 3 or more days during April–October 1979–2018 from data taken from the National Snow and Ice Data Center. Characteristic 300-hPa geopotential height patterns associated with anomalous Greenland ice-melt events are identified using self-organizing maps (SOMs) constructed from ERA-Interim reanalysis data.

A thermal metric and a precipitable water metric are calculated by taking area-averaged values of the standardized 700-hPa temperature anomaly and the standardized precipitable water anomaly, respectively, for a domain over Greenland for 942 days with ice melt greater than or equal to +1 standard deviation of Greenland ice melt. The thermal metric is used to link 300-hPa geopotential height patterns to 700-hPa temperature patterns. The precipitable water metric is used to link 300-hPa geopotential height patterns to vertically integrated water vapor patterns. Events at the 10th percentile and 90th percentile of the standardized Greenland ice-melt anomaly are identified. Two lists of dates corresponding to the starting day of events from the 10th percentile and events from the 90th percentile of the standardized Greenland ice-melt anomaly were created. One event from each list was randomly selected as a representative case study. Two events from the lower and upper 10th percentiles are randomly selected: the 5–7 June 2009 event and the 9–15 April 2016 event, respectively. Both events are analyzed according to the evolution of the amplitude of the flow quantified in terms of sectorial sinuosity and interpreted in terms of the QG geopotential height tendency forcing.

Characteristic synoptic patterns identified using SOMs show that flow regimes conducive to anomalous Greenland ice-melt events vary from a strong trough upstream of Greenland to a strong ridge over Greenland. Events at the 10th percentile of standardized Greenland ice-melt anomaly occur during the warmer months (i.e., June, July, and August) of the ice-melt season with the exception of one event occurring in October. Events that fall into the 90th percentile of standardized Greenland ice-melt anomaly occur during the colder months (i.e., April, May, September, and October) of the ice-melt season with the exception of one event occurring in July

and one event occurring in August. Positive mean values of the thermal metric are higher for events at the 90th percentile than for events at the 10th percentile.

A diagnosis of the 300-hPa QG geopotential height tendency forcing for the two selected events show that ridge amplification over Greenland is dominated by geopotential height tendency forcing due to the differential advection of temperature by the geostrophic wind that is associated with poleward-directed warm-air advection. Geopotential height tendency forcing due to the advection of geostrophic absolute vorticity by the geostrophic wind plays a subordinate role. The main difference between the two events lies in the magnitude of the thermal advection and the value of the thermal metric. The 9–15 April 2016 event from the 90th percentile of standardized Greenland ice-melt anomaly events was associated with stronger poleward-directed warm-air advection compared with the 5–7 June 2009 event. The 9–15 April 2016 event also was associated with a higher thermal metric value and larger standardized 700-hPa temperature anomaly compared with the 5–7 June 2009 event from the 10th percentile of standardized Greenland ice-melt events. The larger standardized 700-hPa temperature anomaly over Greenland for the 9–15 April 2016 event may be attributed to stronger thermal advection. The stronger thermal advection was occurring ahead of two poleward-moving surface cyclones upstream of Greenland concurrent with a 700-hPa ridge over southeastern Greenland that is enhancing the poleward transport of warm air. Weaker poleward transport of warm air concurrent with a 700-hPa ridge centered over southeastern Greenland was occurring ahead of one surface cyclone for the 5–7 June 2009.

ACKNOWLEDGEMENTS

I would like to thank my co-advisors, Drs. Dan Keyser and Lance Bosart for their advisement throughout my graduate school experience. Their input throughout this experience was crucial to my growth as a scientist and as a communicator. I appreciate the opportunities they provided me with to present at numerous conferences. Dan and Lance are passionate scientists and teachers, and I am proud to have had the opportunity to attend their classes. I have learned a lot from them.

I wish to show my gratitude to the faculty members in the Department of Atmospheric and Environmental Sciences at the University at Albany for the unique educational experience, for their efforts in providing us with a high-quality learning experience, and for always being available for outside class discussions. A special thank you to Annette Audi, Barbara Zampella, Ashley Turski, Carolyn DeLuise, and Chaina Porter for their administrative support. I would also like to recognize Kevin Tyle for the vital 24/7 technical assistance on which this M.S. work depended.

I would like to thank all my fellow graduate students and colleagues for their companionship and support. I would especially like to thank my friends and housemates Mike Main, Cameron Paquette, and Mathew Vaughan for all the great conversations, meals, and laughs shared under one roof. To my friends from the undergraduate years especially Leann Anthony, Josie Crouch, Michael Muhlhausen, and Mathew Brewer it would not have been the same without you. To the special people I met in graduate school, Minghao Zhou, Kevin Biernat, Emily Paltz, Rebecca Orrison, Ernesto Tejedor, Nathalia Ruiz, Peyton Capute, and Jeremiah Otero Piersante I am grateful for your invaluable friendship, for the shared memorable moments, for your scientific and moral support through challenging times, and cheers to the great times spent together.

I am indebted to a mentor of the highest order that I have met along the way. Dr. Ryan Torn has been a tremendous influence in guiding me to become a better scientist and in bringing out the best in me as a person. He has gone above and beyond in fulfilling his role as my professor and my mentor, in being present to collaborate with me since my undergraduate school experience, in believing in me as a student, in guiding me to grow as a person, and in helping me realize my potential. I am grateful for his companionship and friendship in my journey here at SUNY Albany, and I am honored to call him my mentor.

A special thank you goes to my loving family. Despite the long distance separating us, they have been present and supportive from day one. They provided me with unconditional love and motivation all throughout my journey to pursue my studies abroad and to follow my passion in becoming a meteorologist. To that I will forever be grateful.

I would like to thank Dr. Jonathan E. Martin for providing the sinuosity calculation code that made this research possible.

This research was supported by the Office of Naval Research (ONR) grant N00014-18-1-2200, awarded to the University at Albany, SUNY.

Mansour El Riachy

Albany, New York

May 2021

TABLE OF CONTENTS

LIST OF FIGURES

1 Introduction

1.1 Motivation

In recent decades, the Arctic region has been gaining more attention as warming has increased at a faster rate relative to the rest of the globe (Screen et al. 2010). This greater warming at higher latitudes compared with lower latitudes, or Arctic amplification, is associated with Arctic–midlatitude flow interactions and an increase in cyclone-related incursions of warm, moist air from middle latitudes into the Arctic. These incursions of warm, moist air into the Arctic are associated with increased reductions in snow and ice cover, which contribute to increased water vapor content, changes in cloud cover, and enhanced warming in the lower troposphere. This warming is suggested to be reinforced by a positive ice–temperature feedback emerging in the Arctic region, as discussed by Screen et al. (2010), where the increased reduction of snow and ice cover in the Arctic has been substantial enough in the recent decades to enhance Arctic warming, which eventually increases the likelihood of more snow and ice melting. This feedback is thus influenced by the incursions of warm, moist air from middle latitudes that occur upstream of high-latitude ridges, and in highly amplified flow patterns superimposed with enhanced low-level baroclinicity across locations in the Arctic where horizontal gradients of heat and moisture fluxes may be found. These flow patterns culminate in high-latitude blocking and Rossby wave breaking (RWB) and are sometimes associated with Arctic cyclones (ACs), which are synoptic-scale features that are often responsible for warm-air incursions.

The frequency of blocking events is associated with extreme weather in middle latitudes and amplification of large-scale Rossby waves, as discussed in Barnes et al. (2015), is one cause of

enhanced Arctic warming resulting from a chain of events debated in the literature (e.g., Francis et al. 2012; Liu et al. 2012). The chain of events starts with enhanced Arctic warming that reduces the equator-to-pole temperature gradient at the surface which causes midlatitude winds and the jet stream to slow down and shift equatorward. This slowing down of the jet stream eventually leads to amplified large-scale Rossby waves or flow patterns in the meridional direction and an increase in the frequency of blocking events. Amplified flow patterns are usually associated with extreme weather in the Northern Hemisphere mid-latitudes and incursions of warm, moist air and into the Arctic. Flow amplification and incursions of warm, moist air into the Arctic can result in longitudinally varying horizontal temperature gradients that are associated with disruptions of the tropospheric polar vortex and can occur within preferred longitudinal corridors.

In this study, we identify four corridors of high AC track frequency, on which we center 90° longitudinal sectors: Pacific, West of Greenland, Atlantic, and Asian. We then use sinuosity, a metric that describes the waviness of the circumpolar flow, to quantify tropospheric polar vortex modification by localized incursions of warm, moist air from middle latitudes that are associated with the aforementioned amplified flow patterns and ACs. To quantify modifications within longitudinal sectors, we introduce sectorial sinuosity, which is calculated for the identified 90° longitudinal sectors. Modifications of the tropospheric polar vortex in the West of Greenland sector sometimes culminate in ridging over Greenland associated with poleward directed warm-air surges that may have a large impact on the Greenland ice sheet (GrIS). This impact on GrIS motivates us to focus on the West of Greenland sector, where we diagnose the influence of disruptions of the tropospheric polar vortex on the synoptic flow regime. We use sectorial sinuosity to quantify flow amplitude during synoptic flow regimes that are associated with anomalous

Greenland ice-melt events. Then we adopt self-organizing maps (SOMs) to identify characteristic synoptic patterns conducive to anomalous Greenland ice-melt events. SOMs implementation was programed using the minisom package (https://github.com/JustGlowing/minisom/). SOM's architecture allows for a reduced and ordered representation of high-dimensional datasets by a smaller set of variables (Oliveira et al. 2020). In other words, SOMs is a type of artificial neural network that converts high-dimensional data items into low-dimensional display by clustering data items into nodes or categories according to the similarities between these data items.

1.2 Literature review

1.2.1 Incursions of warm, moist air into the Arctic

The important role that moisture intrusions from lower latitudes play on Arctic circulations has been extensively discussed in the literature. Woods et al. (2013) analyzed the large-scale circulation patterns associated with intense moisture intrusions into the Arctic and found that these intrusions are concentrated over the main sea and ocean basins across 70°N latitude, in the Labrador Sea, Atlantic, Barents/Kara Sea, and Pacific. At the time of maximum moisture intrusions, Woods et al. (2013) created composites of the large-scale circulation patterns shown in Fig. 1. Figures 1a–d indicate that a blocking pattern is evident in composites of potential temperature on the 2-PVU surface in association with a ridge of high potential temperature, indicative of the presence of an anticyclonic potential vorticity anomaly on the eastern flank of each sector. Figs. 1e–h display sea level pressure composites corresponding to the 2-PVU surface composites of potential temperature that show a low pressure system and a blocking high pressure system embedded in each sector during a moisture intrusion, both enhancing the poleward flow of moisture.

Springtime extreme events of moisture transport into the Arctic affect sea-ice concentrations and are also correlated with increased Arctic air temperature with a long-lasting surface temperature anomaly for up to two weeks (Yang et al. 2017). This surface temperature anomaly is due to the moisture flux into the Arctic, which is associated with anomalous downward longwave radiation at the surface and increased surface temperature leading to enhanced ice melt. Yang et al. (2017) also show how a high frequency of occurrence of blocking weather regimes, especially in the North Atlantic, is mainly responsible for extreme moisture transport into the Arctic from lower latitudes. The high frequency of occurrence of blocking weather regimes and moisture transport during springtime is related to sea-ice extent in late summer and early fall (Kapsch et al. 2013). This springtime moisture transport is associated with increased cloudiness in the Arctic region, which also amplifies the greenhouse effect and results in downward longwave radiation at the surface and increased ice melt. An indirect effect, discussed by Kapsch et al. (2013), consists of a decrease in the amount of shortwave radiation earlier in the season with increased cloudiness then an increase of shortwave radiation later in the season. This increased amount of shortwave radiation reaching the surface relative to the climatological mean is due to decreased surface albedo from increased ice melt. This creates an increased amount of positive shortwave radiation anomaly and would act to amplify ice melt later in the season.

Moisture transport into the Arctic is also tied to midlatitude dynamics: specifically, Rossby wave breaking (RWB). Cyclonic or anticyclonic, RWB can account for ~68% and ~56% of extreme poleward moisture transport by transients across 60°N in winter and summer, respectively, as shown by Liu and Barnes (2015). RWB in the troposphere is identified as overturning potential

temperature contours on the dynamical tropopause or the 2 PVU surface. When the overturning of potential temperature contours has a negative tilt, it is associated with Cyclonic wave breaking (CWB), and when the overturning of potential temperature contours has a positive tilt, it is associated with anticyclonic wave breaking (AWB). CWB is associated with extreme poleward moisture transport by transient disturbances southwest of Greenland and over the Bering Strait, whereas AWB is associated with extreme poleward moisture transport by transient disturbances over the Norwegian Sea, as shown in Fig. 2 (Liu et al. 2015). As mentioned in Liu and Barnes (2015), previous studies have shown that RWB occurrence is closely linked to the latitude of the eddy-driven jet; AWB (CWB) tends to occur more frequently when the eddy-driven jet is shifted poleward (equatorward) (e.g., Strong and Magnusdottir 2008; Woollings et al. 2008; Rivière 2011; Barnes and Hartmann 2012). CWB tends to occur downstream of a negatively tilted trough axis in the poleward exit region and cyclonic shear side of the jet, while AWB tends to occur downstream of a positively tilted ridge axis in the equatorward exit region and anticyclonic shear side of the jet (e.g., Martius et al. 2007; Strong and Magnusdottir 2008b; Barnes and Hartmann 2012; Bowley et al. 2019).

1.2.2 Modifications of the tropospheric polar vortex and amplified flow patterns

The opportunity for episodes of transient poleward transport of heat and moisture into the Arctic is created by modifications of the tropospheric polar vortex. Modifications of the tropospheric polar vortex attributed to blocking patterns associated with poleward moisture transport concurrent with RWB can culminate in flow amplification. Amplified flow patterns are manifested as amplified troughs and ridges in the 300-hPa geopotential height field, an example of which is the high-latitude ridge situated over Greenland on 12 April 2016 shown in Fig. 3. Ridge

amplification over Greenland on 12 April 2016 was associated with poleward-directed warm-air surges that culminated in a significant early season Greenland ice-melt event (Fig. 4). We are motivated to focus on the West of Greenland sector and quantify tropospheric polar vortex modification tied to Greenland ice-melt events and associated with ridging in the West of Greenland sector.

We will use sinuosity as a metric for quantifying flow amplitude and tropospheric polar vortex modification by warm, moist air intrusions: The sinuosity metric, illustrated in Fig. 5, is borrowed from geomorphology and is introduced as a means of quantifying the waviness of the mid-tropospheric flow using geopotential height contours on specified isobaric surfaces (Martin et al. 2016). We apply the sinuosity metric to the equatorward edge of the polar vortex as follows: The edge of the polar vortex is defined by specified geopotential contours, on the 300- or 500-hPa pressure levels, which typically lie within the core of the westerlies (Frauenfeld and Davis 2003).

1.2.3 Importance of Greenland ice sheet

The Greenland Ice Sheet (GrIS) has been extensively discussed in the literature as a major component of the Earth's cryosphere. The GrIS is a significant store of freshwater that may be intermittently released into the global ocean (Cullather et al. 2018). The GrIS also represents an example of a large area of land ice and snow that is important to consider when discussing global warming and climate change. Recent studies have indicated that the GrIS is experiencing a negative mass balance, with a recent acceleration in mass loss dominated by increased surface melt and corresponding runoff (e.g., Box et al. 2006; Mote 2007; van den Broeke et al., 2009; Fettweis et al. 2011; Hanna et al. 2013a, 2013b, 2014; Mioduszewski et al. 2016). Increased melting of land

ice can weaken the Atlantic Ocean overturning circulation (AMOC). The AMOC's speed depends on the balance between salt water and fresh water, with salt water being denser than fresh water, which renders the former easier to sink. Increased fresh water from increased land ice melt can alter the balance between salt water and fresh water and slow down the AMOC. This slowing down of the AMOC may impact temperatures around the North Atlantic (Velinga et al. 2002), which can affect global temperatures and sea level. Sherman et al. (2020) mention how rising temperatures is associated with land ice melt from the GrIS, which is a major contributor to global sea level rise of 0.33 mm yr^{-1} of the global 3.2 mm yr^{-1} from 1993 to 2010 (Vaughan et al. 2013). Shepherd et al. (2012) also state that GrIS has been a major contributor to global sea level rise in recent decades.

1.2.4 Drivers and mechanisms of GrIS melting

Drivers of GrIS melting analyzed from various studies in the literature are discussed in this subsection. Mioduszewski et al. (2016) demonstrate that the largest positive melt anomalies occur in concert with positive 700-hPa geopotential height anomalies near Greenland associated with wind, temperature, and humidity patterns indicative of strong poleward transport of heat and moisture. Cullather et al. (2018) states that the large-scale atmospheric circulation may produce increased surface ice melt by: 1) providing cloudless conditions that enhance solar radiation, 2) enabling the advection of warm air over the ice sheet, 3) enhancing moisture and cloud cover that increase downwelling infrared radiation and surface warming, and 4) by influencing turbulent fluxes and near surface winds.

1.2.5 Synoptic flow conducive to Greenland ice melt

Atmospheric circulation patterns have become more conducive to Greenland melt in the last decade as discussed by Mioduszewski et al. (2016), who also state that variations in summer melt are linked to the strength and frequency of anticyclonic-circulation and high-pressure patterns over Greenland and the North Atlantic (e.g., Mote 1998a, 1998b; Fettweis et al. 2011, 2013; Hanna et al. 2013a).

Mioduszewski et al. (2016) analyze increased poleward temperature advection at midlevels from characteristic 700-hPa and 500-hPa geopotential height patterns, and state that it appears to have served as the dominant driver of some of Greenland's record surface melt in recent years, particularly during 2007–2012 (e.g., Fettweis et al. 2011a; Hanna et al. 2013b, 2014; Neff et al. 2014). Mioduszewski et al. (2016) investigate the controls on summer GrIS surface melt from 1979 to 2014 by developing a synoptic climatology using SOMs of 500-hPa geopotential height derived from the Modern-Era Retrospective analysis for Research and Applications dataset.

Mioduszewski et al. (2016) were among the first to apply SOMs to investigate summer GrIS surface melt from a synoptic climatological perspective and to link identified 500-hPa geopotential height trends associated with summer GrIS surface melt to wind, temperature, and humidity at 700-hPa and at the surface. While Mioduszewski et al. (2016), among others, diagnose GrIS surface melt from a lower-tropospheric and surface perspective, in this thesis we focus on upper-tropospheric circulation patterns, and we classify Greenland ice-melt events into groups of flow amplitude using sectorial sinuosity.

Häkkinen et al. 2014 state that the negative phase of the North Atlantic Oscillation, with a high-pressure anomaly over the GrIS, has previously been implicated (Mote 1998) in enhancing surface melting of the GrIS. They defined large melt events to be when the daily Moderate Resolution Imaging Spectroradiometer (MODIS) standardized melt anomaly is stronger than +1 standard deviation, and low melting events to be when the daily MODIS standardized melt anomaly is less than -1 standard deviation. They constructed composite fields from the years 2000–2013 to show that large melt events are associated with a 500-hPa ridge centered over Greenland, which is flanked by troughs to the west and east (Fig. 6a) with relatively warm 500-hPa temperatures (Fig. 6b) that collectively resemble an omega block over Greenland. Low melt events are associated with a quasi-zonal flow over the ice sheet (Figs. 6c and 6d). The difference fields in 500-hPa geopotential height (Fig. 6e) and temperature (Fig. 6f) show areas that are at the 99% confidence level where both difference fields show a strong positive anomaly over Greenland.

In the scientific literature it is discussed how frequency and intensity of blocking anticyclones can influence the extent of surface melt. The June–July 2012 period of GrIS surface melt is one example where frequent and intense blocking anticyclones occurred. This period is analyzed, in particular, by McLeod and Mote (2015) who state that a series of exceptionally anomalous Greenland blocks that developed from the end of May until mid-July of 2012 contributed to an extreme melt event on 11–12 July in which surface melting was detected across approximately 98.6% of the GrIS (e.g., Nghiem et al. 2012; Tedesco et al. 2013; Hanna et al. 2014). McLeod and Mote (2015) labels a distinct class of North Atlantic cyclones as precursor cyclones and are extratropical cyclones originating to the west of Greenland blocks prior to the peak of blocking intensity. The study then states that enhanced surface melting during the summer, particularly

over southern and western Greenland, is strongly linked to the combination of adiabatic warming generated by subsiding air associated with blocking anticyclones and warm-air advection associated with precursor cyclones. Solomon et al. (2017) discuss the boundary layer–surface interactions on the GrIS during the July 2012 extreme melt event. They investigate cloud radiative effects and surface energy fluxes associated with surface ice melt. Solomon et al. (2017) show the importance of low-level liquid-bearing clouds not just for their direct radiative effect and enhancement of surface warming, but also for the indirect effect in reducing stratification from cloud top to the surface. This reduction in stratification from cloud top to the surface acts to homogenizes the cloud topped boundary layer and is explained by Solomon et al. (2017) to be a result of a combination of radiative heating of the surface, cloud-top radiative cooling, and cloud-driven turbulent mixing. Hahn et al. (2020) investigate the impact of high-pressure systems on Greenland cloud cover and ice melt. They show how anticyclonic circulations interact with Greenland topography to produce orographic lift and descent, which affect the response of cloud cover to blocking. As described by Hahn et al. (2020), blocking over Greenland induces anomalous upslope winds corresponding to anomalous ascent in northeastern Greenland and anomalous downslope winds corresponding to anomalous descent in southern Greenland. This anomalous vertical motion enhances cloud cover over northeastern Greenland, promoting increased cloud cover and longwave-driven warming and ice melt, whereas it reduces cloud cover over southern and western Greenland, promoting increased shortwave-driven warming and ice melt.

1.3 Research goals and thesis structure

1.3.1 Research goals

1. Identify favorable longitudinal corridors characterized by a high frequency of ACs tracking into the Arctic from middle latitudes.
2. Quantify disruptions within the identified longitudinal sectors of the tropospheric polar vortex by warm, moist air intrusions from lower latitudes using sectorial sinuosity.
3. Classify synoptic flow patterns conducive to anomalous Greenland ice-melt events into groups of flow amplitude quantified in terms of sectorial sinuosity.
4. Identify, for each group of flow amplitude, characteristic 300-hPa synoptic flow patterns conducive to anomalous Greenland ice-melt events using SOMs.
5. Diagnose the 700-hPa thermal and precipitable water characteristics over Greenland associated with anomalous Greenland ice-melt events.
6. Diagnose the disruptions by warm, moist air intrusions from lower latitudes of the tropospheric polar vortex during anomalous Greenland ice-melt events by computing the forcing terms in the QG geopotential height tendency equation.

1.3.2 Thesis organization

- Data and methodology
- Climatologies
- Case studies
- Summary

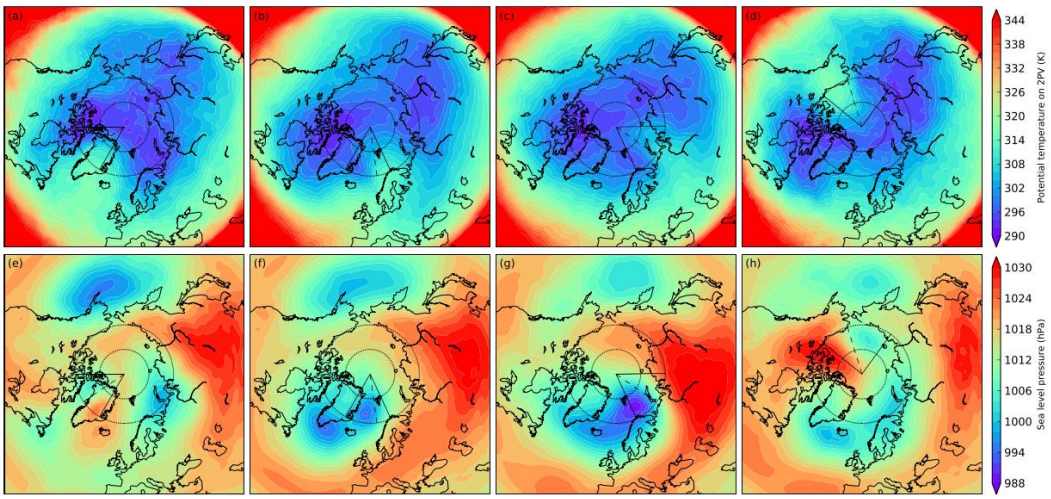

Fig. 1. Composites of potential temperature on the (a)–(d) 2 PVU surface and (e)–(h) sea level pressure at the time of maximum intensity for moisture intrusions occurring within each of the four sectors: Labrador [(a) and (e)], Atlantic [(b) and (f)], Barents/Kara [(c) and (g)], and Pacific [(d) and (h)]. Black lines show the sector boundaries. Dashed black lines indicate the median location of the moisture intrusions at maximum intensity. Dotted circles show latitude lines at 70°N and 80°N. [Figure 3 and caption adapted from Woods et al. (2013).]

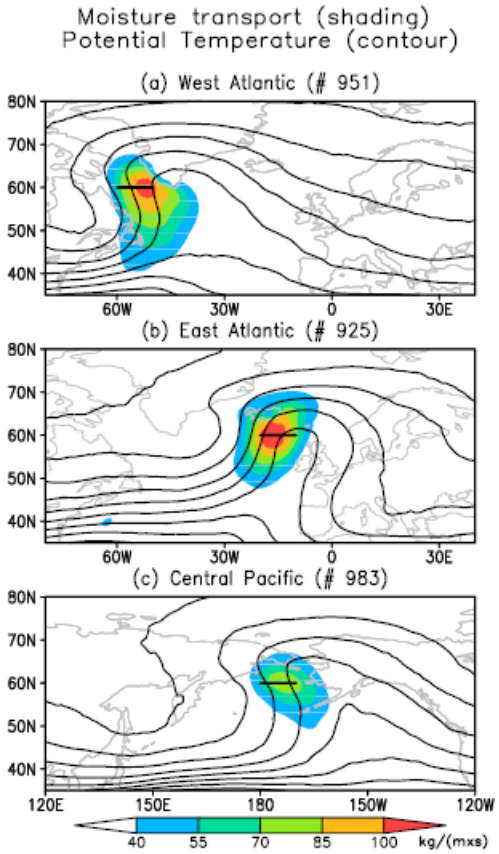

Fig. 2. Composite variables for extreme (greater than the 90th percentile) transient poleward moisture transport across 10° longitude bins at 60°N indicated by the black straight lines for the (a) West Atlantic (60°W–50°W), (b) East Atlantic (20°W–10°W), (c) central Pacific (180°W–170°W). The moisture transport is denoted by shading, and potential temperature on the 2 PVU surface is denoted by contours. The number of 6 h time steps in each composite is denoted in the title of each panel. [Figure 4 and caption from Liu et al. (2015).]

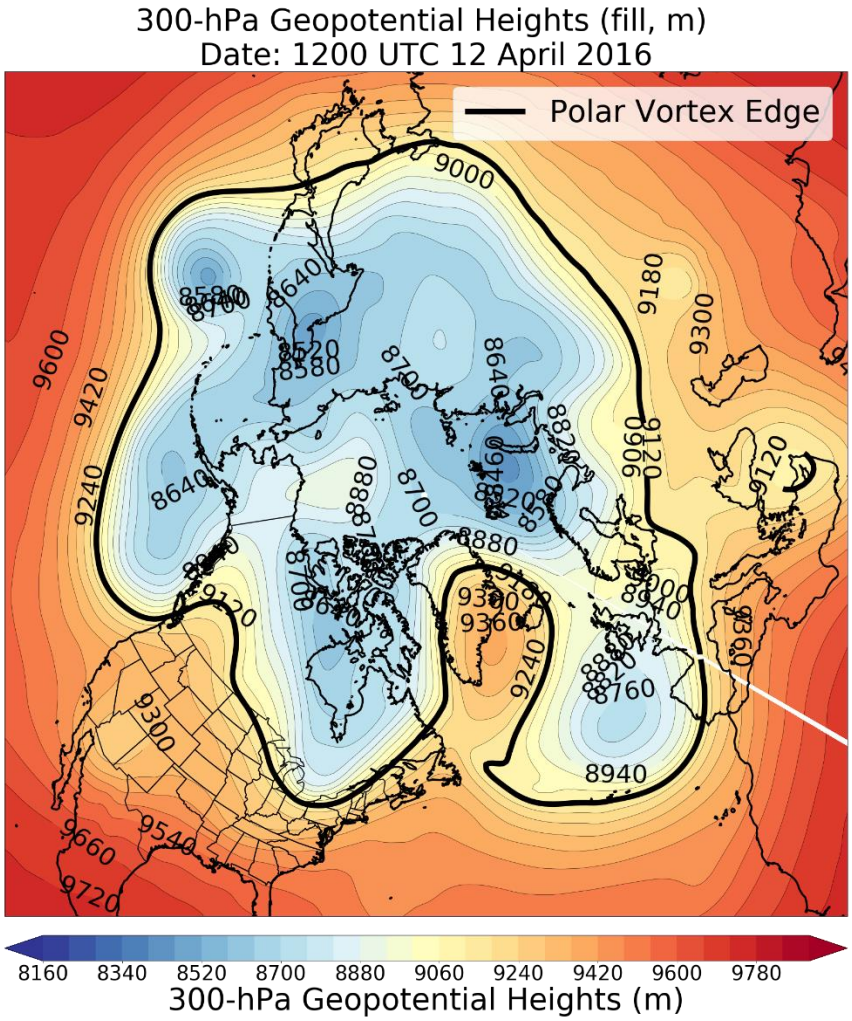

Fig. 3. 300-hPa geopotential height (fill, m) and polar vortex edge (thick black contour) for 1200 UTC 12 April 2016.

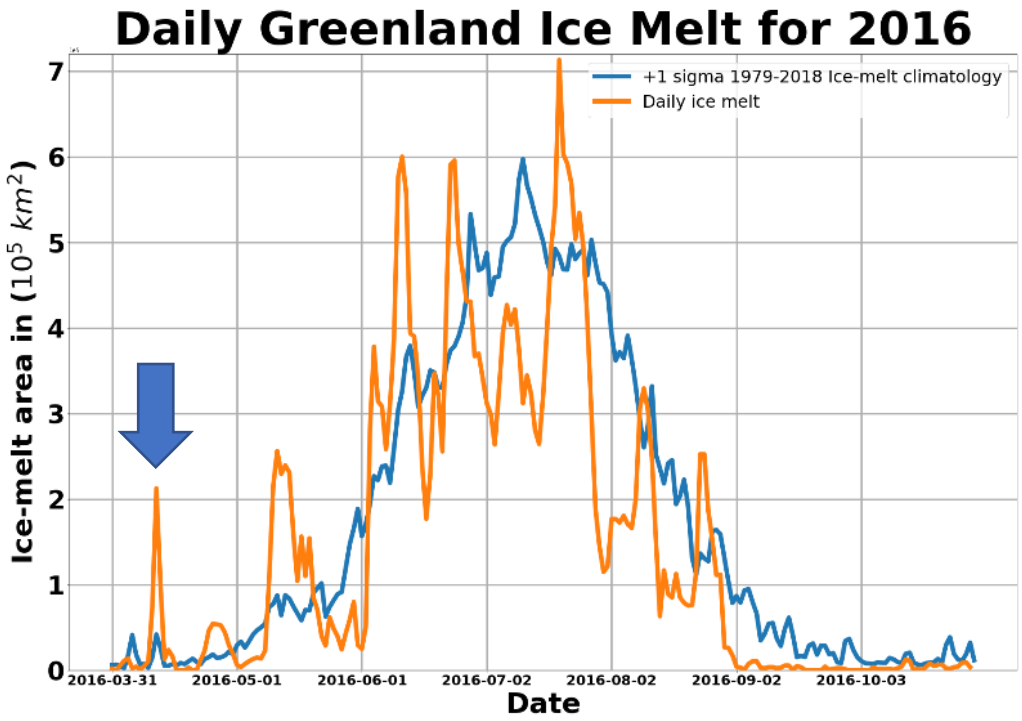

Fig. 4. Daily Greenland ice-melt data for 2016 (blue curve) and +1 sigma 1979–2018 ice-melt climatology (orange curve), Anomalous Greenland ice-melt event annotated (blue arrow)

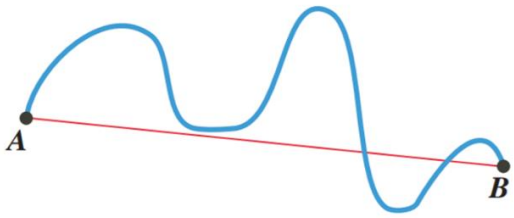

$$S_{AB} = \frac{\text{(Length of CONTOUR)}}{\text{(Length of SEGMENT)}}$$

Source: Martin et al. (2016)

Fig. 5. Schematic illustrating the sinuosity metric. S_{AB} is the ratio of the length of the blue contour to the length of the red line segment AB. [Figure 1 from Martin et al. (2016), and caption adapted from Martin et al. (2016).]

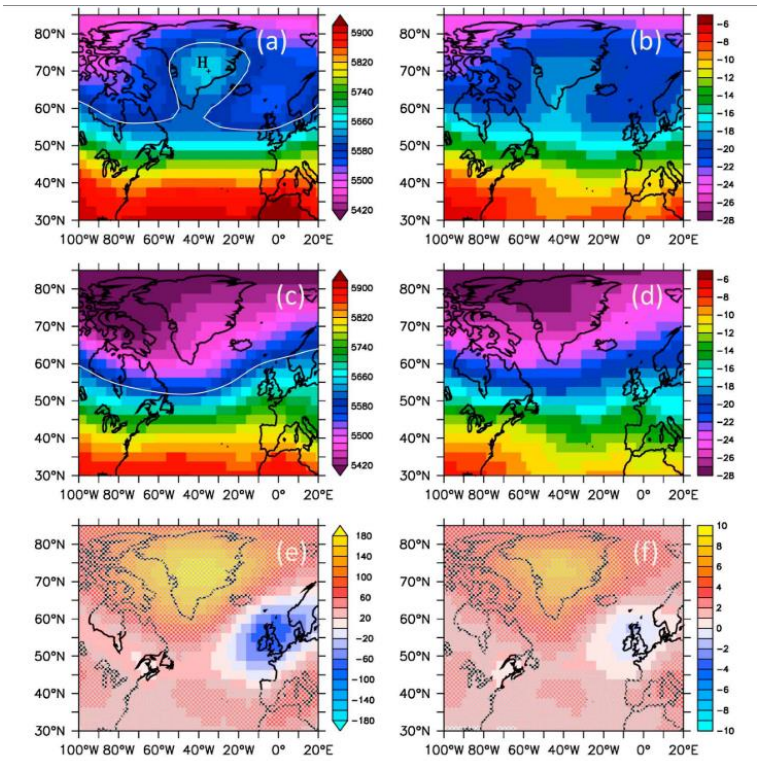

Fig. 6. The 2000–2013 composite of 500-hPa (a), (c), and (e) geopotential height (m) and (b), (d), and (f) temperature (°C) when the MODIS melt anomaly is greater than +1 standard deviation (a) and (b), and less than -1 standard deviation (c) and (d). The difference is shown in (e) and (f) for (a) minus (c) and (b) minus (d), respectively. In (a) and (c), the 5600 m geopotential height contour is drawn in white; also, in (a), a maximum geopotential height value of 5647 m is marked by the black plus sign. The cross-hatched values denote differences that are significant at the 99% confidence level. [Figure 3 from Häkkinen et al. (2014), and caption adapted from Häkkinen et al. (2014).]

2 Data and methodology

2.1 Favorable longitudinal corridors for AC tracking from middle latitudes into the Arctic

The first goal of this study is to identify favorable longitudinal corridors characterized by high frequency of ACs tracking into the Arctic from middle latitudes. In order to accomplish this goal, we start by constructing a climatology of ACs for the 1979–2018 period using the cyclone climatology constructed by Sprenger et al. (2017). Sprenger et al. (2017) use a novel method to derive a climatology of extratropical cyclones from sea level pressure (SLP) fields. The method is

applied to the six-hourly 40-yr European Centre for Medium-Range Weather Forecasts (ECMWF) Re-Analysis (ERA-40). The method consists of a procedure to identify individual cyclones and an algorithm to track the identified cyclones. Cyclone identification begins by determining the location of individual cyclone centers and their associated SLP minima. For every identified cyclone, an algorithm with an SLP contour interval of 2 hPa searches for the outermost SLP isobar enclosing the cyclone center. Finally, the area inside the outermost closed isobar surrounding each identified cyclone is determined. By adopting a definition that ACs are deemed to be extratropical cyclones that last 2 or more days and spend at least some portion of their lifetimes in the Arctic (>70°N), we extract AC dates and tracks from the Sprenger et al. cyclone climatology.

In this study, we choose ACs originating in middle latitudes (<70°N) and tracking into the Arctic. AC tracks are identified, and 90° longitudinal sectors are centered at locations of high AC track frequency. Four sectors are identified: Atlantic sector (1323 ACs, Fig 7), Asian sector (1013 ACs, Fig. 8), Pacific sector (626 ACs, Fig. 9), and West of Greenland sector (619 ACs, Fig. 10). An AC that originates or terminates outside of a given sector is associated with that sector if the longitude of the cyclone at 70°N falls 5° of longitude inward from the boundaries of that sector.

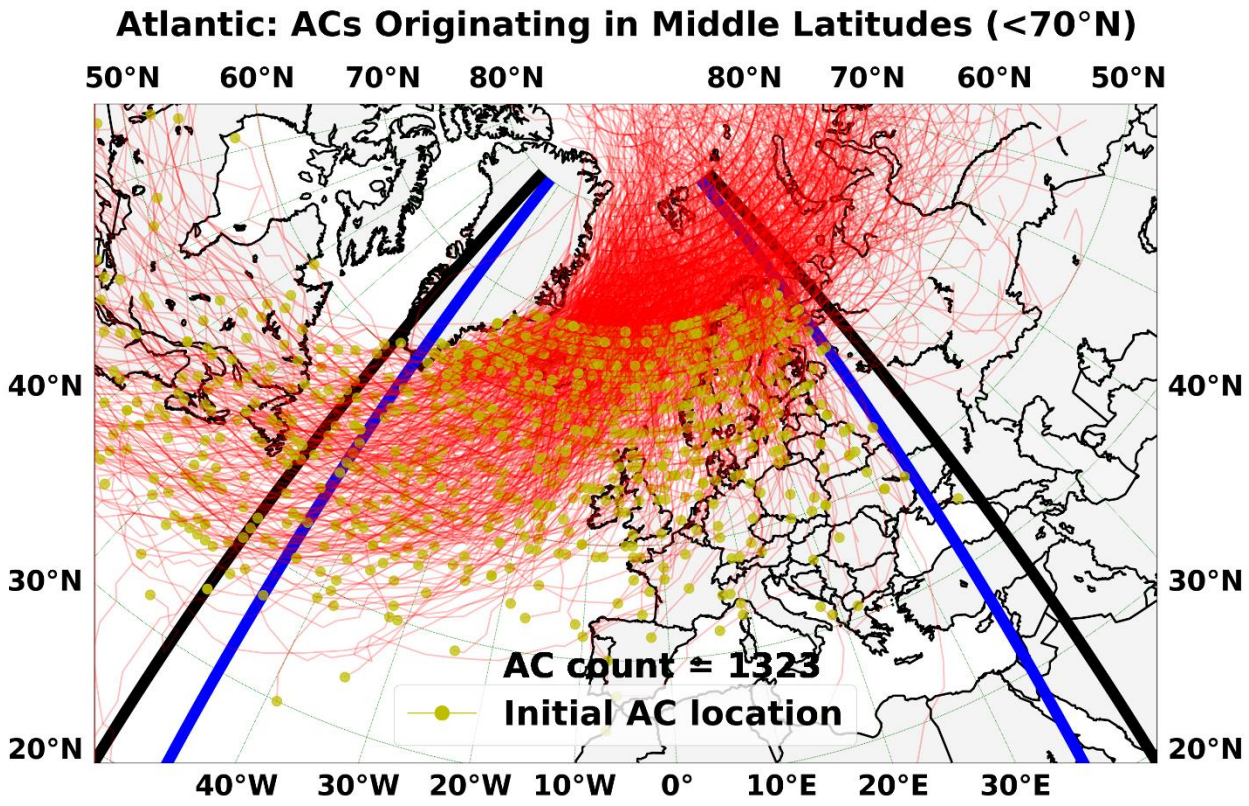

Fig. 7. Atlantic sector and associated ACs originating in middle latitudes (<70°N). Black lines denote sector boundaries and blue lines denote boundaries for choosing ACs that cross 70°N 5° of longitude inward from sector boundaries.

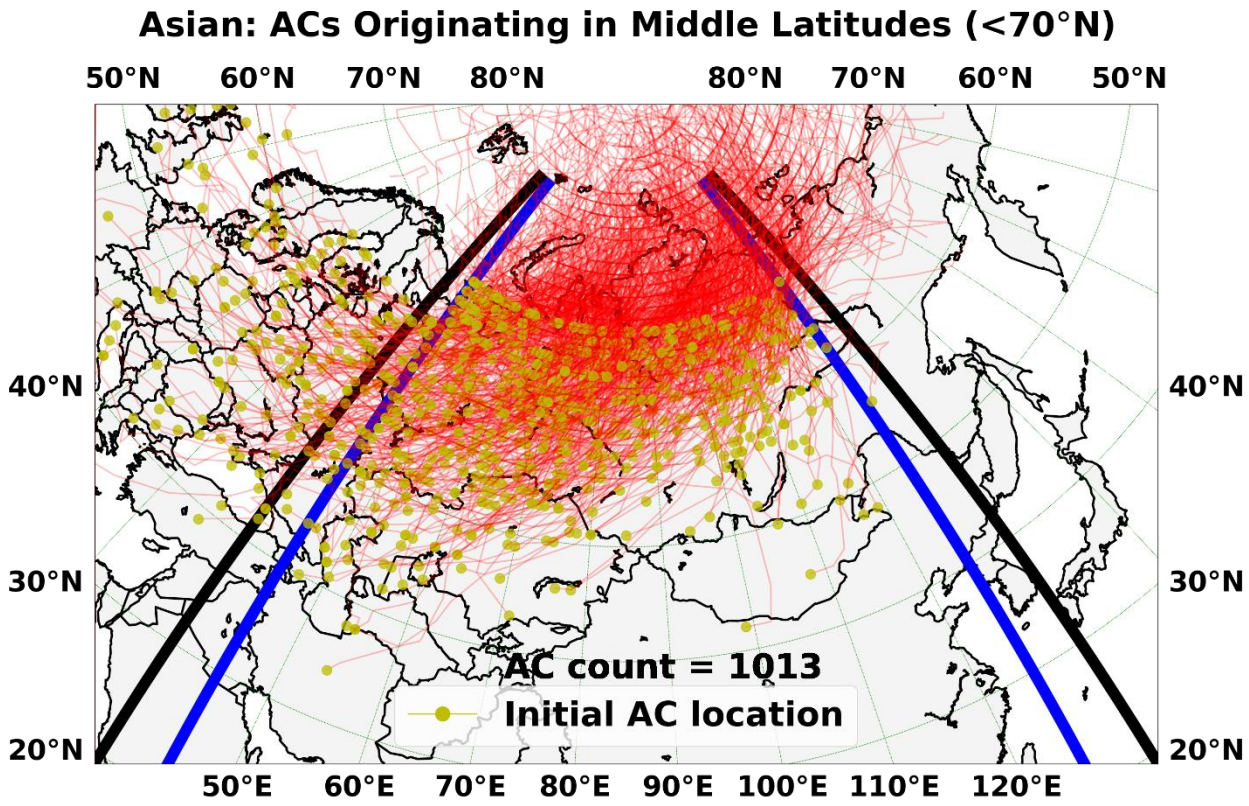

Fig. 8. As in Fig. 7 except for Asian sector.

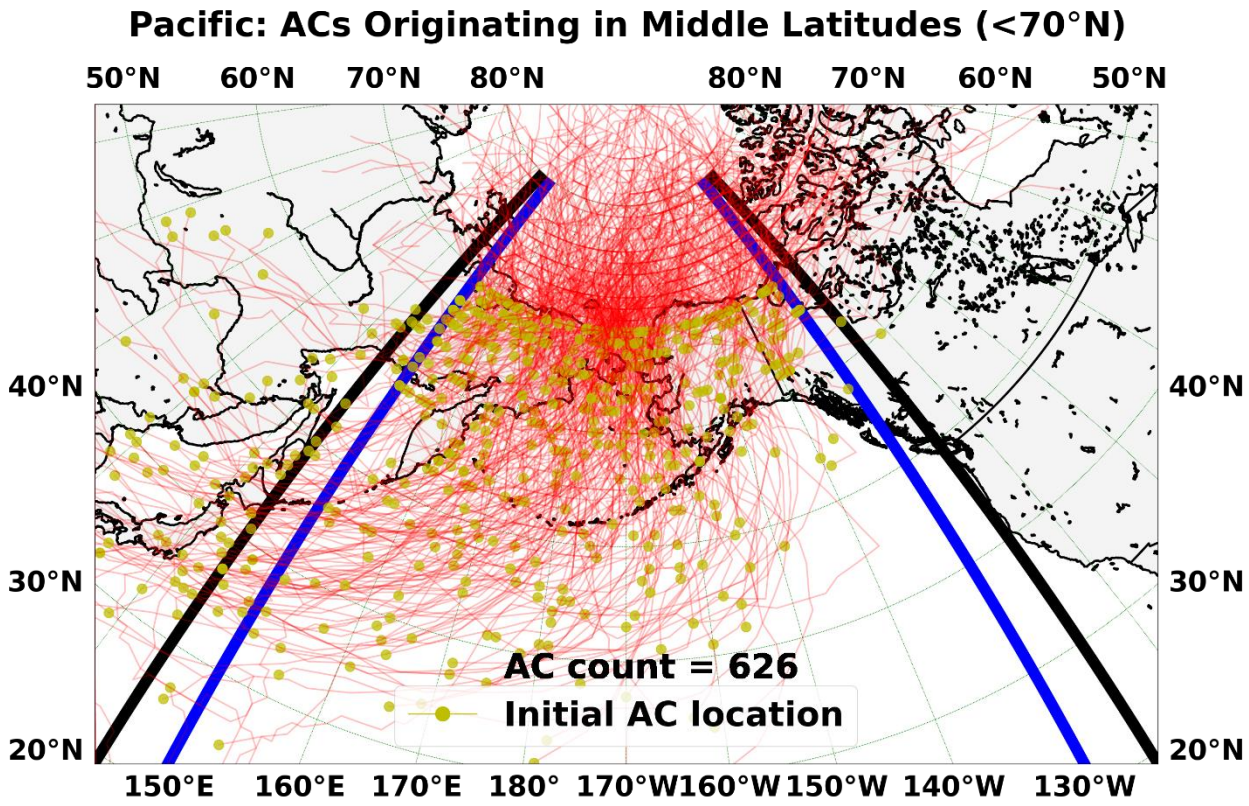

Fig. 9. As in Fig. 7 except for Pacific sector.

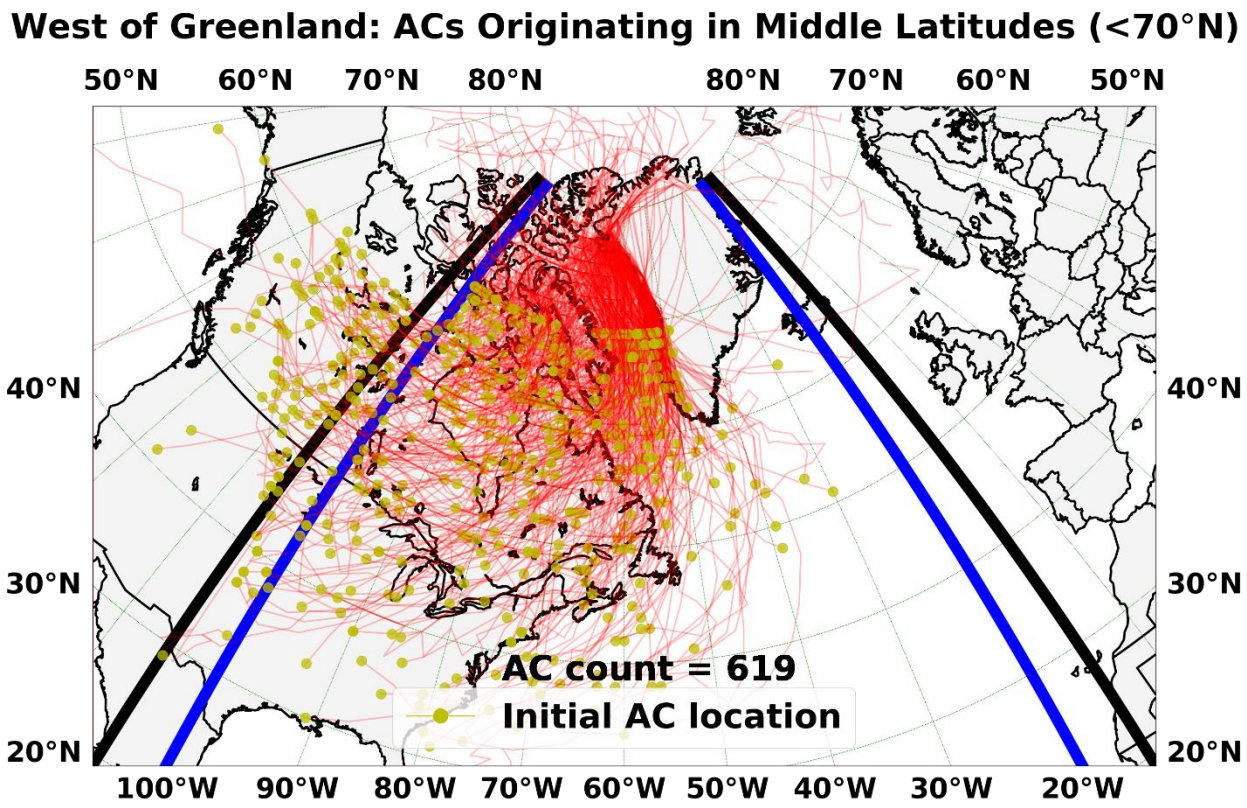

Fig. 10. As in Fig. 7 except for West of Greenland sector.

3 Climatologies

3.1 Sectorial sinuosity climatology

To quantify disruptions of the tropospheric polar vortex according to sector, a sectorial sinuosity climatology is constructed for 1979–2018 using ERA-Interim reanalyses for the equatorward boundary of the tropospheric polar vortex defined by a threshold geopotential height contour on the 300-hPa surface. The method for calculating sectorial sinuosity is described as follows and refers to Fig. 11:

I. Calculate the area of the sector enclosed by a representative 300-hPa geopotential height threshold contour as determined by Frauenfeld et al. (2003).

II. Determine the equivalent latitude, the latitude poleward of which the area is equal to the area enclosed by the threshold geopotential height contour.

III. Calculate the ratio of the length of the 300-hPa geopotential height threshold contour to the length of the equivalent latitude sector.

3.2 Characteristic 300-hPa synoptic patterns

A total of 2351 days of positive Greenland ice-melt anomaly is identified during April–October 1979–2018 from data taken from the National Snow and Ice Data Center (https://nsidc.org/greenland-today/greenland-surface-melt-extent-interactive-chart/). The upper 40th percentile of the 2351 identified days corresponds to 942 days with melting equal to or above +1 standard deviation of Greenland ice melt. Probability density functions (PDFs) of sectorial sinuosity associated with ±1 sigma Greenland ice-melt days show that it is more likely for +1 sigma ice-melt days to occur in high sectorial sinuosity regimes compared to −1 sigma ice-melt days (Fig. 12).

A climatology is constructed of Greenland ice-melt events that have 3 consecutive days or more of ice melt greater than or equal to +1 standard deviation. Events of 3 consecutive days or more constitute the upper 75th percentile of total +1 sigma ice-melt days from the 1979–2018 climatology. 129 ice-melt events are identified and are grouped by year (Fig. 13) and month (Fig. 14), hereafter referred to as events. Figure 13 shows that there is a substantial increase in events during 1979–2018. For the first decade, 1979–1988, only 3 events occurred, all in 1988. For the second decade, 1989–1998, there is an increase in the number of events to 18 with a frequency of occurrence of events per year ranging between 1 and 6. Events occurred in 8 out of the 10 years, except for 1993 and 1994. For the third decade, 1999–2008, there is another increase in the number of events to 51, with a frequency of occurrence of events per year ranging between 2 and 10. Events occurred every year during this decade. For the fourth decade, 2009–2018, the number of

events total 57 with a frequency of occurrence of events per year ranging between 1 and 11. Events occurred every year during this decade. Figure 14 shows the number of ice-melt events by month: 70 events occurred in June, July, and August, 32 events occurred in March, April, and May, and 27 events occurred in September and October. The 129 events in Fig. 14 equate to 690 days and are classified into three groups according to the magnitude of the sectorial sinuosity of the threshold 300-hPa geopotential height contour: 155 days with sectorial sinuosity between 1 and 2 (group 1), 354 days with sectorial sinuosity between 2 and 3 (group 2), and 181 days with sectorial sinuosity greater than 3 (group 3).

Based on the above classification, characteristic 300-hPa geopotential height patterns associated with anomalous Greenland ice-melt events are identified using SOMs constructed from ERA-Interim reanalysis data (https://www.ecmwf.int/en/forecasts/datasets/reanalysis-datasets/era-interim). Each sectorial sinuosity group is divided into three categories or nodes, totaling to 9 nodes (Fig. 15), where a node consists of similar 300-hPa geopotential height patterns identified by the SOMs. For every node of characteristic 300-hPa geopotential height pattern the following variables are plotted: Standardized 300-hPa geopotential height anomaly (Fig. 16), 300-hPa wind speed (Fig. 17), standardized precipitable water anomaly (Fig. 18), 700-hPa temperature (Fig. 19) and standardized 700-hPa temperature anomaly (Fig. 20), and distribution of frequency of ice-melt days per month for each node (Fig. 21).

3.2.1 Discussion of 9-panel plots

For days from group 1:

For 300-hPa geopotential height, standardized geopotential height anomaly, and wind speed (Figs. 15, 16, and 17): Node 1 shows a deep negatively tilted trough associated with a −1 sigma geopotential height anomaly extending to the southeast of Greenland. The −1 sigma geopotential height anomaly coincides with a strong westerly jet with a maximum of 42 m s^{-1} and southeasterly flow associated with a ridge east of Greenland. Node 2 shows a positively tilted trough–ridge pattern associated with a +1.5 sigma geopotential height anomaly and a strong westerly jet with a maximum of 40 m s^{-1} over southwestern Greenland associated with a ridge over southern Greenland. Node 3 shows a low-amplitude trough–ridge pattern associated with a +0.75 sigma geopotential height anomaly and a relatively weak westerly jet with a maximum of 30 m s^{-1} associated with a ridge over southeastern Greenland.

Standardized precipitable water anomaly plots (Fig. 18) show that the largest positive anomaly is associated with node 2 with a +2 sigma maximum over southern Greenland, followed by node 3 with a +1.25 sigma maximum over southern and southwestern Greenland, and node 1 with a +1 sigma maximum over southeastern Greenland. The standardized precipitable water anomaly maxima are located upstream of the ridge axes.

Figure 19 shows that a 700-hPa thermal ridge associated with nodes 1–3 is collocated with positive standardized 700-hPa temperature anomalies (Fig. 20) and the 300-hPa geopotential height ridge (Fig. 15). Standardized 700-hPa temperature anomaly plots (Fig. 20) show the largest positive anomaly is associated with node 2 with a +1.5 sigma maximum over the southeastern coast of Greenland, followed by node 3 with a +1 sigma maximum centered over central and southeastern Greenland and by node 1 with a +0.75 sigma maximum over east Greenland.

Node 1 and 2 are associated with days that mostly occur in the colder months of the Greenland ice-melt season, April, May, September, and October. Node 3 is associated with days that mostly occur in the warmer months of the Greenland ice-melt season, June, July, August, and also extending into September and October (Fig. 21).

For days from group 2:

All nodes within group 2 exhibit a relatively similar trough–ridge pattern with the trough over northeastern Canada and the ridge over southern and southeastern Greenland. The trough–ridge pattern in node 1 is associated with a weak westerly jet with a maximum of 26 m s^{-1} across the northeastern United States extending eastward into the Atlantic. The trough–ridge pattern in nodes 2 and 3 is associated with a strong westerly jet with maxima of 30 m s^{-1} in node 2 and 34 m s^{-1} in node 3 across the northeastern United States extending into the Atlantic. A secondary maximum in wind speed is located over southwestern Greenland with maxima of 26 m s^{-1} in node 2 and 32 m s^{-1} in node 3 (Figs. 15 and 17). The variation in jet intensity between the three nodes may be attributed to the month of occurrence of the geopotential height patterns for each node, where nodes with patterns associated with stronger jets in nodes 2 and 3 are associated with the colder months of the ice-melt season and the pattern associated with the weaker jet in node 1 is associated with the warmer months of the ice-melt season (Fig. 21).

Standardized precipitable water anomaly plots (Fig. 18) show that the largest positive anomaly is associated with node 3 with a +1.5 sigma maximum over southern Greenland, followed by node 2 with a +1.25 sigma maximum also over southern Greenland, and node 1 with the smallest positive

anomaly and a ~+1.25 sigma maximum over central Greenland. The standardized precipitable water anomaly maxima are located upstream of the ridge axes.

Standardized 700-hPa temperature anomaly plots show that the maximum anomaly situated over southeastern Greenland is +1.25 sigma for nodes 1 and 3 and +1 sigma for node 2. These positive temperature anomalies (Fig. 20) are collocated with the 700-hPa thermal ridge (Fig. 19) and the 300-hPa geopotential height ridge (Fig. 15).

For days from group 3:

Nodes from this group exhibit the largest sectorial sinuosity and the highest-amplitude ridges with the largest spatial extent. For 300-hPa geopotential height, standardized geopotential height anomaly, and wind speed (Figs. 15, 16, and 17): Node 1 shows an omega block ridge pattern over central and southern Greenland that is associated with a +1.75 sigma geopotential height anomaly and a westerly jet with a maximum of 30 m s^{-1}. Node 2 shows a Rex block ridge pattern with a cutoff anticyclone over central and southern Greenland that is associated with a +1.75 sigma geopotential height anomaly north of a cutoff cyclone south of Greenland that is associated with a −1.25 sigma geopotential height anomaly. Node 2 exhibits a westerly jet across the northeastern United States extending eastward into the Atlantic with a maximum of 36 m s^{-1} in the base of the cutoff cyclone south of Greenland and a secondary jet aligned with the ridge over Greenland with a maximum of 24 m s^{-1}. Node 3 shows an omega block ridge pattern over central and southern Greenland that is associated with a +1.5 sigma geopotential height anomaly. Node 3 exhibits a westerly jet across the northeastern United States extending eastward into the Atlantic with a maximum of 36 m s^{-1} in the base of the trough over the northeastern United States and a secondary jet aligned with the ridge over Greenland with a maximum of 28 m s^{-1}.

Standardized precipitable water anomaly plots (Fig. 18) show comparable positive anomalies for all 3 nodes with a +1.25 sigma maximum. The +1 sigma contour covers most of Greenland in nodes 1 and 2, where the spatial extent of the positive anomaly encompasses the largest area relative to all 9 nodes. Although nodes 1 and 3 are associated with comparable 300-hPa geopotential height patterns, the standardized precipitable water anomaly maximum for node 3 is concentrated over southwestern Greenland and the Labrador Sea, with an extension into the northwestern tip of Greenland surrounding a local minimum over central Greenland.

Standardized 700-hPa temperature anomaly plots show that the largest maximum anomaly of +1.75 sigma is associated with node 2. Nodes 1 and 3 follow with maximum anomalies of +1.5 and +1.25 sigma, respectively. The positive temperature anomaly is located over southern and southeastern Greenland for all of the nodes. For all nodes in group 3 the positive temperature anomaly (Fig. 20) is also collocated with the 700-hPa thermal ridge (Fig. 19) and the 300-hPa geopotential height ridge (Fig. 15), and covers a larger area over Greenland than the nodes from the lower-amplitude groups. This larger area may be attributed to the larger areal extent of the 300-hPa geopotential height ridge compared to nodes from the lower-amplitude groups and is associated with the high-amplitude geopotential height patterns in group 3.

A PDF is calculated for each node that shows the probability density of ice-melt days as a function of standardized Greenland ice-melt anomaly (Fig. 22). The PDFs show that some nodes are associated with a PDF that is skewed towards lower values of standardized ice-melt anomaly and other nodes are associated with a PDF that exhibits a gradual spread from lower to higher values of standardized ice-melt anomaly. The standardized ice-melt anomaly ranges from +1 sigma,

consistent with the construction of the Greenland ice-melt climatology, and reaches maximum values between +5 and +6 sigma for some nodes.

For days from group 1 (Fig. 22):

The PDF for node 1 is skewed towards low standardized ice-melt anomaly, with a maximum of 0.60 at ~+1.8 sigma and decreasing to 0.10 at ~+3.0 sigma. The PDF for node 2 gradually decreases from a maximum of 0.27 at ~+1.5 sigma to 0.04 at ~+5.8 sigma. The PDF for node 3 is skewed towards low standardized ice-melt anomaly, with a maximum of 0.55 at ~+1.4 sigma and decreasing to 0.05 at ~+5.6 sigma.

For days from group 2 (Fig. 22):

The PDF for node 1 is skewed towards low standardized ice-melt anomaly, with a maximum of 0.58 at +1.4 and decreasing to 0.01 at +5.1 sigma. The PDF for node 2 is also skewed towards low standardized ice-melt anomaly, with a maximum of 0.42 at +1.7 sigma and decreasing to 0.04 at +5.8 sigma. The PDF for node 3 gradually decreases from a maximum of 0.30 at +1.9 sigma to 0.08 at +5.8 sigma.

For days from group 3 (Fig. 22):

The PDF for node 1 exhibits a spread for low values of standardized ice-melt anomaly, with a maximum of 0.45 at +1.6 sigma and gradually decreasing to 0.35 at +2.8 sigma and dropping to 0.04 at +3 sigma. The PDF for node 2 exhibits a spread for low values of standardized ice-melt anomaly, with a maximum of 0.41 at +1.5 sigma and decreasing to 0.06 at +4.6 sigma. The PDF for node 3 exhibits a spread over all values of standardized ice-melt anomaly, ranging from +1

sigma to +4.9 sigma, with a maximum of 0.35 at +1.9 sigma gradually decreasing to 0.40 at +4.9 sigma.

3.2.2 Thermal metric and precipitable water metric

To describe 700-hPa temperature and precipitable water patterns associated with each node, a thermal metric and a precipitable water metric are calculated by taking area-averaged values of the standardized 700-hPa temperature anomaly and the standardized precipitable water anomaly, respectively, for a domain over Greenland for the 942 days with melting greater than or equal to +1 standard deviation of Greenland ice melt (Fig. 23). Domain boundaries start at latitude of 60°N and longitude of 60°W and end at latitude of 80°N and longitude of 15°W. The thermal metric is used to link 300-hPa geopotential height patterns to 700-hPa temperature patterns. The precipitable water metric is used to link 300-hPa geopotential height patterns to vertically integrated water vapor patterns. The best-fitting regression line relating each metric to Greenland ice melt was calculated using linear regression for each node to diagnose the relationship between the two metrics and Greenland ice melt. The days for each node are sorted by increasing order of standardized Greenland ice-melt anomaly for each day, and the regression line and the associated values for the thermal and precipitable water metrics are plotted in Fig. 24a and Fig. 24b, respectively.

For the thermal metric, nodes 3, 4, and 7 have the highest R-values of 0.53, 0.56, and 0.66, followed by nodes 5, 6, and 8 with R-values of 0.36, 0.39, and 0.50, and nodes 1, 2, and 9 with R-values of 0.17, 0.13, and 0.20. Figure 21 shows that nodes with the highest R-values (nodes 3, 4, and 7) are associated with the warmer months of the ice-melt season with the exception of a smaller portion of total days within node occurring in September, and nodes with the lowest R-values

(nodes 1, 2, and 9) are associated with the colder months of the ice-melt season with node 2 having 2 days occurring in June and node 9 having 6 days occurring in June. Nodes with R-values that fall in between the highest and lowest R-values (nodes 5, 6, and 8) are associated with days occurring in both the warmer and colder months of the ice-melt season for nodes 5 and 8, and from the colder months of the ice-melt season for node 6. For the precipitable water metric, nodes 3, 4, 5, 7, and 8 have the highest R-values of 0.46, 0.49 0.46, 0.55, and 0.47, followed by nodes 6 and 9 with R-values of 0.29 and 0.24, and nodes 1 and 2 with R-values of −0.01 and 0.18. Figure 21 shows that nodes with the highest R-values, nodes 3, 4, and 7 are associated with the warmer months of the ice-melt season and nodes 5 and 8 are associated with days that occur in both the warmer and colder months of the ice-melt season. Nodes with the lowest R-values (nodes 1, and 2) are associated with the colder months of the ice-melt season with node 2 having 2 days occurring in June. Nodes with R-values that fall in between the highest and lowest values are node 6 and node 9. Node 9 is associated with the colder months of the ice-melt season with 6 days occurring in June and node 6 is associated with the colder months of the ice-melt season. The regression analysis shows that nodes associated with days that occur in the colder months of the ice-melt season exhibit a weak dependence (i.e., low R-values) of each of the metrics on ice melt, whereas nodes associated with days that occur in the warmer months of the ice-melt season exhibit a strong dependence (i.e., high R-values) of each of the metrics on ice melt.

3.2.3 Temporal evolution of events

To describe the evolution of each of the 129 events (Figs. 13 and 14), every day of each event is matched with the corresponding node out of the 9 total nodes. 3-day patterns are identified

from overlapping 3-day periods within each event. All 9 nodes from the three groups are described below based on the 300-hPa geopotential height patterns shown in Fig. 15:

I. Node 1 is associated with a low-amplitude negatively tilted trough–ridge pattern.

II. Node 2 is associated with a low-amplitude positively tilted trough–ridge pattern.

III. Node 3 is associated with a low-amplitude neutrally tilted trough–ridge pattern.

IV. Nodes 4–6 are associated with medium-amplitude trough–ridge patterns.

V. Nodes 7 and 9 are associated with a high-amplitude omega block ridge pattern.

VI. Node 8 is associated with a high-amplitude Rex block ridge pattern.

For example, in a 5-day ice-melt event, the 300-hPa geopotential height pattern for each day is associated with its corresponding node identified by the SOMs and days 1–5 exhibit a geopotential height pattern indicated by the numerical sequence, 55588. Within this sequence, days 1–3 (555) are associated with node 5, which indicates a medium-amplitude trough–ridge pattern. Days 2–4 (558) and days 3–5 (588) are associated with nodes 5 and 8 which indicate a medium-amplitude trough–ridge pattern and a Rex block ridge pattern, respectively. 73 distinct 3-day patterns are identified. The frequency of occurrence of each distinct 3-day pattern (the number of times a pattern appears within all events) is calculated. The frequency of occurrence of the distinct 3-day patterns ranges from a minimum of 1 to a maximum of 74. For each of the 129 events, we identify the top 20th percentile of the 73 distinct 3-day patterns that are associated with a frequency of occurrence greater than 6 (Fig. 25).

Stable patterns are defined to be distinct 3-day patterns consisting of the same node of the 300-hPa geopotential height pattern, which are 222, 555, 999, 888, 777, 666, 333, and 444. With the

exception of pattern 222 that exhibits a frequency of 8, the remaining stable patterns exhibit frequencies of occurrence of 14, 18, 21, 32, 33, 35, and 74, respectively, which are of higher frequencies relative to all other identified patterns. The stable patterns 333, 444, 555, 666, correspond to trough–ridge patterns, 777 and 999 correspond to omega block ridge patterns, and 888 corresponds to Rex block ridge pattern. Transitions between trough–ridge patterns and omega block ridge patterns, which are the patterns 699, 477, 447, and 774, exhibit frequency of occurrence of 7, 9, 11, and 12, respectively. The patterns 443 and 433 are associated with transitions that correspond to medium amplitude trough–ridge patterns and exhibit frequency of occurrence of 10 and 11, respectively. A remaining transition, 558, between a trough–ridge pattern and a Rex block ridge pattern, exhibits a frequency of occurrence of 8.

3.2.4 Regression analysis for all events

For each of the 129 events a mean value of the thermal metric is calculated for all of the days in each event. Events at the 10th percentile and 90th percentile of the standardized Greenland ice-melt anomaly are identified and 700-hPa temperature values corresponding to the mean value of the thermal metric are plotted in Fig. 26a and Fig. 26b, respectively. The 13 events that fall into the 10th percentile of standardized Greenland ice-melt anomaly occur during the warmer months (i.e., June, July, and August) of the ice-melt season with the exception of only one event occurring in October. These events are associated with low positive mean values of the thermal metric compared to events at the 90th percentile, i.e., the mean value of the area-averaged values of standardized 700-hPa temperature anomaly for all the days in the event. The 13 events that fall into the 90th percentile of standardized Greenland ice-melt anomaly occur during the colder months (i.e., April, May, September, and October) of the ice-melt season with the exception of

only one event occurring in July and one event occurring in August. These events are associated with high positive mean values of the thermal metric.

To diagnose the relationship between Greenland ice melt and the thermal and precipitable water metrics, we conduct a regression analysis for all events. The best-fitting regression line is plotted relating the mean value of the area-averaged metric values calculated for each event and the mean value of the standardized Greenland ice-melt anomaly for each event sorted in increasing order of standardized ice-melt anomaly (Figs. 27a,b).

Both metrics exhibit a moderate dependence on standardized ice-melt anomaly with R-values of 0.41 and 0.38 for the thermal metric and precipitable water metric, respectively. There is large variability between events for both metrics, which is likely a consequence of the fact that the standardized Greenland ice-melt anomaly is only partially explained by the standardized 700-hPa temperature anomaly (i.e., the thermal metric) and the standardized precipitable water anomaly (i.e., the precipitable water metric).

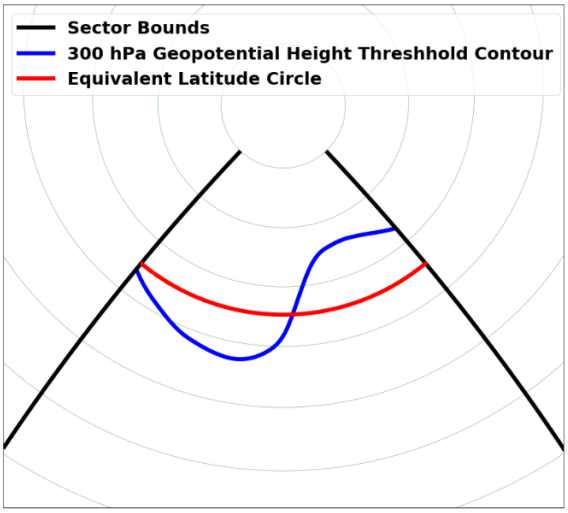

Fig. 11. Illustrative figure for sectorial sinuosity calculation showing sector boundaries (black lines), 300-hPa geopotential height threshold contour (blue curve), and equivalent latitude circle (red curve).

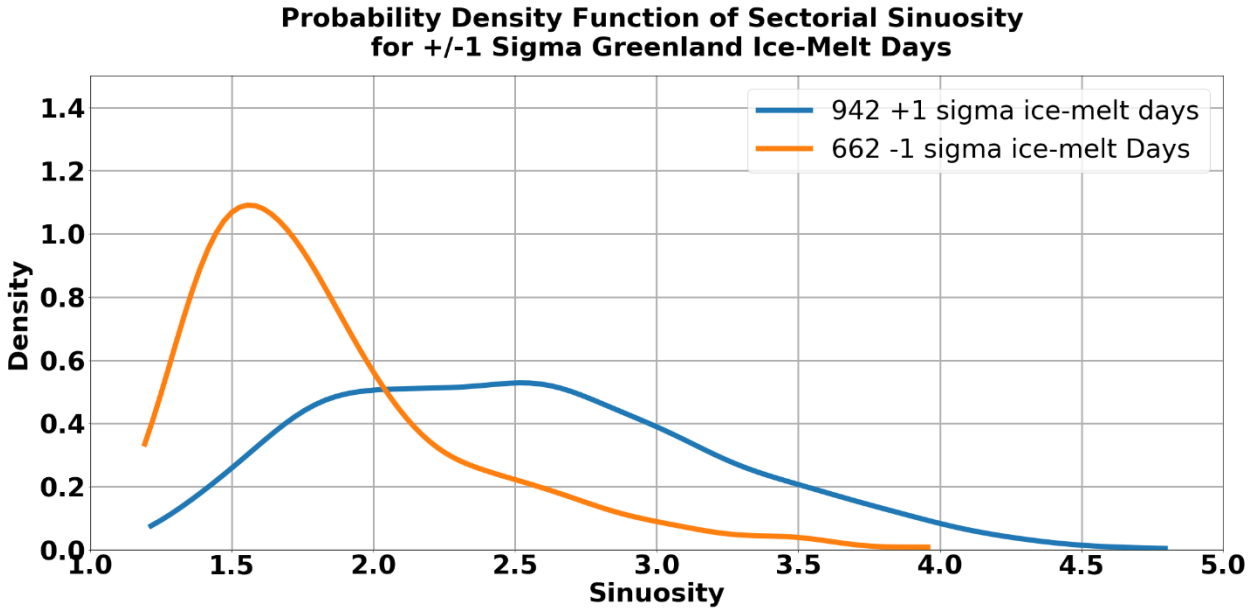

Fig. 12. PDFs of sectorial sinuosity for ±1 sigma Greenland ice-melt days.

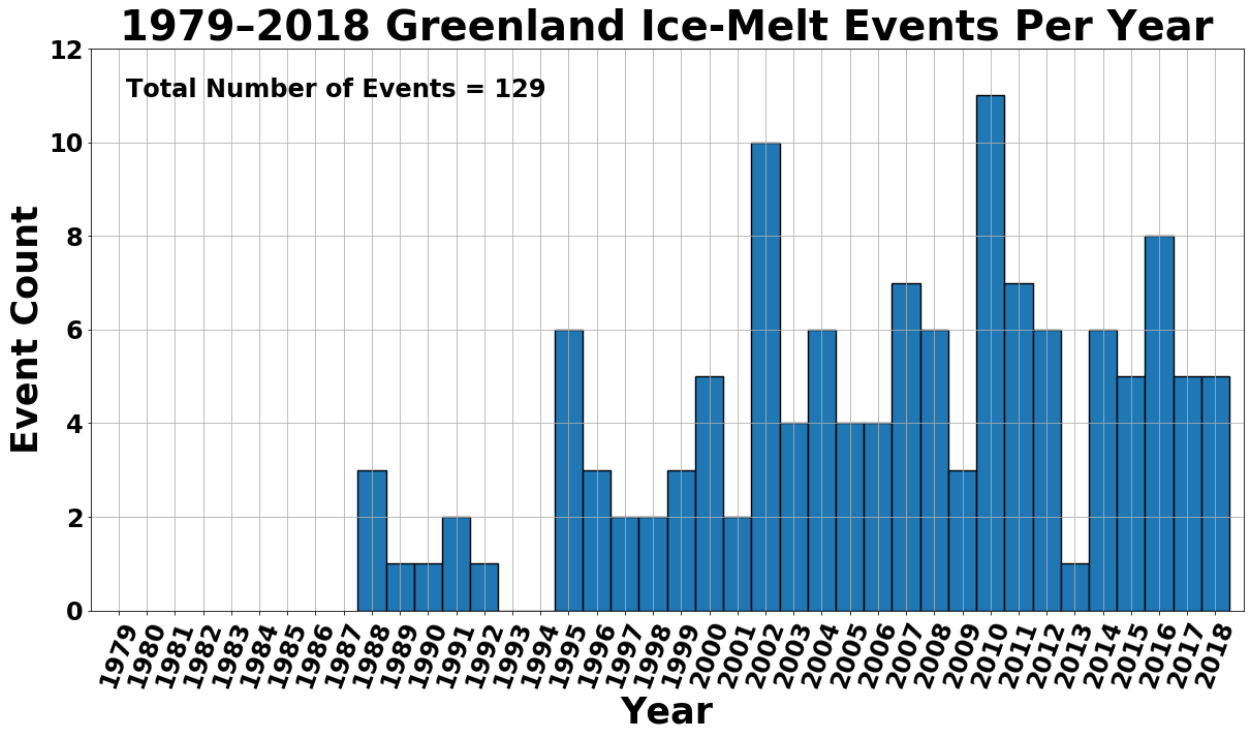

Fig. 13. Greenland ice-melt events per year for 1979–2018.

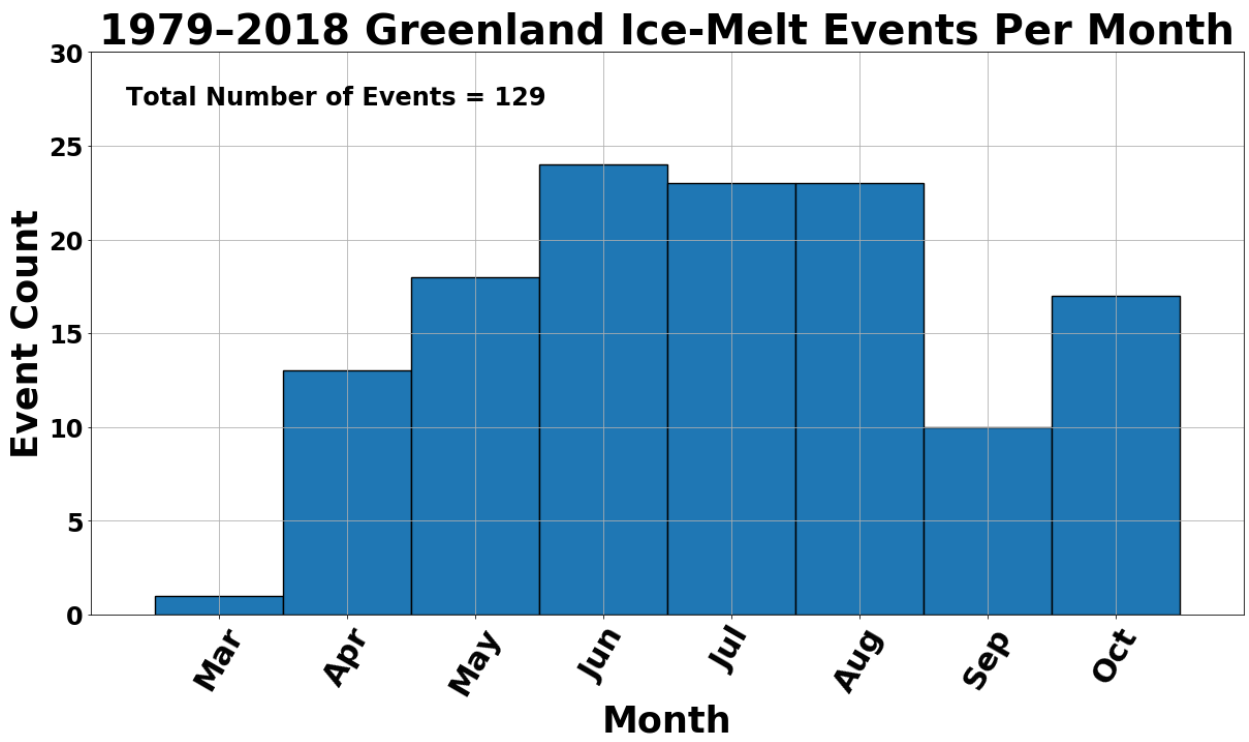

Fig. 14. Greenland ice-melt events per month for 1979–2018.

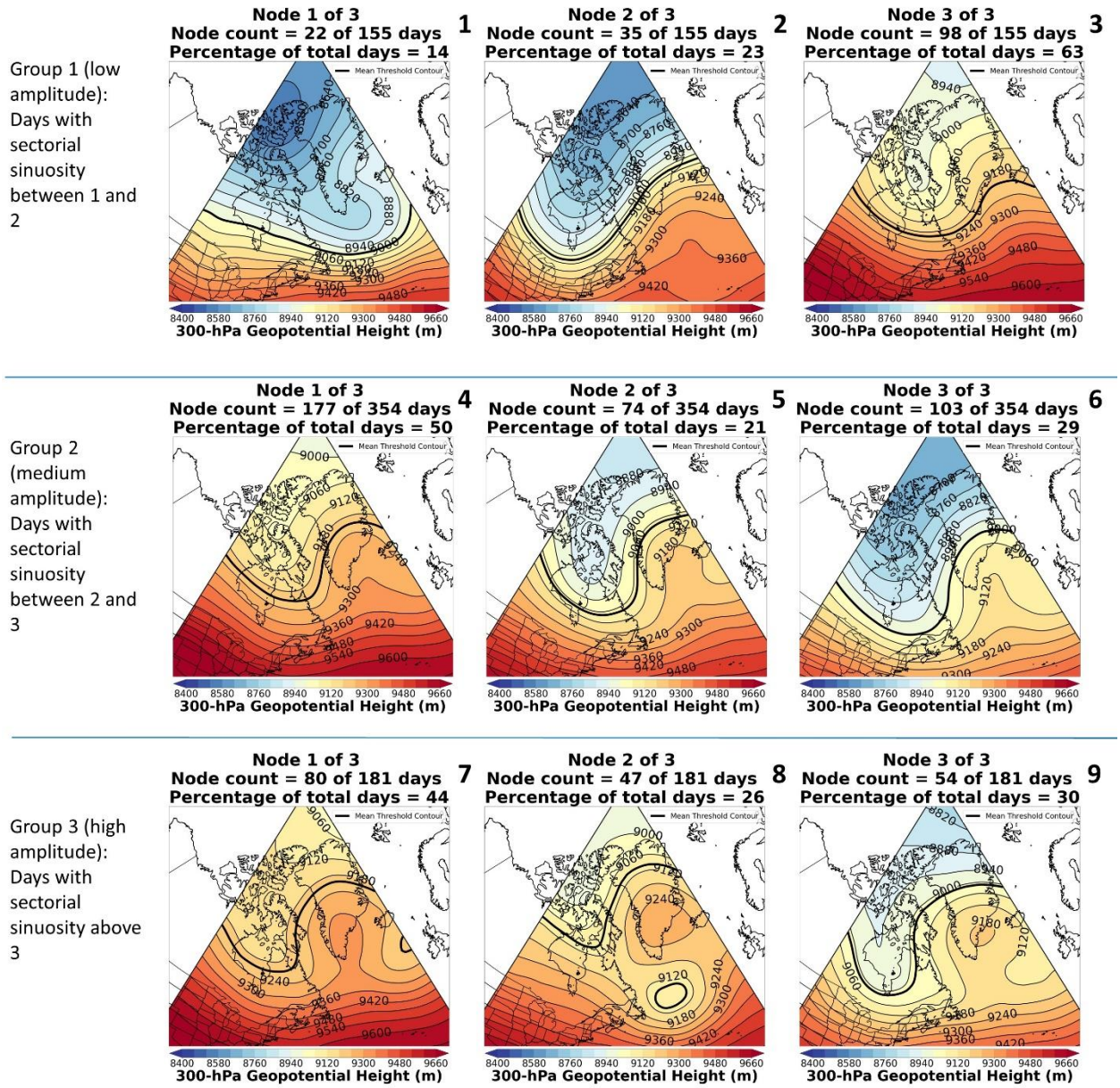

Fig. 15. 9 nodes of characteristic 300-hPa geopotential height patterns identified by the SOMs: nodes 1–3 correspond to sinuosity group 1, nodes 4–6 correspond to sinuosity group 2, and nodes 7–9 correspond to sinuosity group 3.

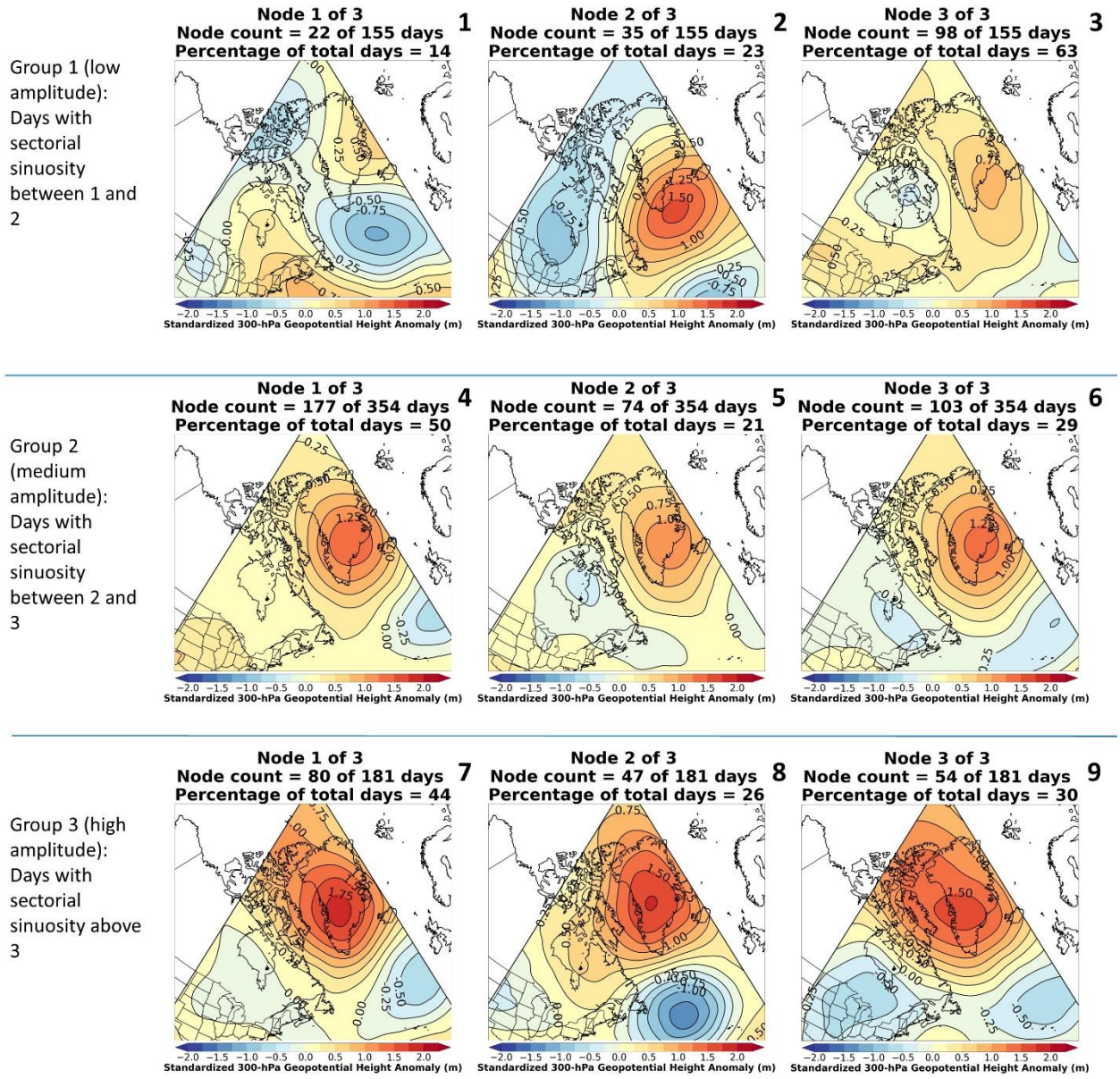

Fig. 16. As in Fig. 15, except for standardized 300-hPa geopotential height anomaly.

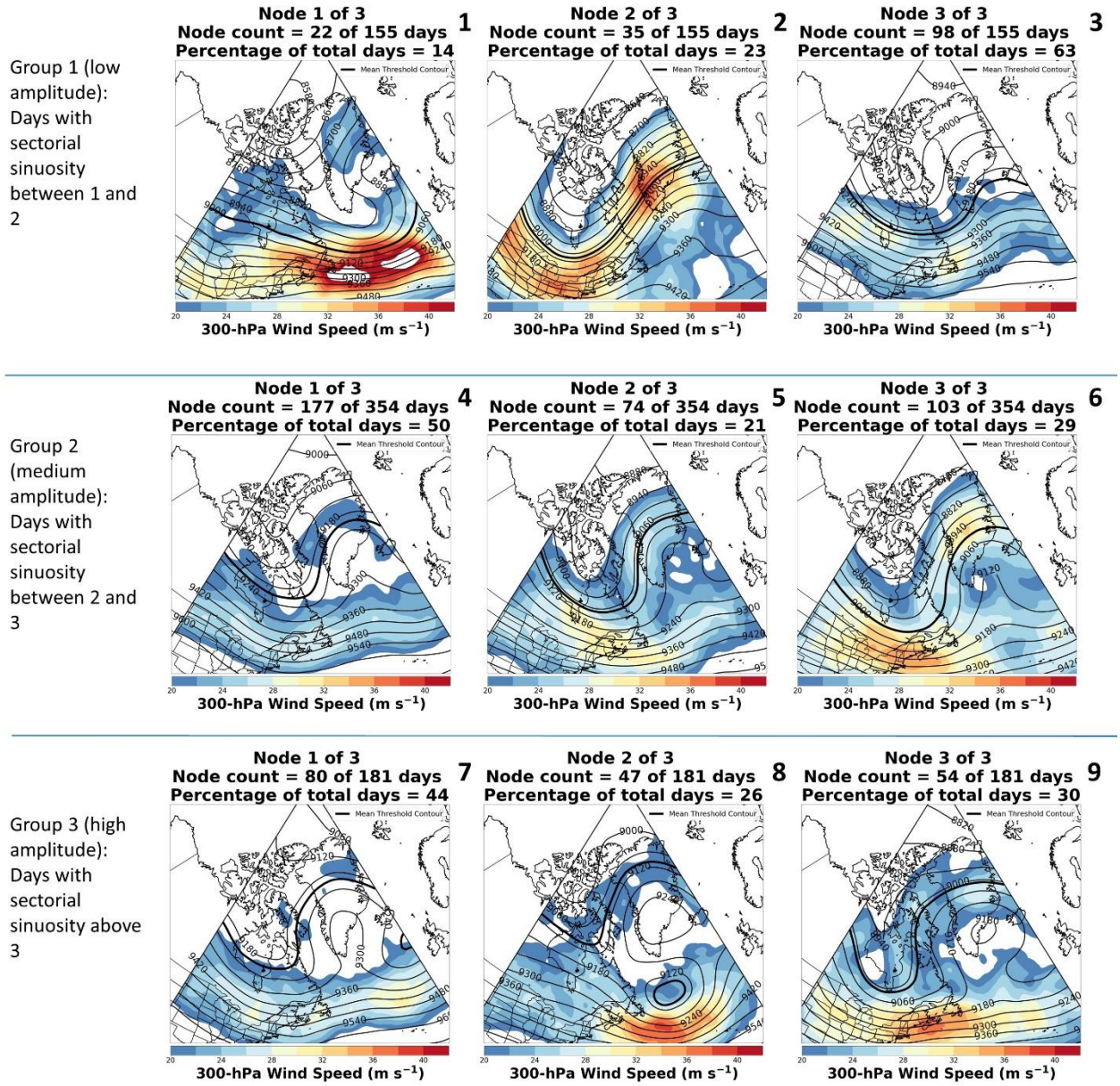

Fig. 17. As in Fig. 15, except for 300-hPa wind speed ($m\ s^{-1}$).

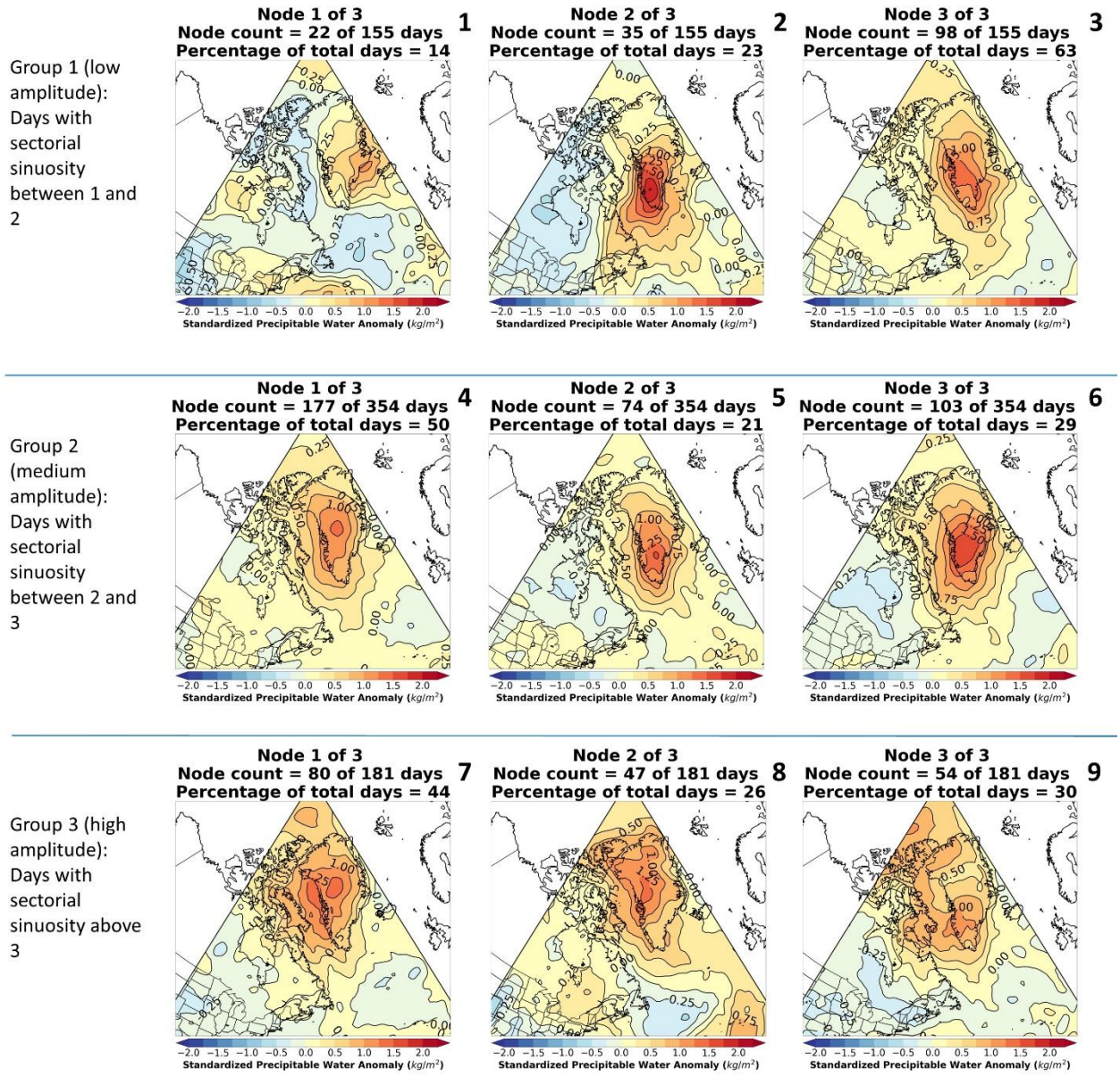

Fig. 18. As in Fig. 15, except for standardized precipitable water anomaly.

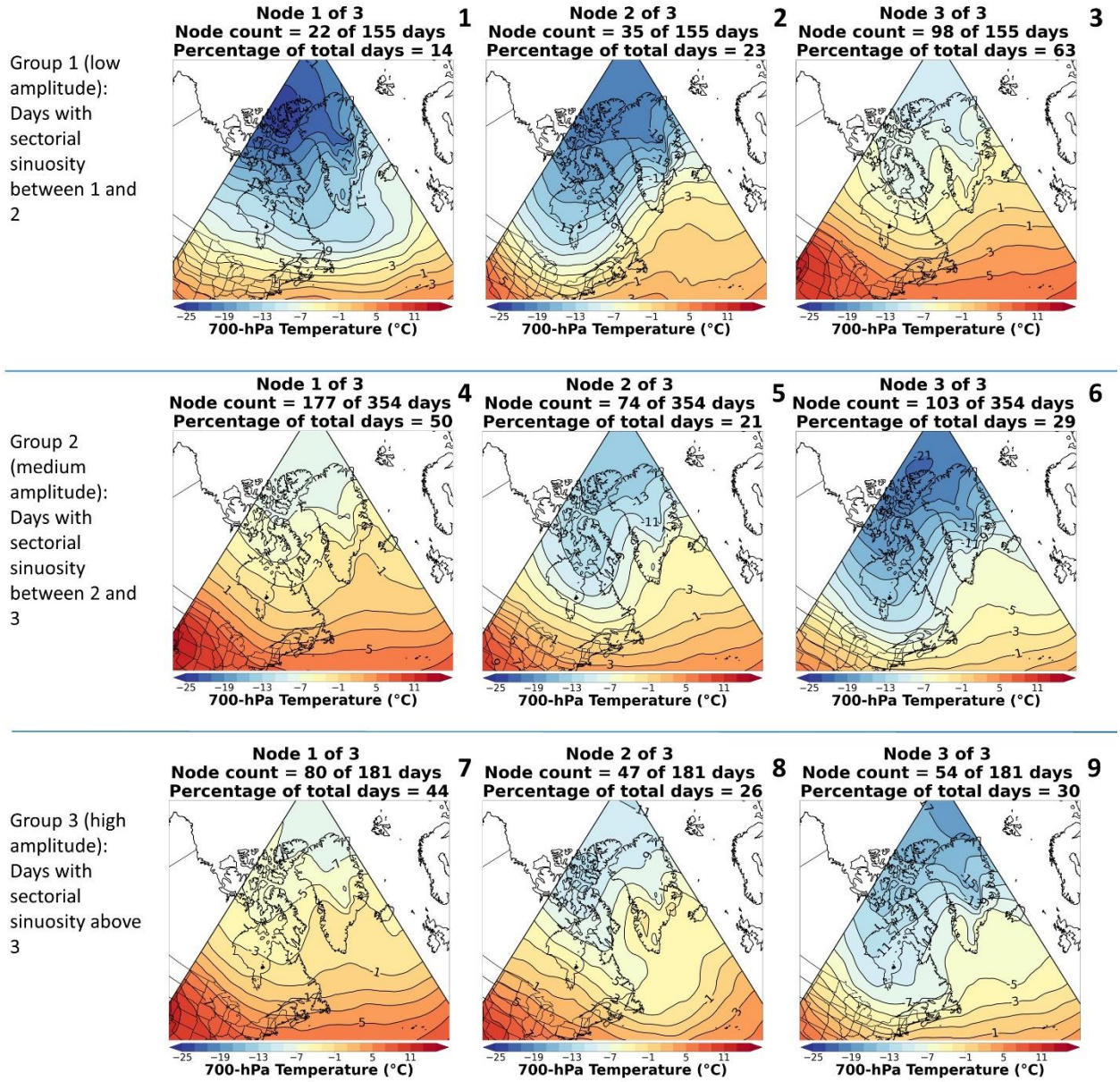

Fig. 19. As in Fig. 15, except for 700-hPa temperature (°C).

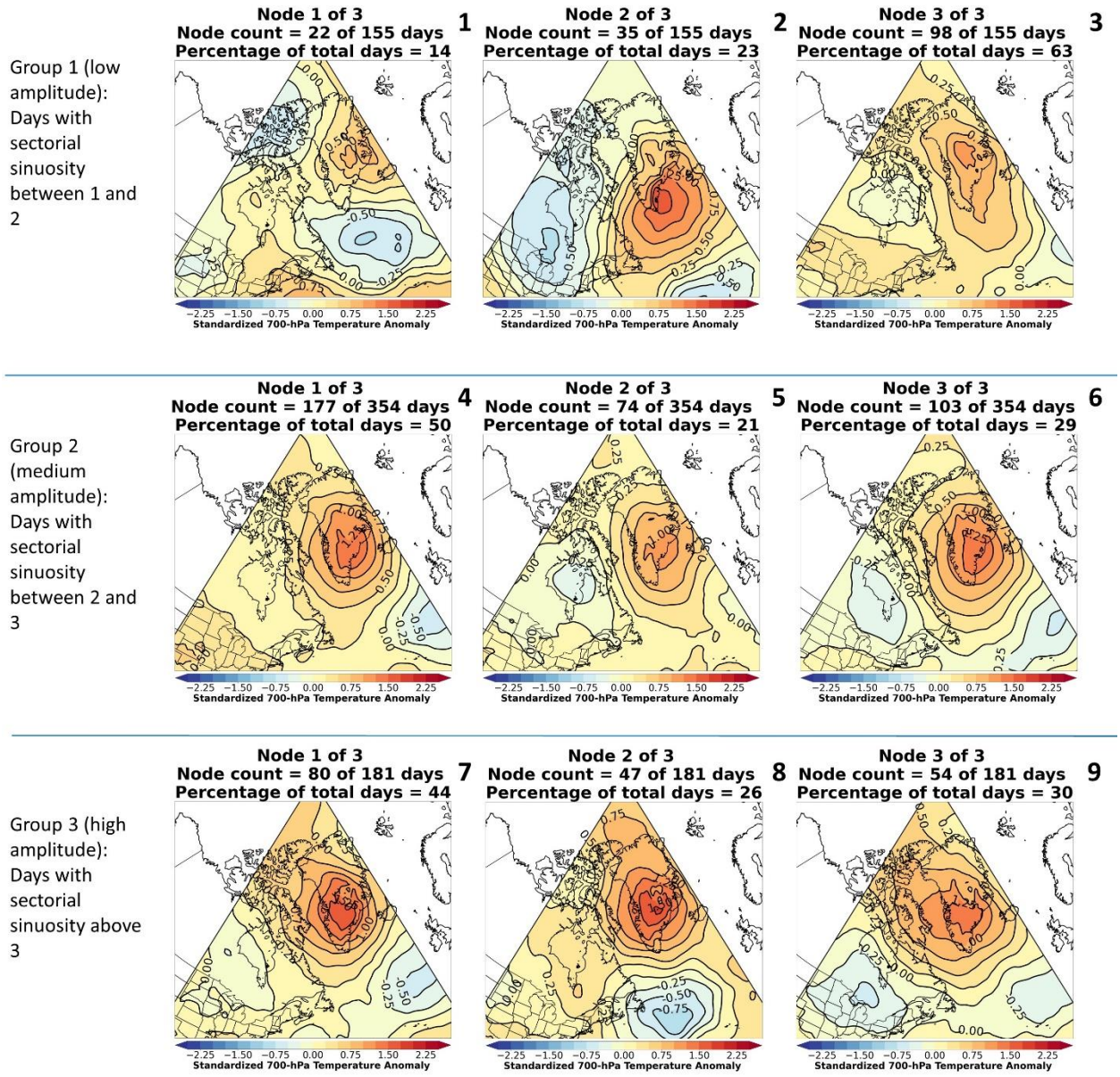

Fig. 20. As in Fig. 15, except for standardized 700-hPa temperature anomaly.

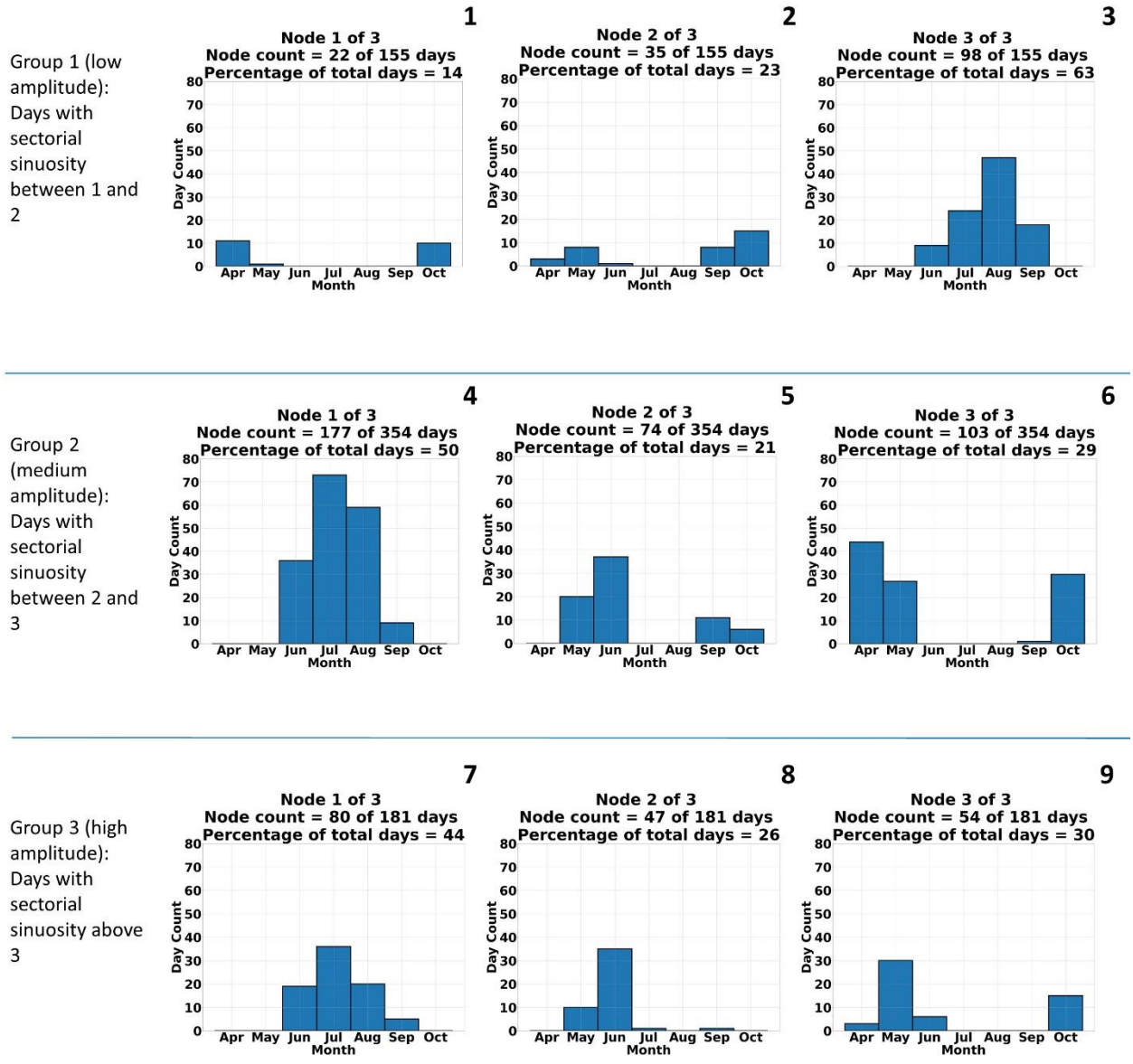

Fig. 21. As in Fig. 15, except for frequency of ice-melt days per month for each node.

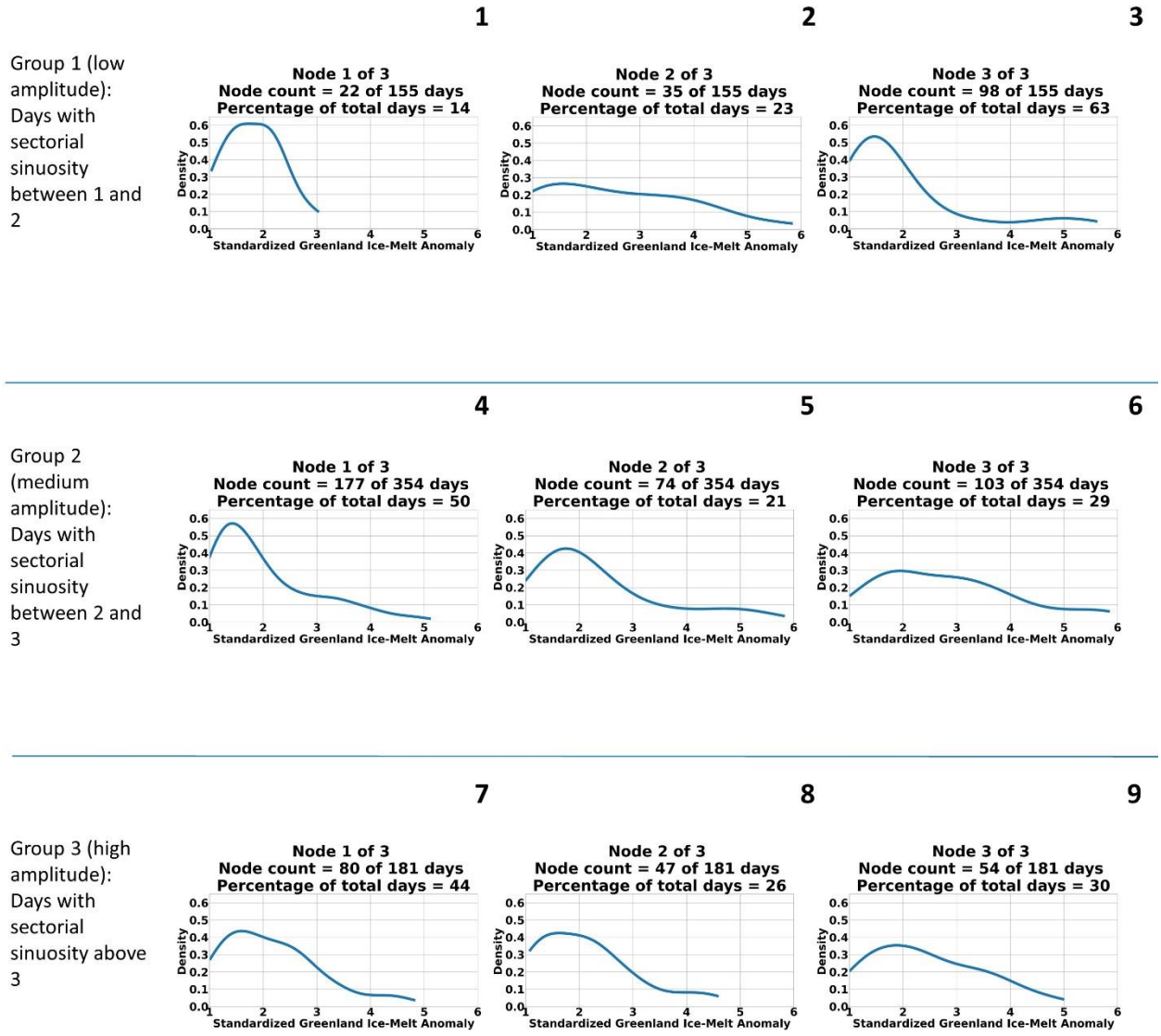

Fig. 22. As in Fig. 15, except for PDFs of standardized Greenland ice-melt anomaly.

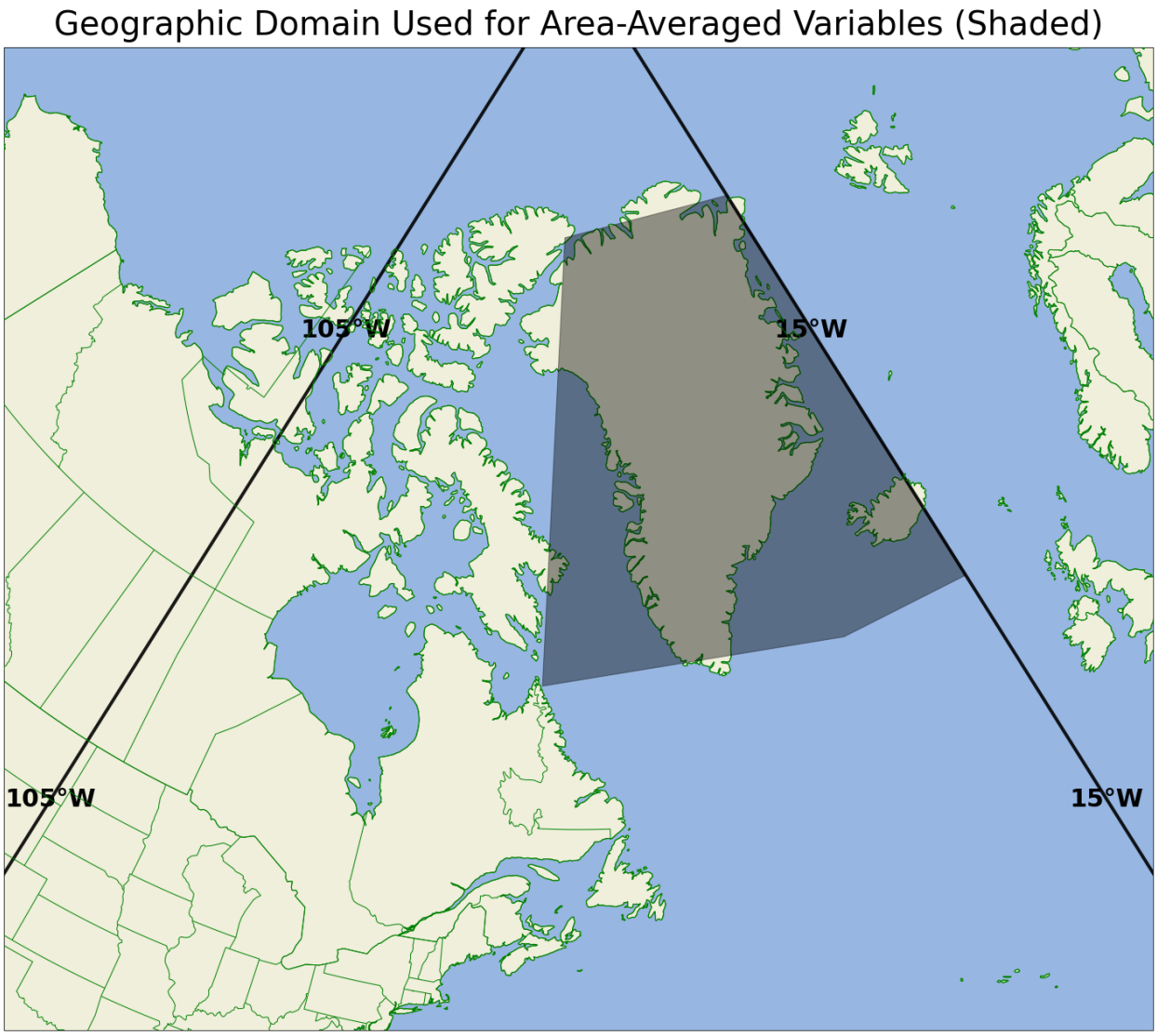

Fig. 23. Geographic domain used for area-averaged variables (shaded). Latitude boundaries of shaded region are approximate to the location of the latitude circles.

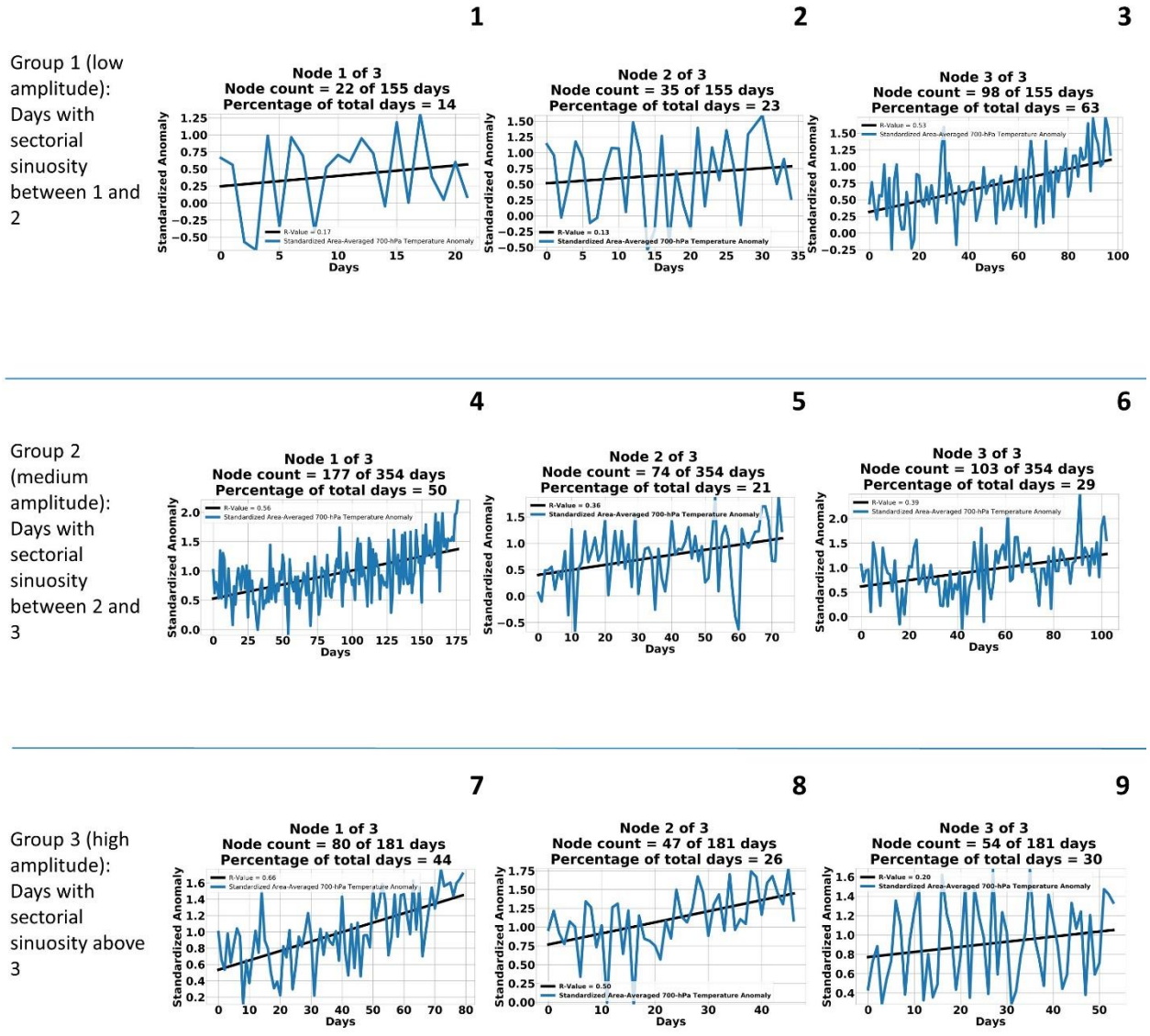

Fig. 24a. As in Fig. 15, except for standardized area-averaged 700-hPa temperature anomaly sorted by increasing order of standardized Greenland ice-melt anomaly for each day.

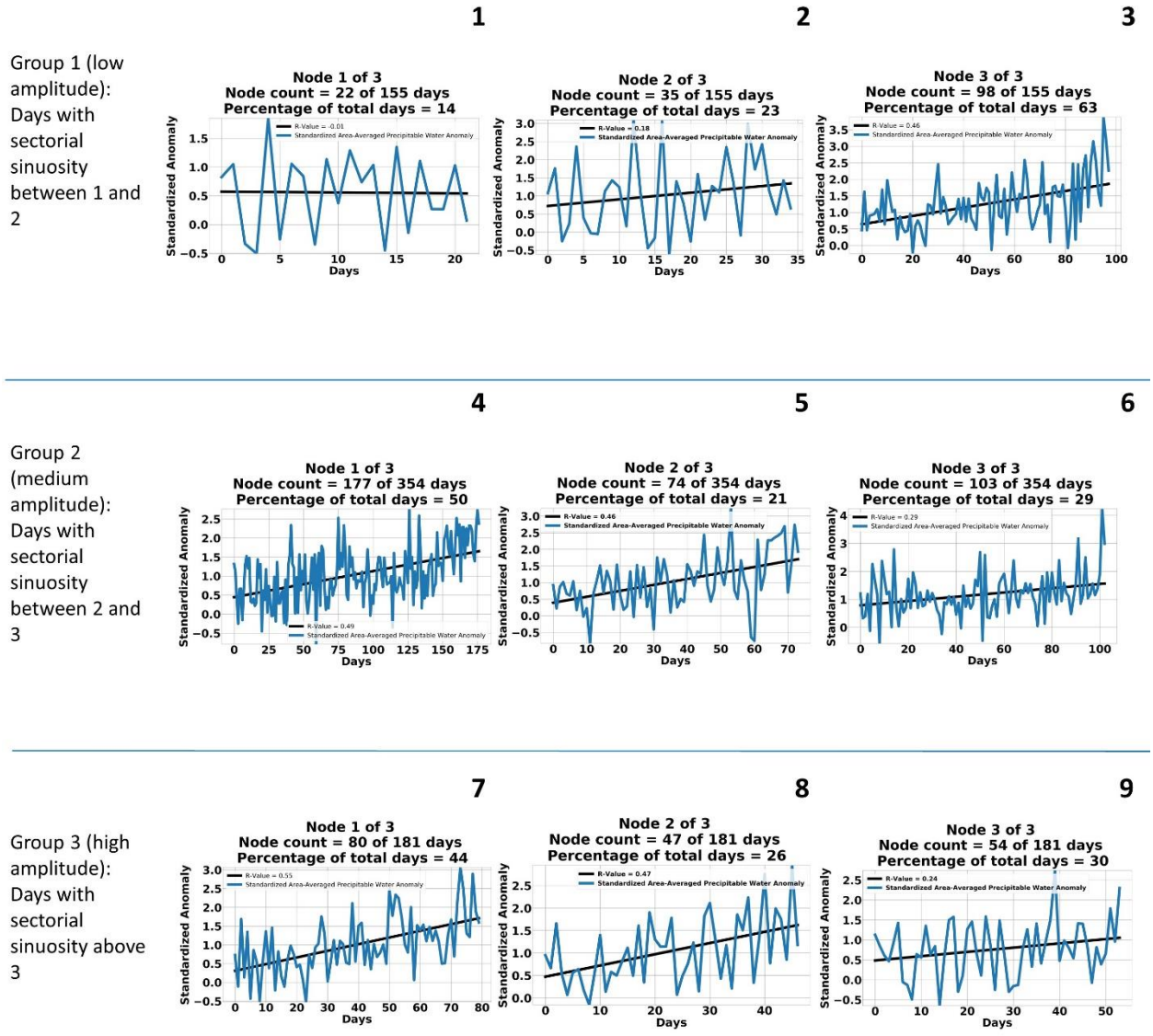

Fig. 24b. As in Fig. 24a, except for standardized area-averaged precipitable water anomaly.

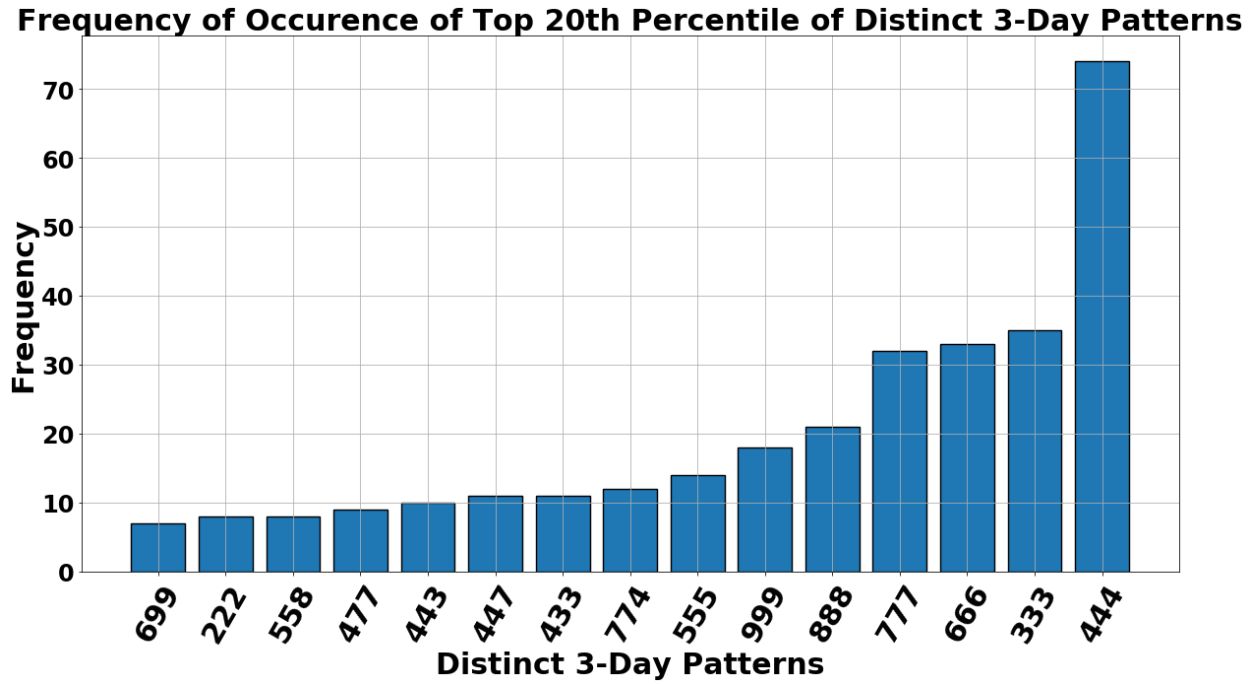

Fig. 25. Frequency of occurrence of top 20th percentile of distinct 3-day patterns.

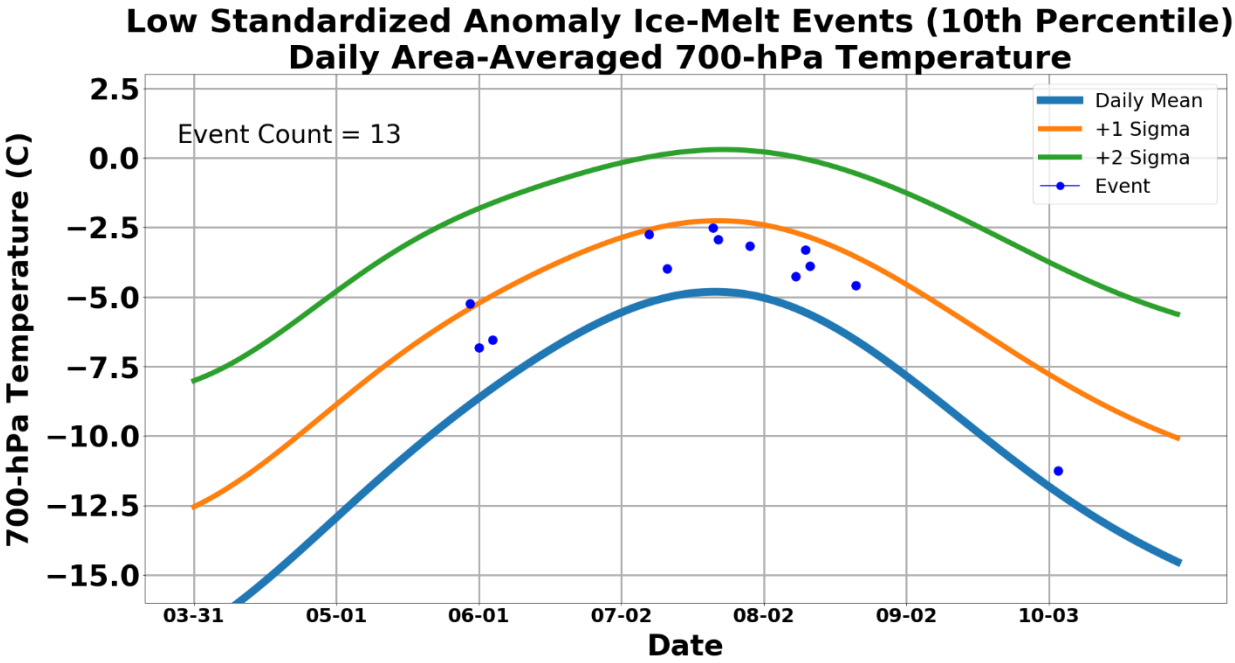

Fig. 26a. Low standardized anomaly of ice-melt events (10th percentile), daily mean of area-averaged 700-hPa temperature (blue curve), +1 sigma of area-averaged 700-hPa temperature (orange curve), and +2 sigma of area-averaged 700-hPa temperature (green curve).

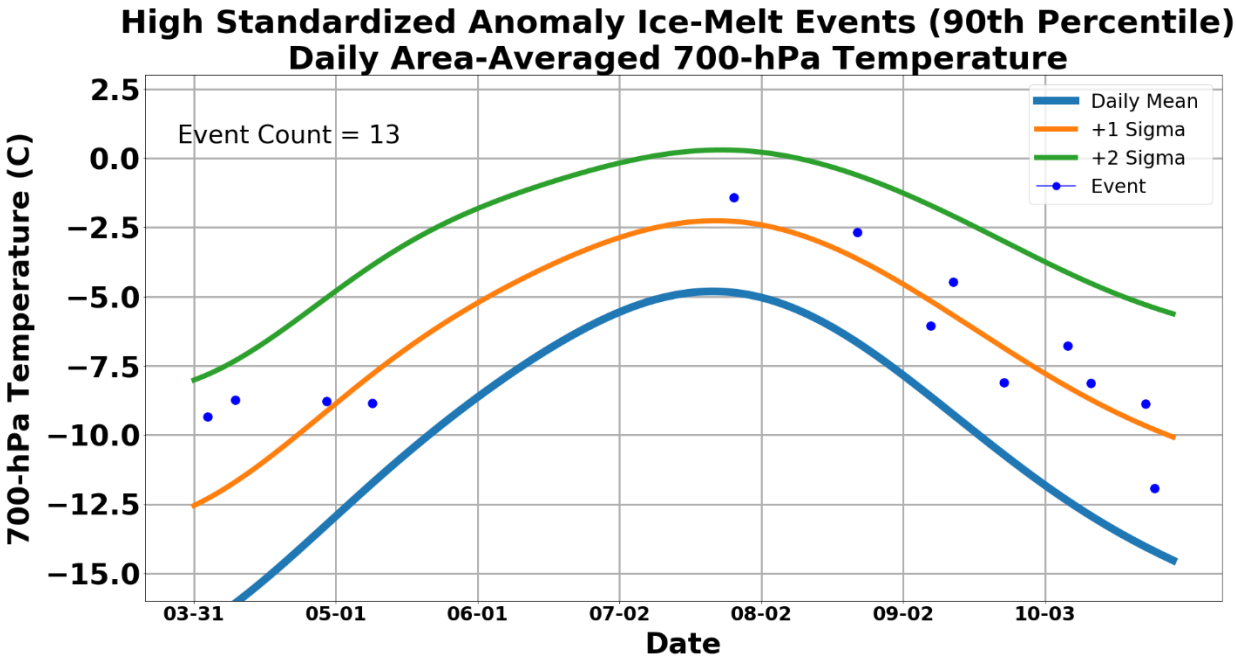

Fig. 26b. As in Fig. 26a, except for high standardized anomaly of ice-melt events (90th percentile).

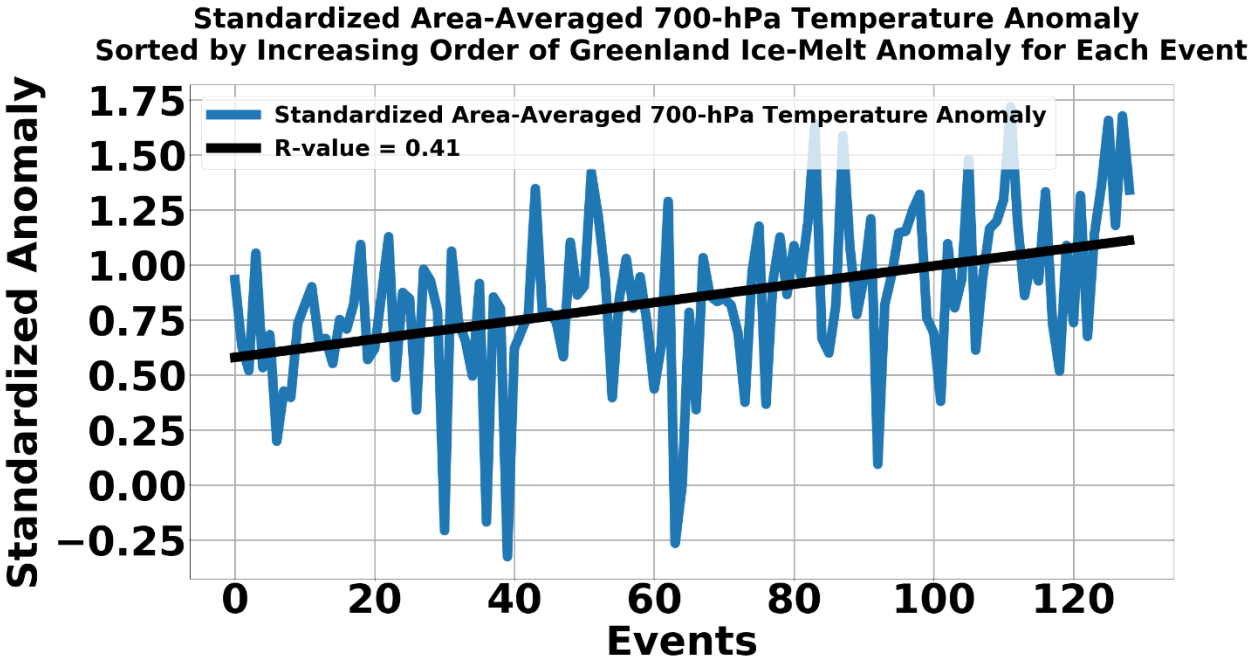

Fig. 27a. Standardized area-averaged 700-hPa temperature anomaly sorted by increasing order of standardized Greenland ice-melt anomaly for each day.

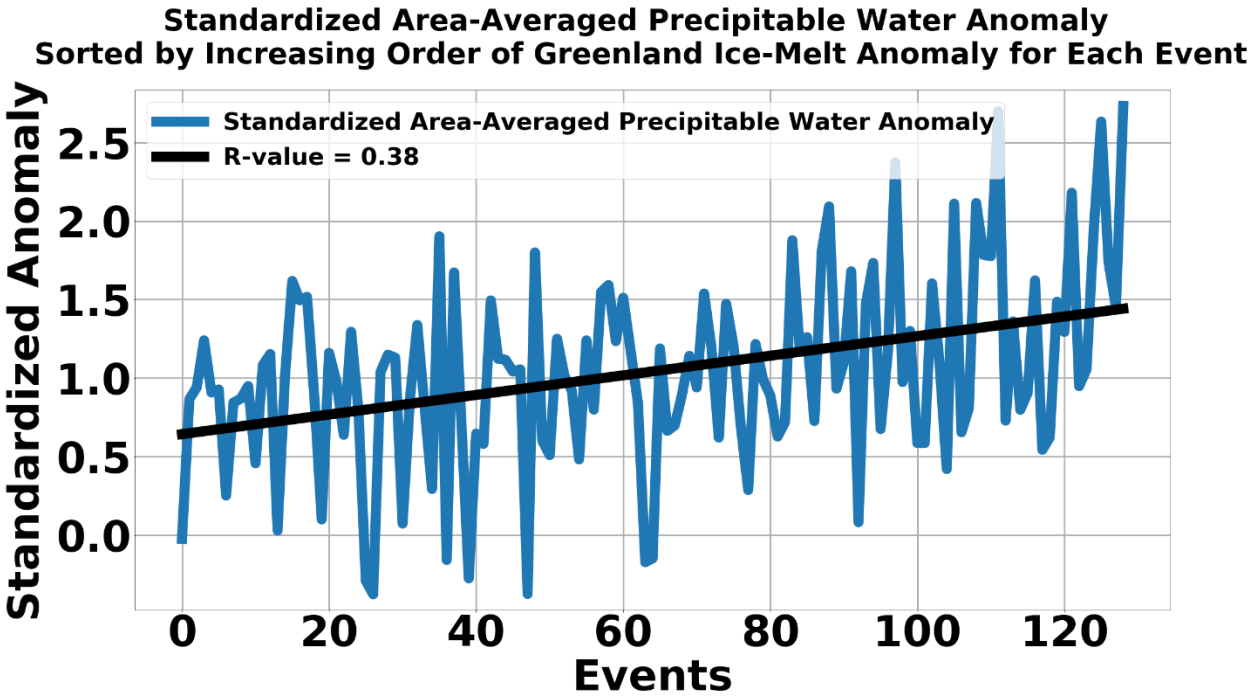

Fig. 27b. As in Fig. 27a, except for standardized area-averaged precipitable water anomaly.

4 Case studies

4.1 QG geopotential height tendency equation

The results of two case studies representative of Greenland ice-melt events at the 10th percentile and 90th percentile of the standardized Greenland ice-melt anomaly are presented and interpreted through calculation of the forcing terms from the 300-hPa QG geopotential height tendency equation. To diagnose the evolution of the tropospheric polar vortex for the two selected events, the forcing terms from the QG geopotential height tendency equation [Eq. (5.6.13) in Bluestein (1992, p. 330)], denoted by Eq. (2), are calculated at 300-hPa. The geopotential tendency is denoted by Eq. (1):

$$\chi = \frac{\partial \Phi}{\partial t} \quad (1)$$

Term A is the advection of geostrophic absolute vorticity by the geostrophic wind, i.e., the propagation term, as annotated in Eq. (2). Term B is the differential advection of temperature by the geostrophic wind, i.e., the amplification term, as annotated in Eq. (2).

$$\left(\nabla_p^2 + \frac{f_0}{\sigma}\frac{\partial^2}{\partial p^2}\right)\chi = \underbrace{f_0\left[-\boldsymbol{V_g}\cdot\boldsymbol{\nabla_p}(\zeta_g + f)\right]}_{\text{Term A: Propagation Term}} - \underbrace{\frac{f_0^2}{\sigma}\frac{\partial}{\partial p}\left[\frac{R_d}{p}\left(-\boldsymbol{V_g}\cdot\boldsymbol{\nabla_p}T\right)\right]}_{\text{Term B: Amplification Term}} \quad (2)$$

4.2 5–7 June 2009 anomalous Greenland ice-melt event

Two lists of dates corresponding to the starting day of events from the 10th percentile and events from the 90th percentile of the standardized Greenland ice-melt anomaly were created. One event from each list was randomly selected as a representative case study. A 10th percentile of standardized Greenland ice-melt anomaly event (Fig. 26a) is randomly selected: 5–7 June 2009 (Fig. 28). The event is associated with a cyclone initially located over western Canada on 0000 UTC 28 May 2009 that tracked to the eastern coast of Newfoundland on 1200 UTC 5 June 2009 (Fig. 29). The cyclone intensified and tracked along the southern tip of Hudson Bay into Newfoundland, reaching its peak intensity on 0000 UTC 3 June 2009 (Fig. 30). Between 0000 UTC 3 June 2009 and 0000 UTC 6 June 2009, the cyclone moved slowly to the northeast over the eastern shore of Newfoundland, as shown by the shorter 24 h distance increments traveled by the cyclone relative to earlier times (Fig. 29). The slow northeastward movement of the cyclone is associated with a 700-hPa trough over Newfoundland (Fig. 31). The 700-hPa trough is associated with weak poleward-directed warm-air advection over the western coast of Greenland, and positive 700-hPa standardized temperature anomaly values over southern Greenland (Fig. 32). The standardized Greenland ice-melt anomaly reached ~+1.1 sigma on 0000 UTC 5 June 2009 (Fig. 28). The amplitude of the flow pattern at 300-hPa during the event is characterized as

high i.e., sectorial sinuosity greater than or equal to 3 (Fig. 33). This event is associated with 300-hPa ridge amplification over southern Greenland, resulting in a flow pattern that is favorable for the transport of warm air poleward (Fig. 34). The evolution of the event is discussed below.

This event is associated with an area-averaged 700-hPa temperature value of −6.5 °C (Fig. 26a), which corresponds to a value of the thermal metric, defined in section 3.2.2, of +0.5. This value of the thermal metric corresponds to the mean value of the area-averaged values of the standardized 700-hPa temperature anomaly for all the days in the event.

2 days prior to the standardized Greenland ice-melt anomaly event, on 0000 UTC 3 June 2009, a 1000 hPa surface cyclone over Newfoundland is located downstream of a 300-hPa trough over eastern Canada and upstream of an amplified negatively tilted ridge over southern Greenland (Figs. 30 and 34). The location of the cyclone relative to the amplified 300-hPa negatively tilted ridge is favorable for the transport of warm air poleward into Greenland. At 300-hPa, ridge amplification over Greenland that occurred starting on 0000 UTC 3 June 2009 is quantified in terms of the increase in sectorial sinuosity (Fig. 33) and is dominated by geopotential height tendency forcing from the amplification term (Term B) (Figs. 34, 35, and 36). At 0000 UTC 3 June 2009, the sectorial sinuosity value was 2.3 (Fig. 33), at the 70th percentile of climatology (Fig. 34), corresponding to a medium-amplitude flow pattern. The QG geopotential height tendency forcing associated with this medium-amplitude flow pattern shows negative values of Term B (Fig. 35) along the poleward side of the 300-hPa ridge to the northeast of Hudson Bay and extending onto the western coast of Greenland. The negative values of Term B imply 300-hPa geopotential height rises and ridge amplification. The evolution of the amplitude of the ridge is quantified in terms of sectorial sinuosity, shown in Fig. 33, which indicates an increase in sectorial sinuosity from 2.3 on 0000 UTC 3 June 2009 to 3.7 on the day of the standardized Greenland ice-

melt anomaly event, on 1200 UTC 5 June 2009. At 700-hPa, a ridge over southern Greenland is collocated with a positive standardized temperature anomaly of +2 sigma (Fig. 32). Poleward-directed warm-air advection of 0.4 °C h^{-1} along the poleward side of the 700-hPa ridge is located over the western coast of Greenland (Fig. 31).

During the standardized Greenland ice-melt anomaly event on 1200 UTC 5 June 2009, the surface cyclone extending between the southern tip of Hudson Bay and the eastern coast of Newfoundland, collocated with a 300-hPa cutoff trough and upstream of a 300-hPa cutoff ridge over southeastern Greenland (Figs. 37 and 38), weakened from 1000 hPa at 0000 UTC 3 June 2009 to 1008 hPa at 1200 UTC 5 June 2009. The location of the surface cyclone relative to the 300-hPa cutoff trough and the 300-hPa cutoff ridge is favorable for the transport of warm air poleward into Greenland. At 300-hPa, ridge amplification over Greenland that occurred in the previous 2,5 days starting on 0000 UTC 3 June 2009 is quantified in terms of an increase in sectorial sinuosity (Fig. 39) and is dominated by geopotential height tendency forcing from the amplification term (Term B) (Figs. 38, 40, and 41). At 1200 UTC 5 June 2009, the sectorial sinuosity value was 3.7 (Fig. 39), at the 95th percentile of climatology (Fig. 41), corresponding to a high-amplitude flow pattern. This high-amplitude flow pattern is associated with 300-hPa ridge amplification and is concurrent with a 300-hPa blocking ridge situated over southeastern Greenland (Fig. 40). At 700-hPa, a cutoff ridge over southeastern Greenland is associated with a positive standardized temperature anomaly of +1 sigma over southern Greenland (Fig. 42). Poleward-directed warm-air advection of 0.3 °C h^{-1} along the poleward side of the 700-hPa cutoff ridge is located over the western coast of Greenland (Fig. 43). This positive temperature anomaly is concurrent with an anomalous Greenland ice-melt anomaly reaching ~+1.1 sigma on 1200 UTC 5 June 2009 (Fig. 28). All of the days from the 5–7 June 2009 event correspond to the characteristic 300-hPa geopotential height

pattern identified by SOMs node 3 (node 9 from Fig. 15) from group 3, consisting of a high-amplitude omega block ridge pattern over Greenland (Fig. 44).

4.3 9–15 April 2016 anomalous Greenland ice-melt event

A 90th percentile of standardized Greenland ice-melt anomaly event (Fig. 26b) is randomly selected: 9–15 April 2016 (Fig. 45). The event is associated with three surface cyclones (Fig. 46). One surface cyclone was initially located over western Canada on 0000 UTC 5 April 2016 and tracked to the Labrador Sea by 0000 UTC 12 April 2016. This surface cyclone intensified and tracked from southern Michigan on 0000 UTC 7 April 2016 into northern New York on 0000 UTC 8 April 2016, concurrent with a blocking surface anticyclone to its east over the North Atlantic (Fig. 47). A strong pressure gradient that is favorable for strong southerly flow and the transport of warm air poleward set up between the blocking surface anticyclone and the surface cyclone to its west. A second, quasi-stationary surface cyclone located at the southern tip of Greenland (Fig. 47) is associated with 700-hPa poleward-directed warm-air advection over the southeastern coast of Greenland at 0000 UTC 8 April 2016 (Fig. 48). Between 0000 UTC 8 April 2016 and 0000 UTC 10 April 2016, the surface cyclone over northern New York moved slowly to the northeast over Newfoundland, while the surface cyclone over the southern tip of Greenland moved east into the North Atlantic (Fig. 49). A third cyclone located to the south of Nova Scotia is concurrent with the surface cyclone over Newfoundland (Fig. 49). The blocking surface anticyclone extends poleward into southern Greenland and is located to the east of the surface cyclone to the south of Nova Scotia and the surface cyclone over Newfoundland.

By 0000 UTC 12 April 2016, the surface cyclone that was over Newfoundland at 0000 UTC 10 April 2016 tracked north into the Labrador Sea concurrent with the blocking surface anticyclone, which split into two surface anticyclones, one off the eastern coast of Nova Scotia

and one over southeastern Greenland (Fig. 50). A strong pressure gradient set up between the blocking surface anticyclone over southeastern Greenland and the surface cyclone to its west in the Labrador Sea. The strong pressure gradient was favorable for strong southerly flow concurrent with 700-hPa poleward-directed warm-air advection (Fig. 51) and with larger positive 700-hPa standardized temperature anomaly values over all of Greenland (Fig. 52) relative to those in the previous case study (Fig. 42). The temperature anomaly values in the present case study are concurrent with a standardized Greenland ice-melt anomaly reaching ~+5.7 sigma on 0000 UTC 12 April 2016 (Fig. 45) compared with the ~+1.1 sigma value from the previous case study (Fig. 28). The amplitude of the 300-hPa flow pattern was characterized as medium, i.e., sectorial sinuosity values between 2 and 3 (Fig. 53). This event is associated with 300-hPa ridge amplification over southern Greenland, resulting in a flow pattern that is favorable for the transport of warm air poleward. The evolution of the event is discussed below.

This event is associated with an area-averaged 700-hPa temperature value of −8.7°C (Fig. 26b), which corresponds to a relatively high mean value of the thermal metric of +1.7 compared to events from the 10th percentile of standardized Greenland ice-melt anomaly with values of the thermal metric not exceeding +1 sigma (Fig. 26a).

1 day prior to the ice-melt event, on 0000 UTC 8 April 2016, a 992 hPa surface cyclone is located over northern New York downstream of a 300-hPa trough (Figs. 47 and 54). This surface cyclone is associated with a negatively tilted 300-hPa trough–ridge pattern and is concurrent with a 1040 hPa blocking surface anticyclone over the North Atlantic. A strong pressure gradient sets up on the eastern (western) flank of the surface cyclone (surface anticyclone) that is favorable for strong southerly flow and the transport of warm air poleward. A quasi-stationary 984 hPa surface cyclone located at the southern tip of Greenland (Fig. 47) is collocated with the base of a 300-hPa

cutoff trough (Figs. 47 and 54). This surface cyclone is associated with a negatively tilted 300-hPa trough–ridge pattern that is favorable for the transport of warm air poleward over the northern half of Greenland. At 300-hPa, ridge amplification over Greenland that occurred starting on 0000 UTC 8 April 2016 is quantified by an increase in sectorial sinuosity (Fig. 53) and is dominated by geopotential height tendency forcing from the amplification term (Term B) (Figs. 54, 55, and 56). At 0000 UTC 8 April 2016, the sectorial sinuosity value was 1.6 (Fig. 53), corresponding to the 42.5 percentile of climatology (Fig. 56) and a low-amplitude flow pattern. The QG geopotential height tendency forcing associated with this low-amplitude flow pattern shows negative values of Term B (Fig. 55) along the poleward side of a 300-hPa ridge over Newfoundland and extending east into the North Atlantic. The negative values of Term B imply 300-hPa geopotential height rises and ridge amplification. The evolution of the amplitude of the ridge is quantified in terms of sectorial sinuosity (Fig. 53), which increases from 1.6 on 0000 UTC 8 to April 2016 to 2.5 on the first day of the standardized Greenland ice-melt anomaly event, on 0000 UTC 9 April 2016. At 700-hPa, a trough over southeastern Greenland and a ridge over eastern Greenland are associated with a positive standardized temperature anomaly of +2 sigma over northern Greenland (Fig. 57). Poleward-directed warm-air advection of 0.4 °C h^{-1} upstream of the 700-hPa ridge is located over the southeastern coast of Greenland (Fig. 48).

During the ice-melt event, on 0000 UTC 10 April 2016, the 992 hPa surface cyclone located over northern New York on 0000 UTC 8 April 2016 (Fig. 47) tracked to the northeast over Newfoundland and weakened to 1000 hPa (Fig. 49). The progression of the cyclone to the northeast coincides with the amplification of the 300-hPa trough–ridge pattern as the trough deepens equatorward into the mid-Atlantic states and the ridge builds poleward over southern Greenland (Fig. 58). This 300-hPa trough–ridge pattern is favorable for the transport of warm air

poleward into southern Greenland. The surface cyclone over the southern tip of Greenland weakened from 984 hPa on 0000 UTC 8 April 2016 to 1000 hPa on 0000 UTC 10 April and moved east over the North Atlantic (Fig. 49). A third surface cyclone is located to the south of Nova Scotia downstream of the deepening 300-hPa trough (Fig. 49). This surface cyclone was concurrent with the surface cyclone over Newfoundland. A 1032 hPa blocking surface anticyclone over the North Atlantic extended poleward into southern Greenland and is located to the east of the two surface cyclones (Fig. 49). The presence of a blocking surface anticyclone concurrent with the two cyclones to its west enhances the pressure gradient and is favorable for strong southerly flow and the transport of warm air poleward. At 300-hPa, ridge amplification over Greenland, which occurred during the previous 2 days starting on 0000 UTC 8 April 2016, is quantified by an increase in sectorial sinuosity (Fig. 59) and is dominated by geopotential height tendency forcing from the amplification term (Term B) (Figs. 58, 60, and 61). At 0000 UTC 10 April 2016, the sectorial sinuosity value was 2.2 (Fig. 59), corresponding to the 87.5 percentile of climatology (Fig. 61) and a medium-amplitude flow pattern. The QG geopotential height tendency forcing associated with this medium-amplitude flow pattern shows large negative values of Term B (Fig. 60) along a portion of the poleward side of the 300-hPa ridge situated over the Labrador Sea and extending east over the western coast of Greenland. The negative values of Term B imply 300-hPa geopotential height rises and ridge amplification. The evolution of the amplitude of the ridge is quantified in terms of sectorial sinuosity (Fig. 59), which increases from 1.6 on 0000 UTC 8 April 2016 to 2.2 during the second day of the Greenland ice-melt event, on 0000 UTC 10 April 2016, and corresponds to a medium-amplitude flow pattern. This medium-amplitude flow pattern is associated with ridge amplification over Greenland during the previous 2 days. At 700-hPa, a ridge over southeastern Greenland is associated with a positive standardized temperature anomaly of +2

sigma (Fig. 62) that extends over southern and eastern Greenland and is larger than the positive standardized temperature anomaly of +1 sigma from the previous case study (Fig. 42). Strong poleward-directed warm-air advection of 0.7 °C h^{-1} (Fig. 63) compared with 0.3 °C h^{-1} from the previous case study (Fig. 43) is located upstream of the 700-hPa ridge axis and extends over the southwestern coast of Greenland into central Greenland. The aforementioned positive temperature anomaly of +2 sigma (Fig. 62) is concurrent with a standardized Greenland ice-melt anomaly reaching ~+5.7 sigma on 0000 UTC 10 April 2016 (Fig. 45). All of the days from the 9–15 April 2016 event correspond to the characteristic 300-hPa geopotential height pattern identified by SOMs node 3 (node 6 from Fig. 15) from group 2, consisting of a medium-amplitude trough–ridge pattern over Greenland (Fig. 64).

During the ice-melt event, on 0000 UTC 12 April 2016, the surface cyclones located over Newfoundland and to the south of Nova Scotia on 0000 UTC 10 April 2016 (Fig. 49) evolve into a 1008 hPa surface cyclone located over the Labrador Sea west of Greenland (Fig. 50). This 1008 hPa surface cyclone is located over the western coast of Greenland and is concurrent with a 1028 hPa blocking surface anticyclone over southeastern Greenland associated with a 300-hPa blocking ridge over southern Greenland (Fig. 65). This flow pattern is favorable for the transport of warm air poleward over Greenland. At 300-hPa, ridge amplification over Greenland that occurred starting on 0000 UTC 8 April 2016 is quantified by an increase in sectorial sinuosity (Fig. 66) and is dominated at 0000 UTC 12 April 2016 by geopotential height tendency forcing from the amplification term (Term B) (Figs. 65, 67, and 68). At 0000 UTC 12 April 2016, the sectorial sinuosity value was 2.5 (Fig. 66), corresponding to the 95th percentile of climatology (Fig. 68) and a medium-amplitude flow pattern. The QG height tendency forcing associated with this medium-amplitude flow pattern shows negative values of Term B (Fig. 67) along the poleward and eastern

edge of the 300-hPa ridge situated over southern Greenland. The negative values of Term B imply 300-hPa geopotential height rises and ridge amplification. The evolution of the amplitude of the ridge is quantified in terms of sectorial sinuosity (Fig. 66), which increases from 2.2 on 0000 UTC 10 April 2016 to 2.5 on the fourth day of the standardized Greenland ice-melt anomaly event, on 0000 UTC 12 April 2016, and corresponds to a medium-amplitude flow pattern. This medium-amplitude flow pattern is associated with ridge amplification over Greenland during the previous four days. At 700-hPa, a ridge centered over southeastern Greenland is associated with a positive standardized temperature anomaly of +2 sigma that extends over all of Greenland and attains a maximum of +4 sigma over eastern Greenland (Fig. 52). This temperature anomaly is large compared with the +1 sigma temperature anomaly from the previous case study that extends over southern Greenland (Fig. 42). Strong poleward-directed warm-air advection of 0.8 °C h^{-1} (Fig. 51) compared with 0.3 °C h^{-1} from the previous case study (Fig. 43) is located upstream of the 700-hPa ridge axis and extends over the western coast of Greenland. The aforementioned positive standardized temperature anomaly of +2 sigma (Fig. 52) is concurrent with a standardized Greenland ice-melt anomaly reaching ~+4.6 sigma on 0000 UTC 12 April 2016 (Fig. 45).

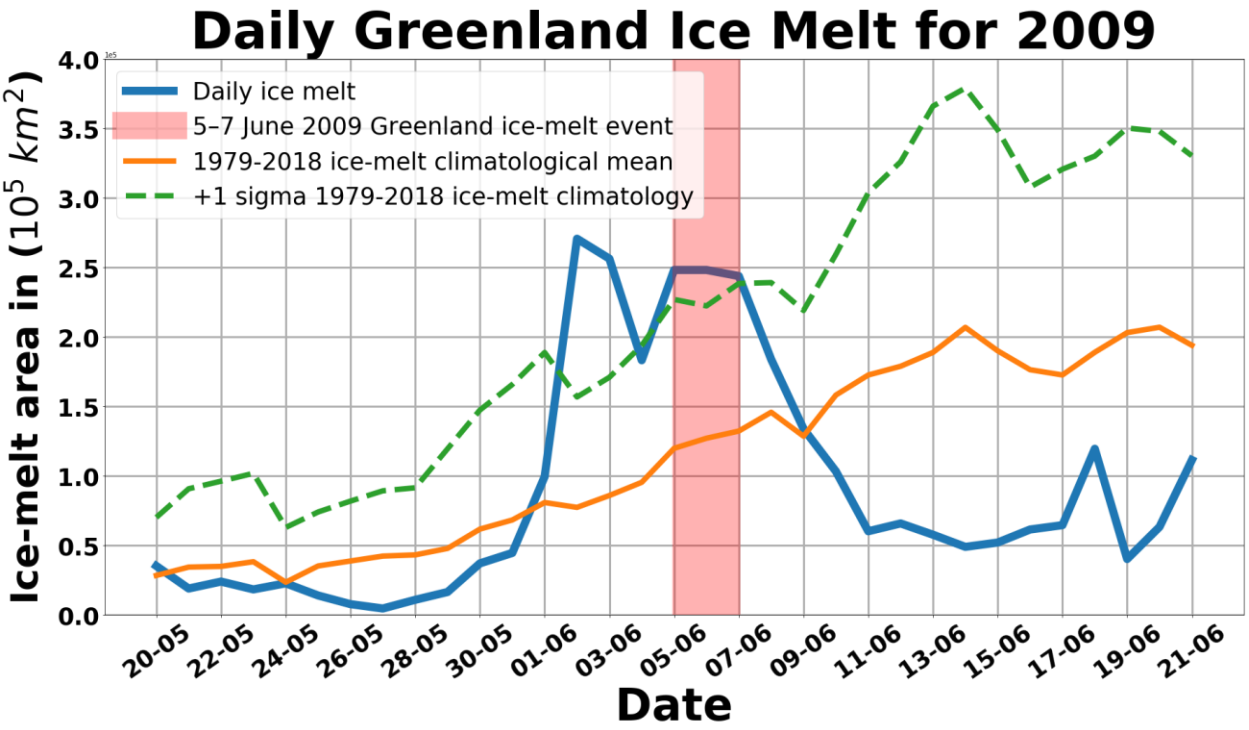

Fig. 28. Daily Greenland ice melt for 2009 (blue curve), 1979–2018 ice-melt climatological mean (orange curve), +1 sigma 1979–2018 ice-melt climatology (dashed green curve), and 5–7 June 2009 Greenland ice-melt event (light red shading).

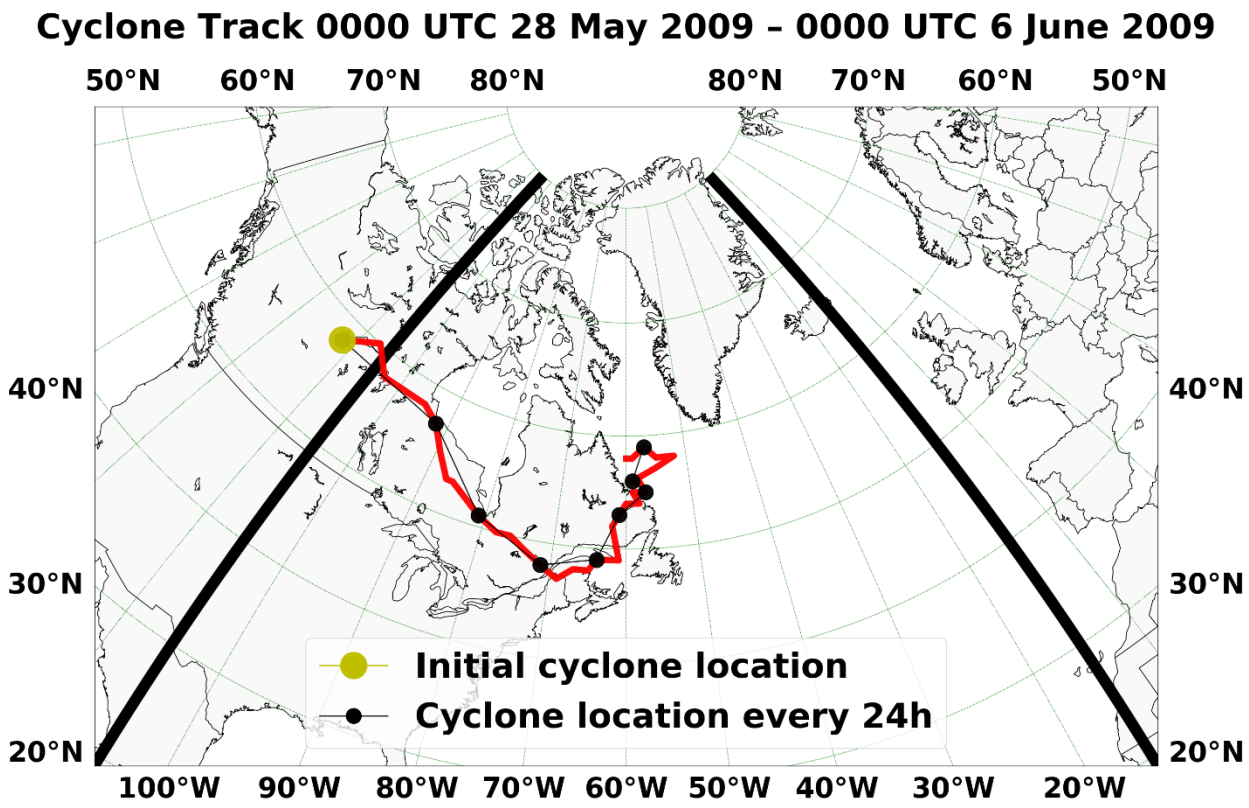

Fig. 29. Cyclone track (red line) for period between 0000 UTC 28 May 2009 and 0000 UTC 6 June 2009, initial cyclone location (yellow dot), and cyclone location every 24 h (black dot).

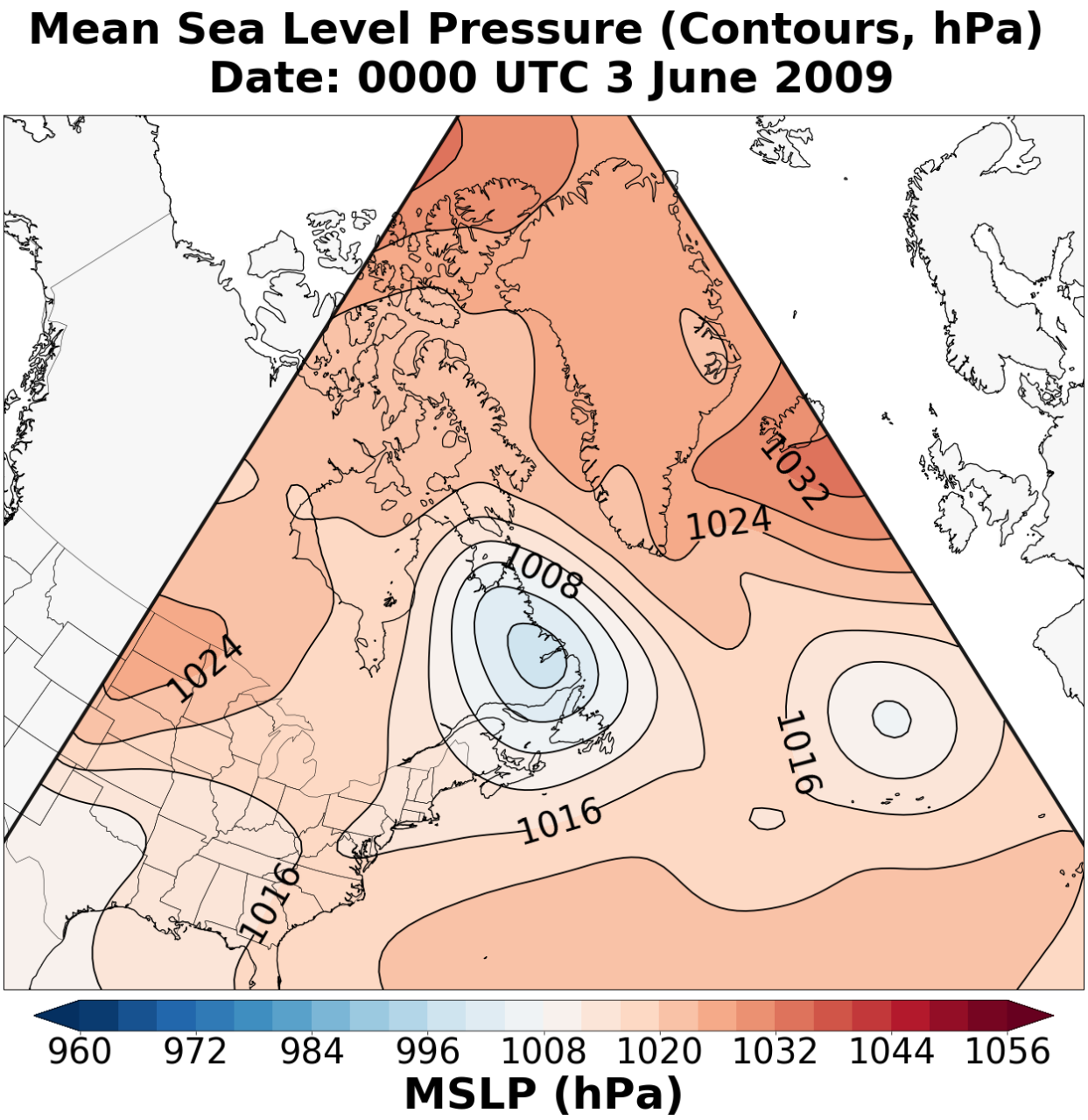

Fig. 30. Mean sea level pressure (contours, hPa) for 0000 UTC 3 June 2009.

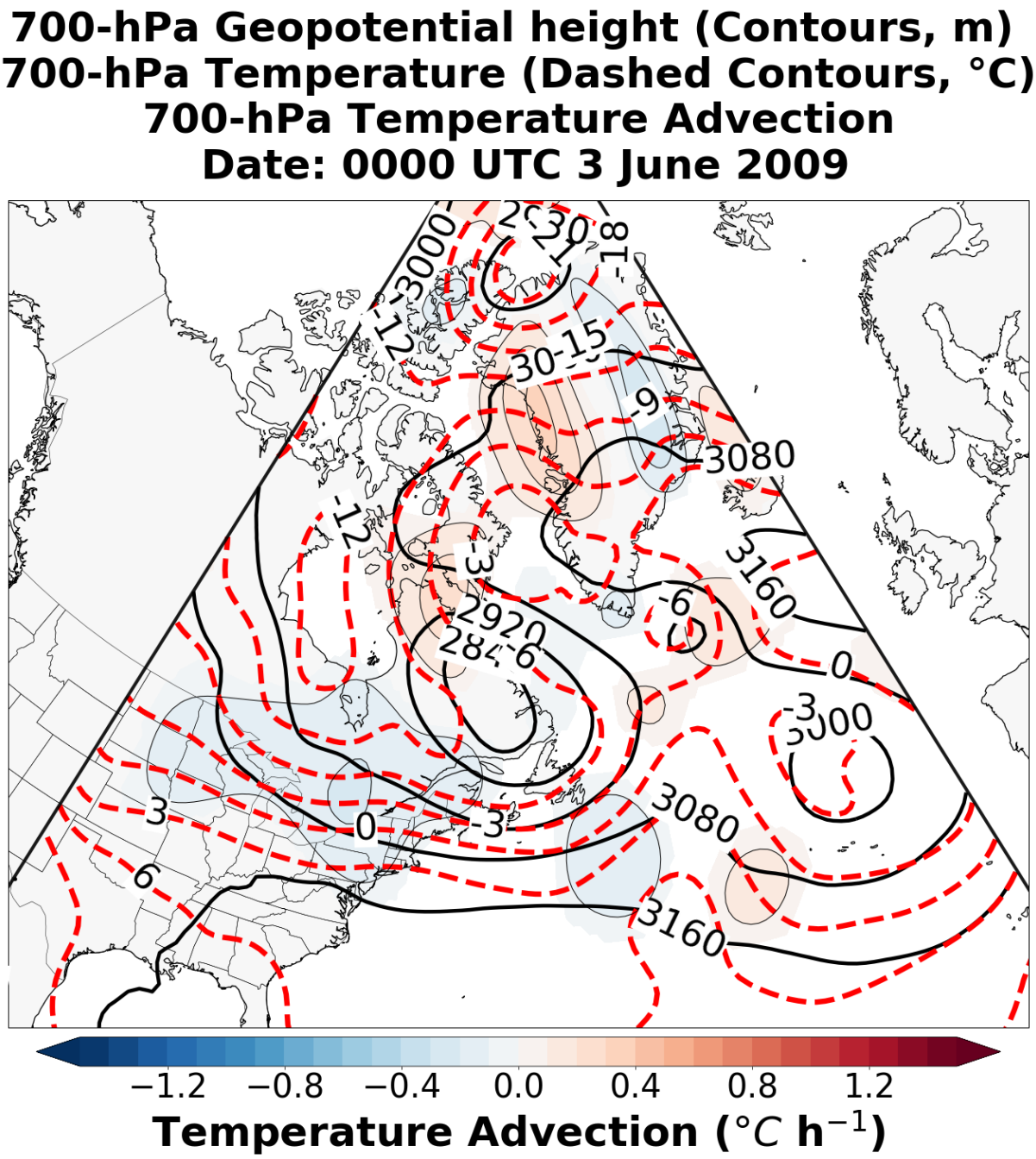

Fig. 31. 700-hPa geopotential height (contours, m), 700-hPa temperature (dashed contours, °C), and 700-hPa temperature advection (°C h^{-1}) for 0000 UTC 3 June 2009.

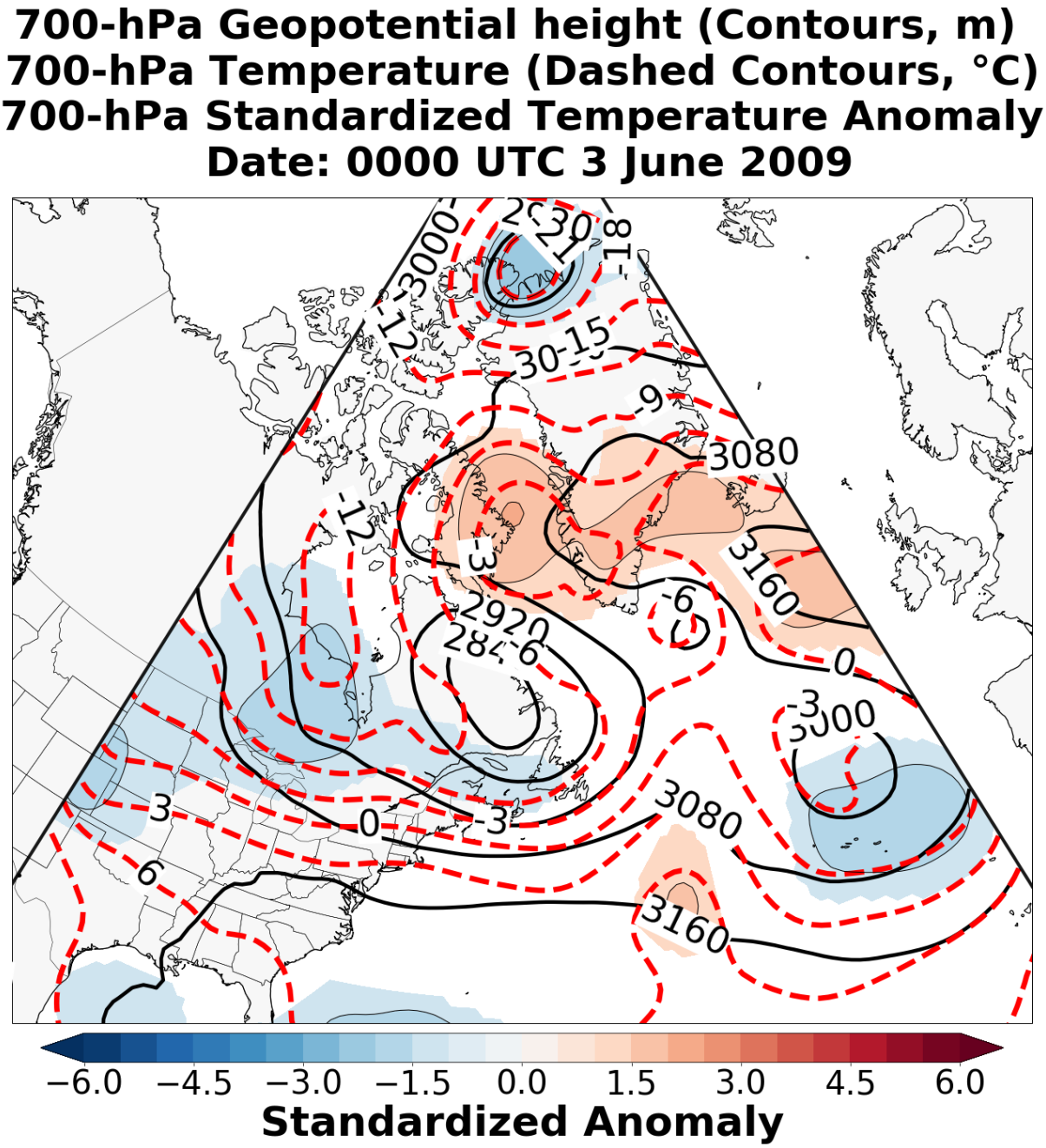

Fig. 32. 700-hPa geopotential height (contours, m), 700-hPa temperature (dashed contours, °C), and 700-hPa standardized temperature anomaly for 0000 UTC 3 June 2009.

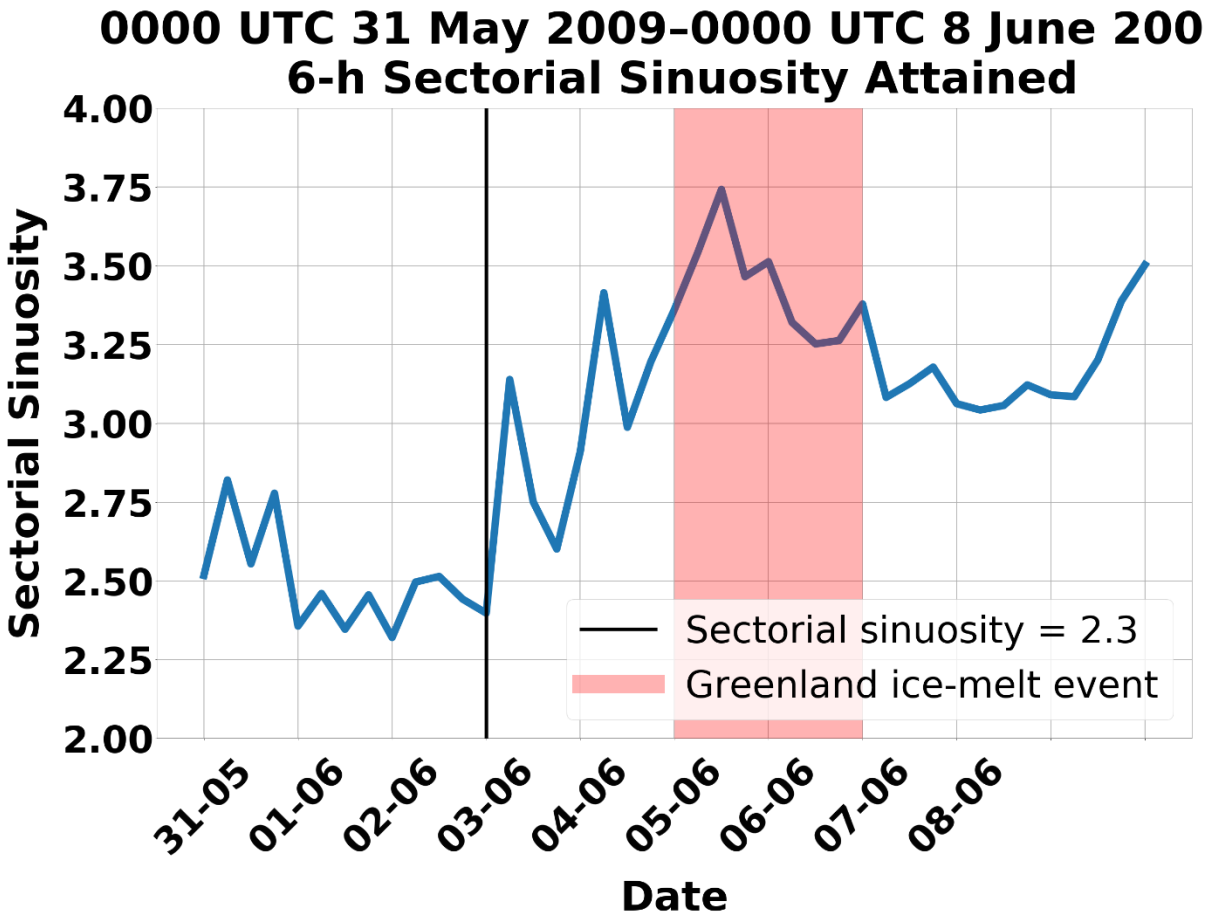

Fig. 33. 6-h sectorial sinuosity (blue curve) for period between 0000 UTC 31 May 2009 and 0000 UTC 8 June 2009, sectorial sinuosity at 0000 UTC 3 June 2009 (vertical black line), and 5–7 June 2009 Greenland ice-melt event (light red shading).

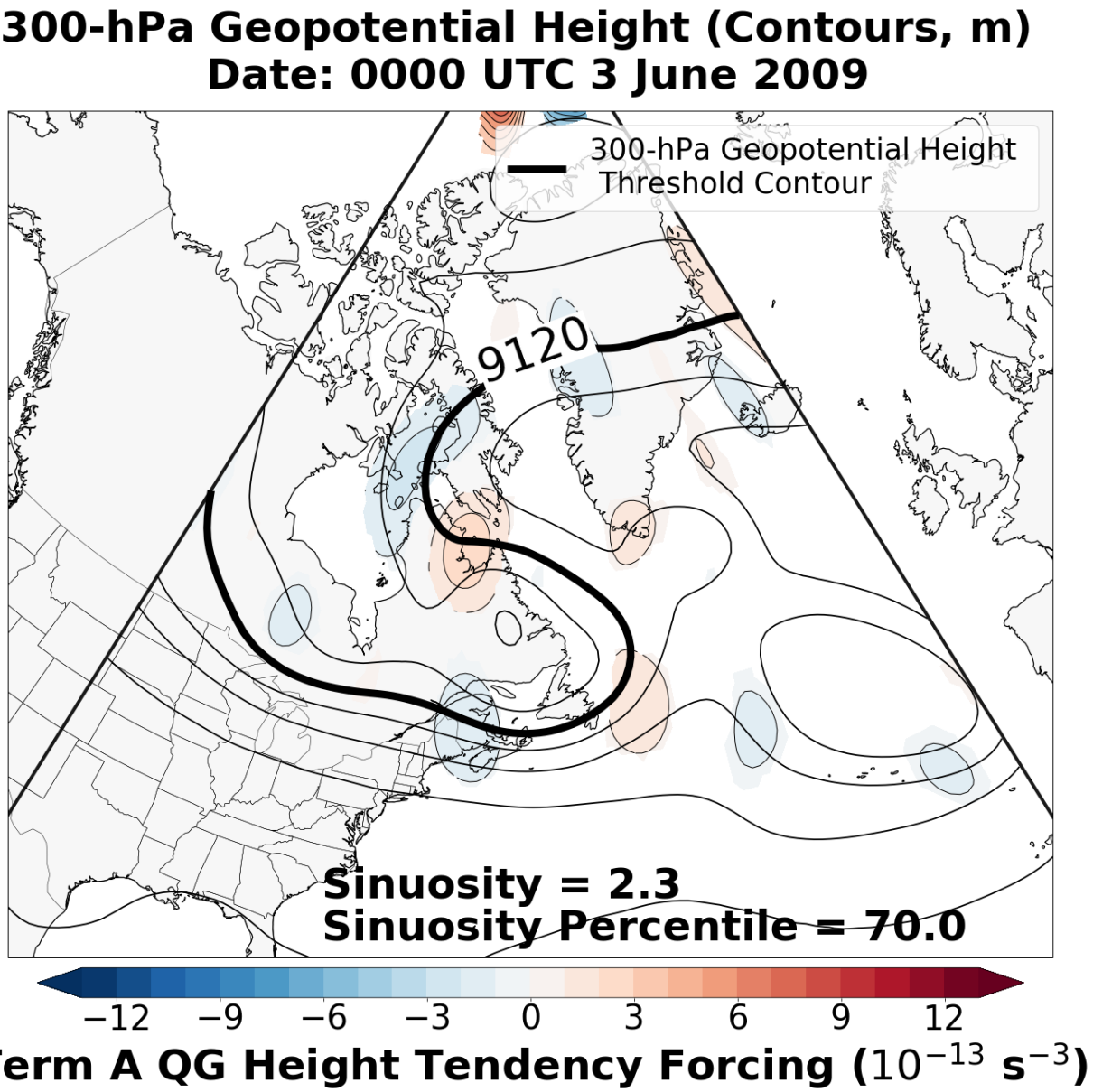

Fig. 34. 300-hPa geopotential height (contours, m), Term A of QG geopotential height tendency forcing (10^{-13} s^{-3}) for 0000 UTC 3 June 2009; positive (negative) forcing is associated with geopotential height falls (rises).

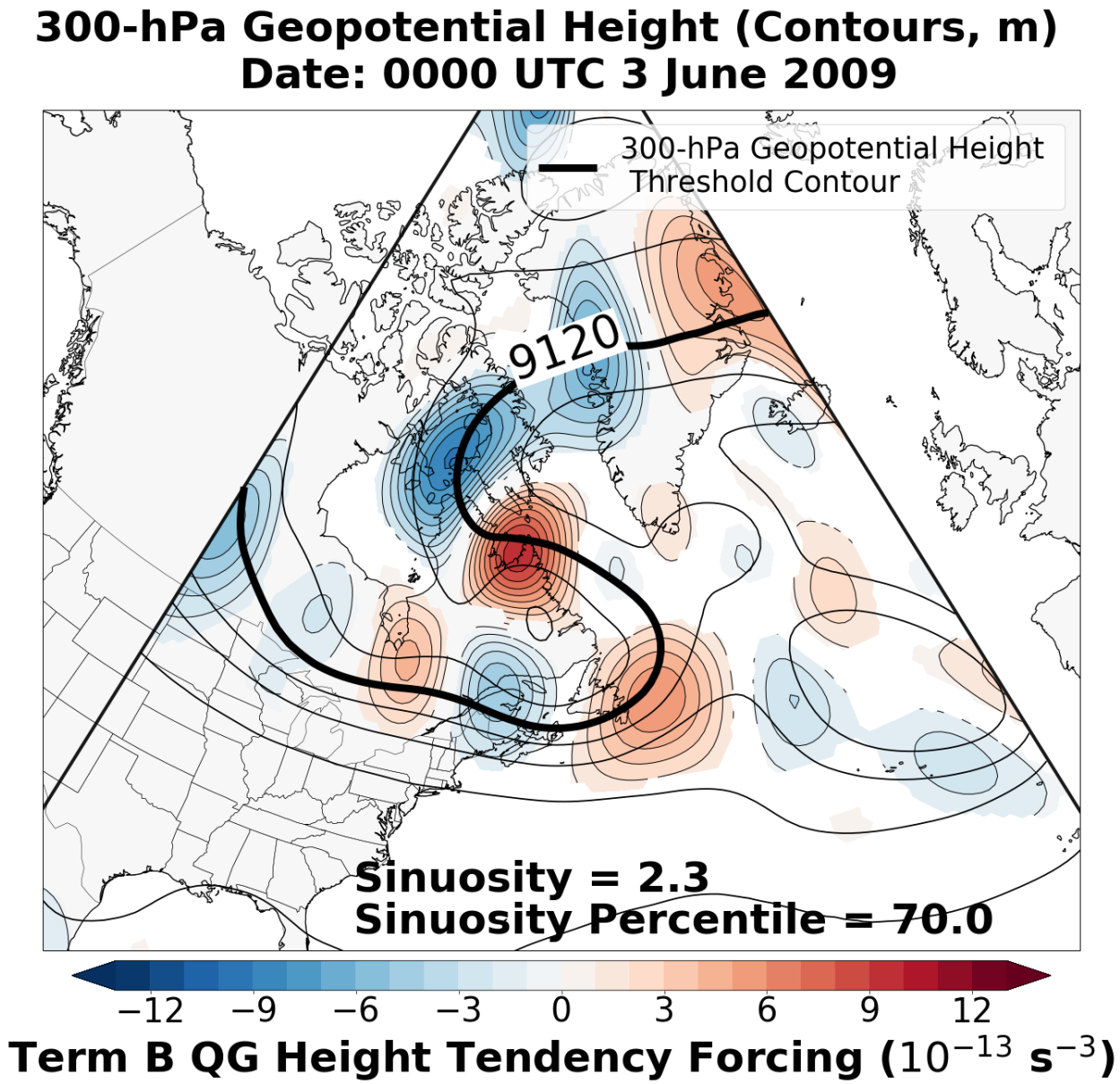

Fig. 35. As in Fig. 34, except for Term B of QG geopotential height tendency forcing ($10^{-13}\,s^{-3}$).

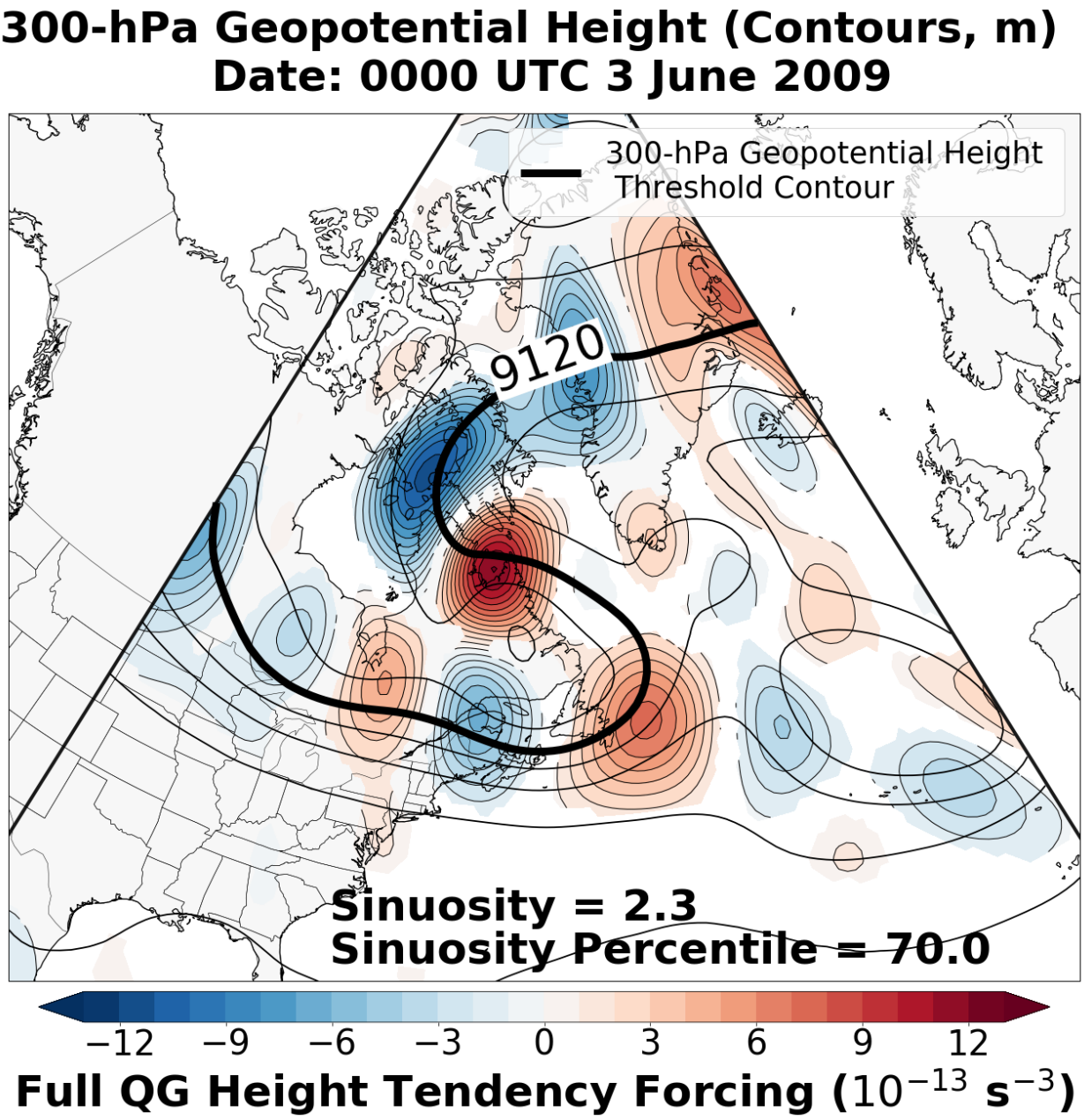

Fig. 36. As in Fig. 34, except for full QG geopotential height tendency forcing ($10^{-13}\,s^{-3}$).

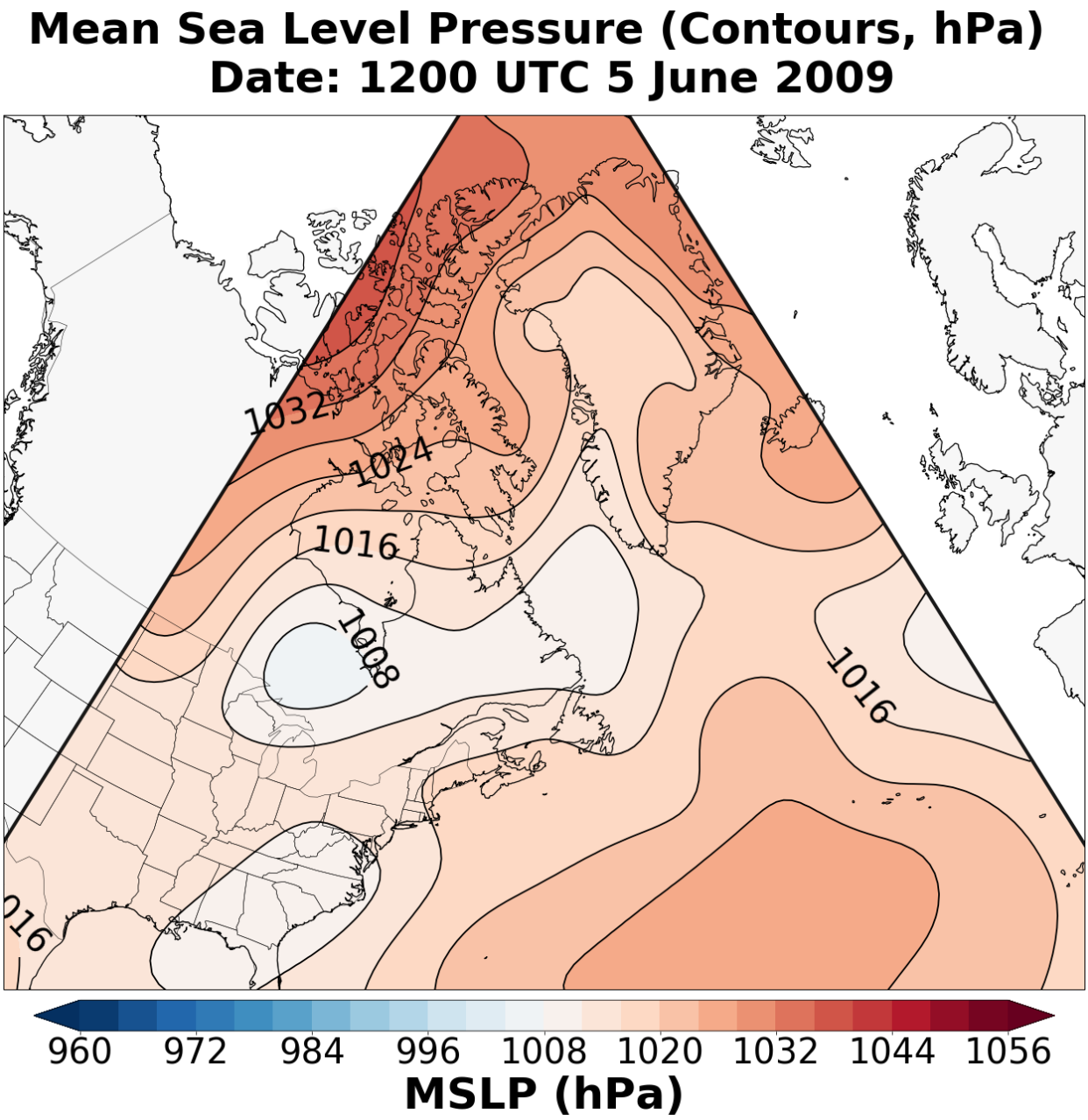

Fig. 37. As in Fig. 30, except for 1200 UTC 5 June 2009.

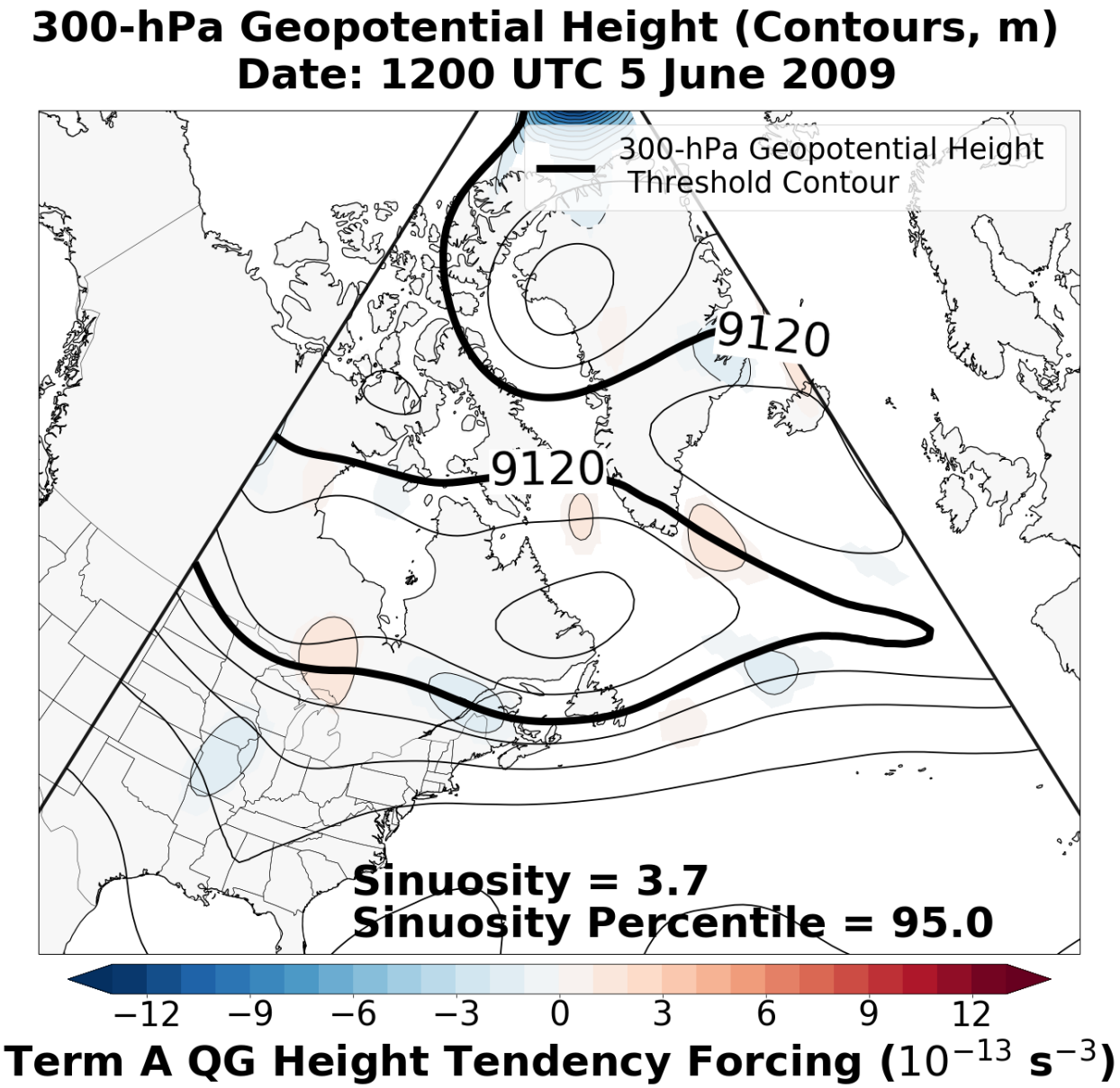

Fig. 38. As in Fig. 34, except for 1200 UTC 5 June 2009.

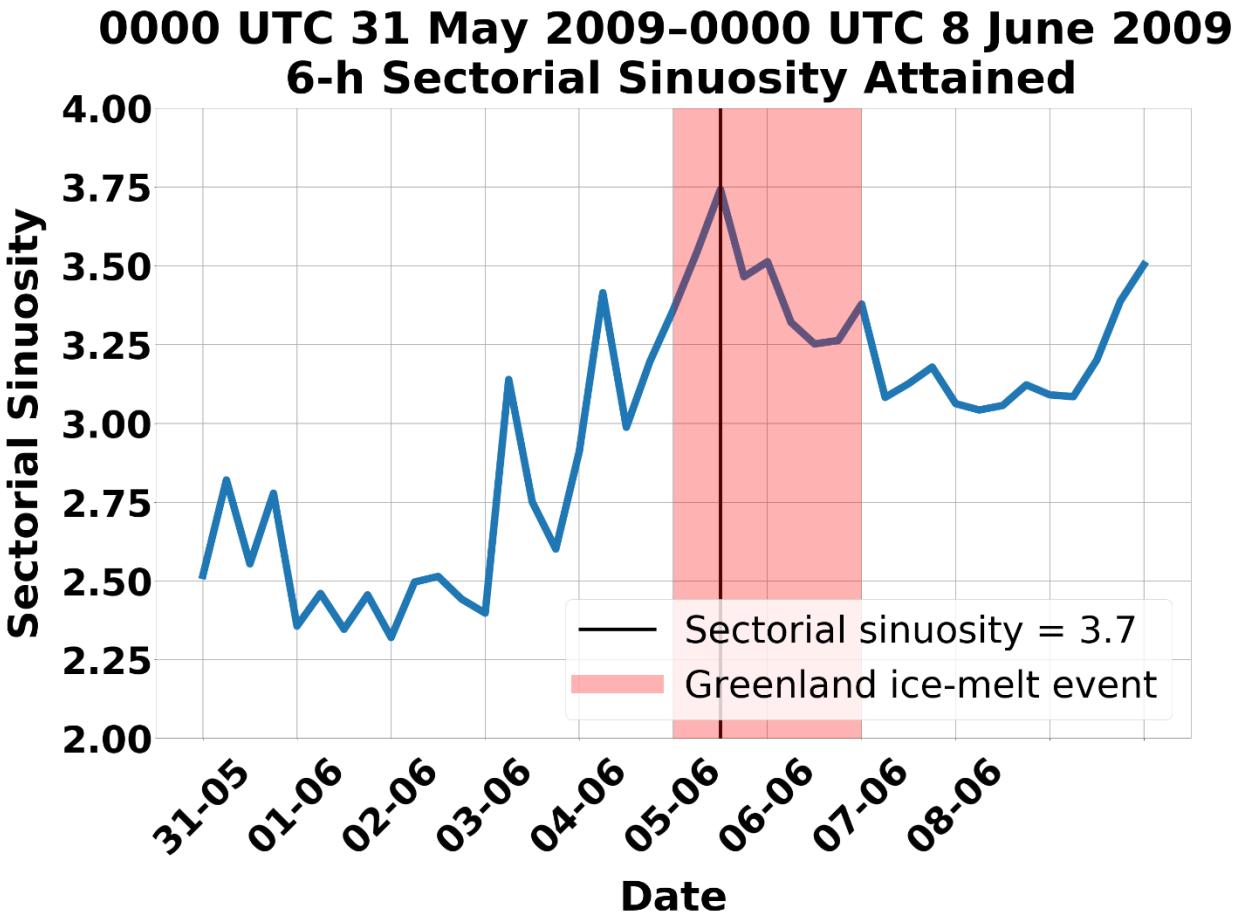

Fig. 39. As in Fig. 33, except for 1200 UTC 5 June 2009.

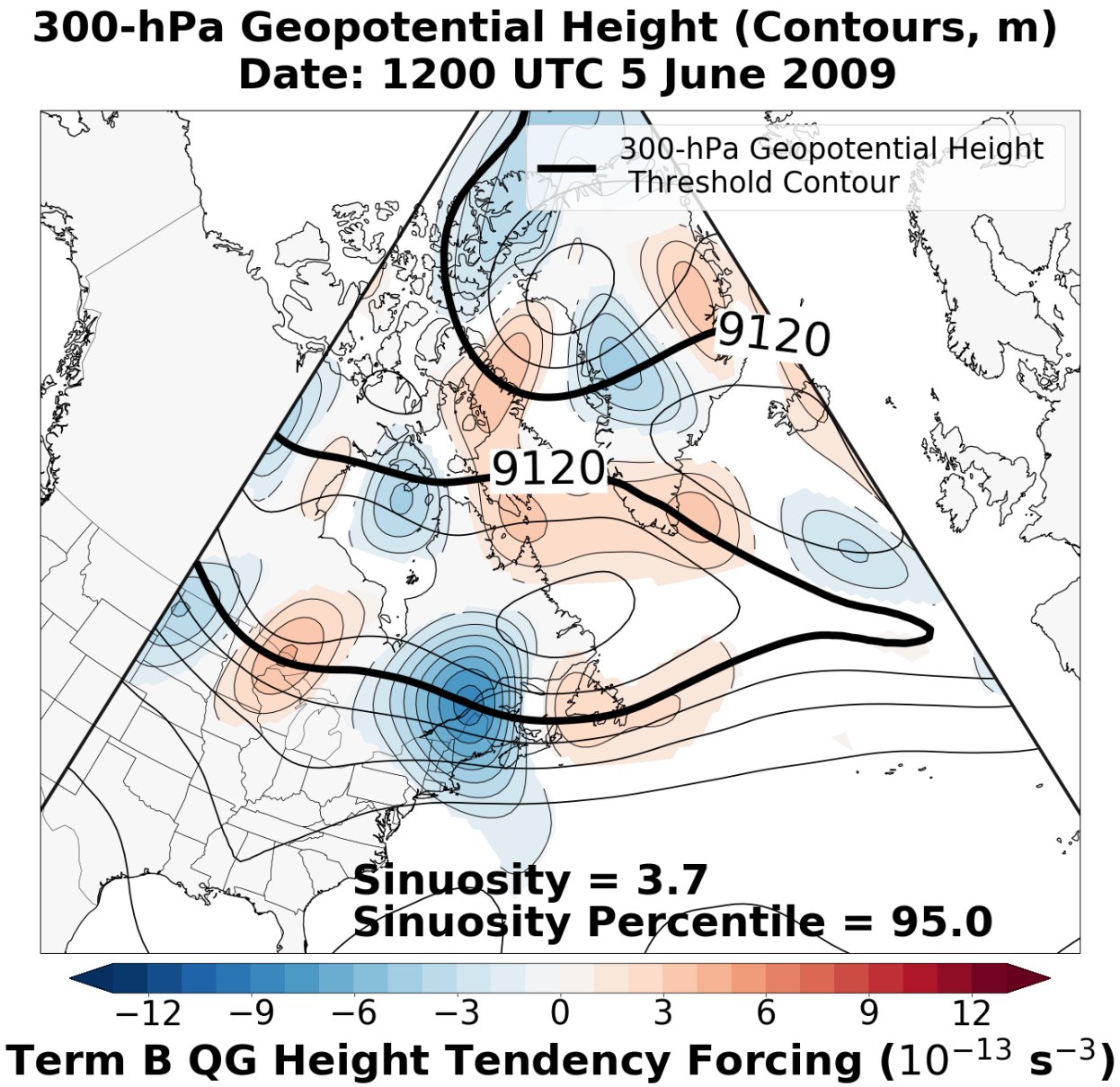

Fig. 40. As in Fig. 35, except for 1200 UTC 5 June 2009.

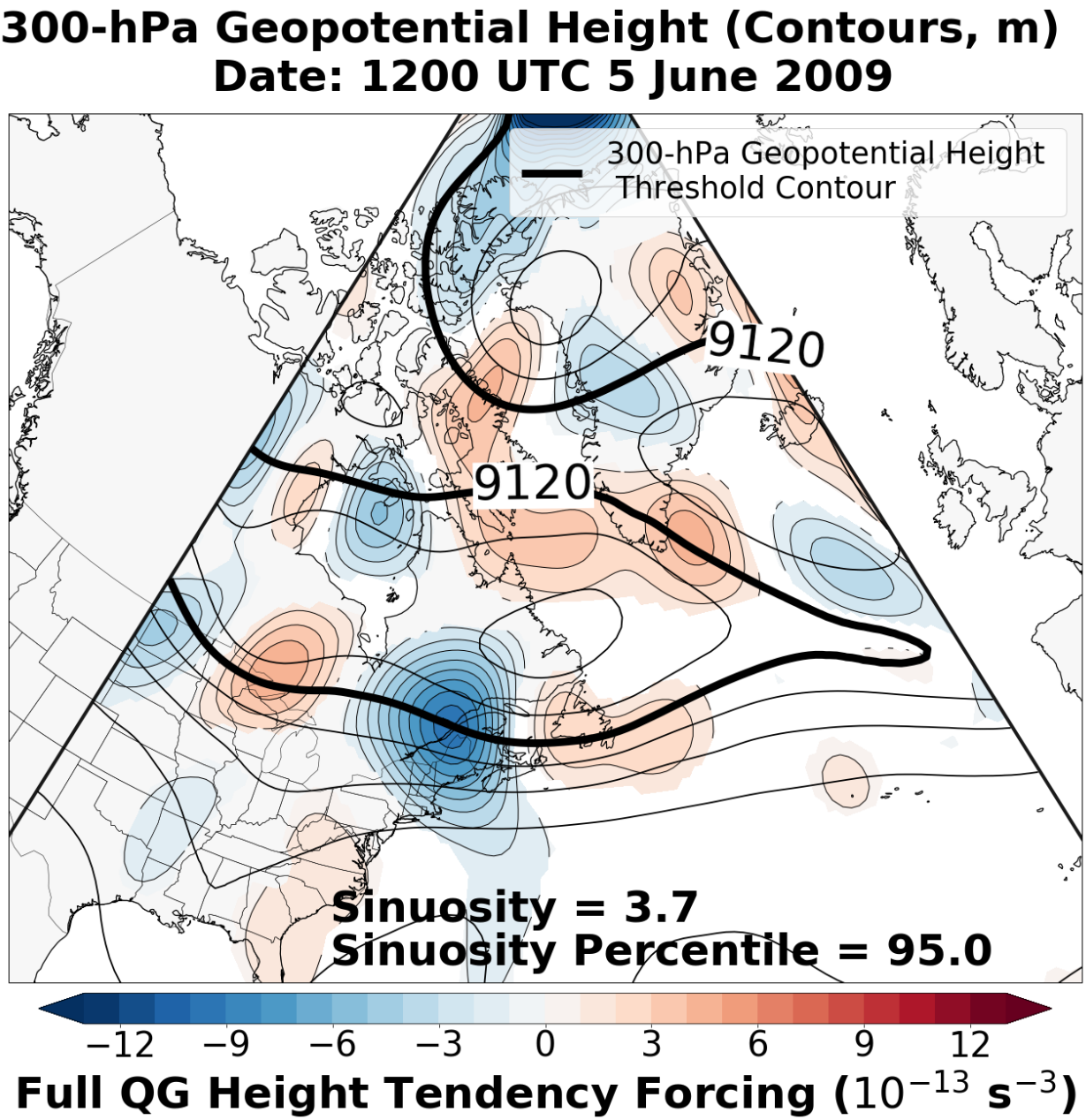

Fig. 41. As in Fig. 36, except for 1200 UTC 5 June 2009.

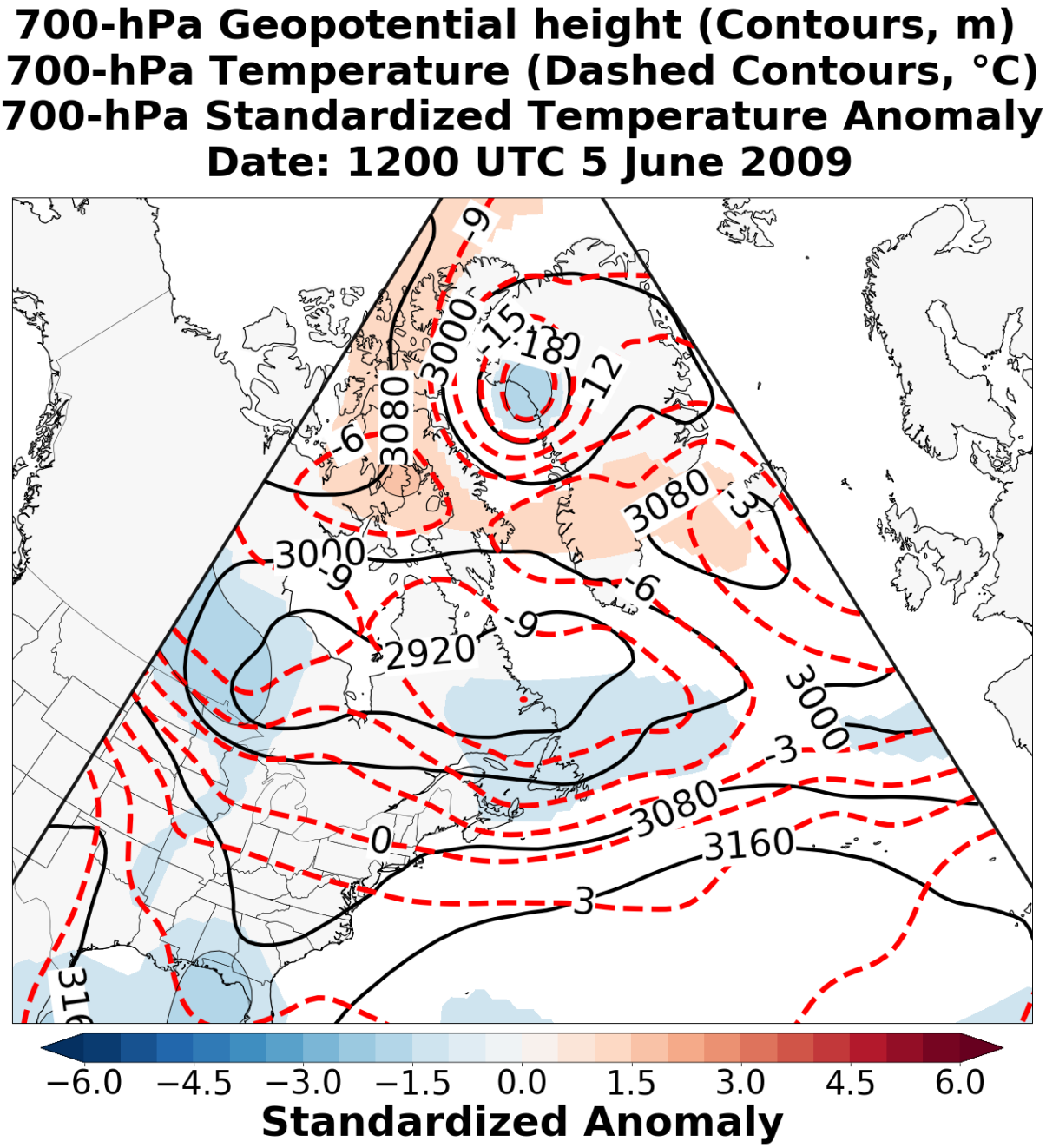

Fig. 42. As in Fig. 35, except for 1200 UTC 5 June 2009.

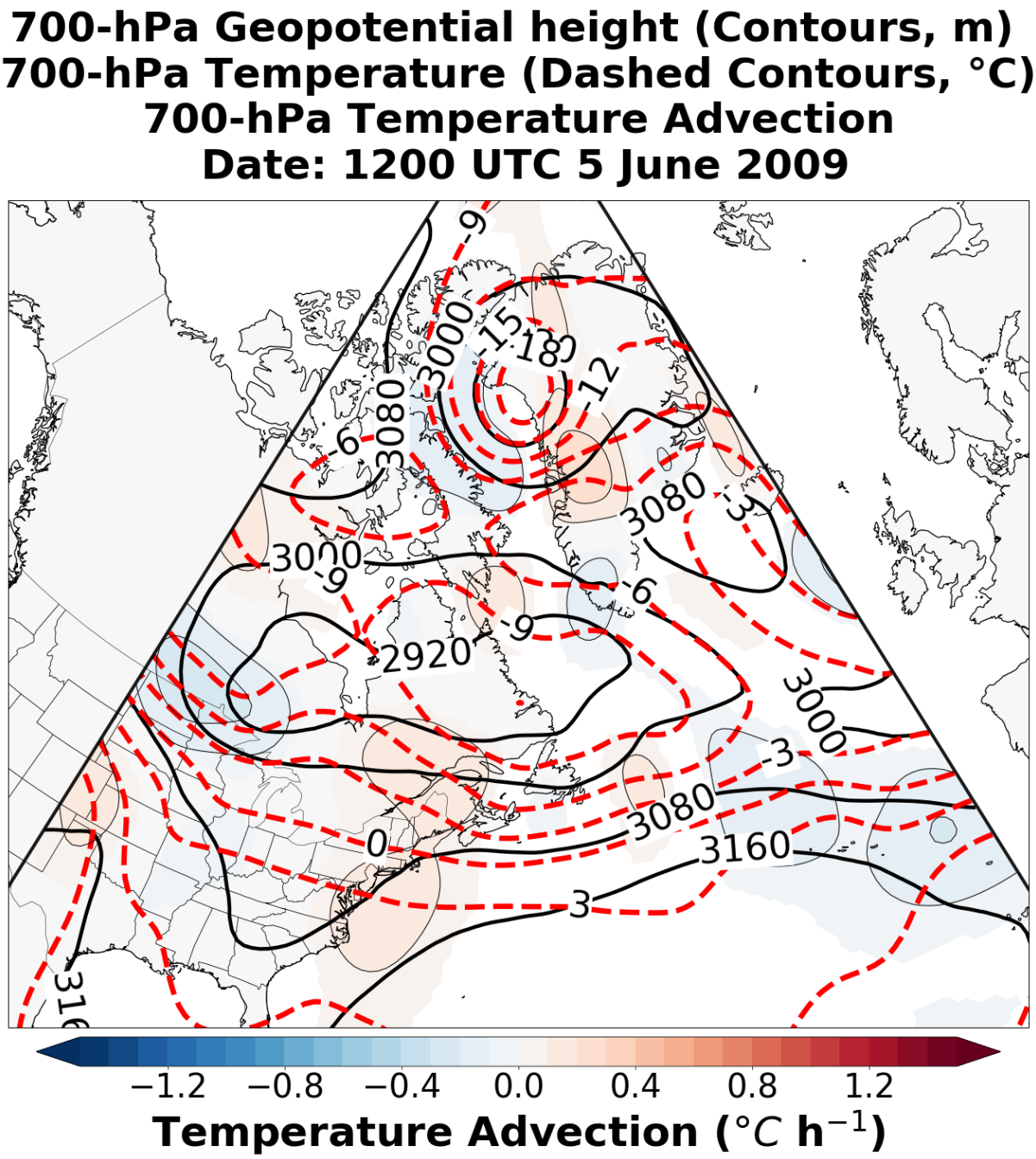

Fig. 43. As in Fig. 31, except for 1200 UTC 5 June 2009.

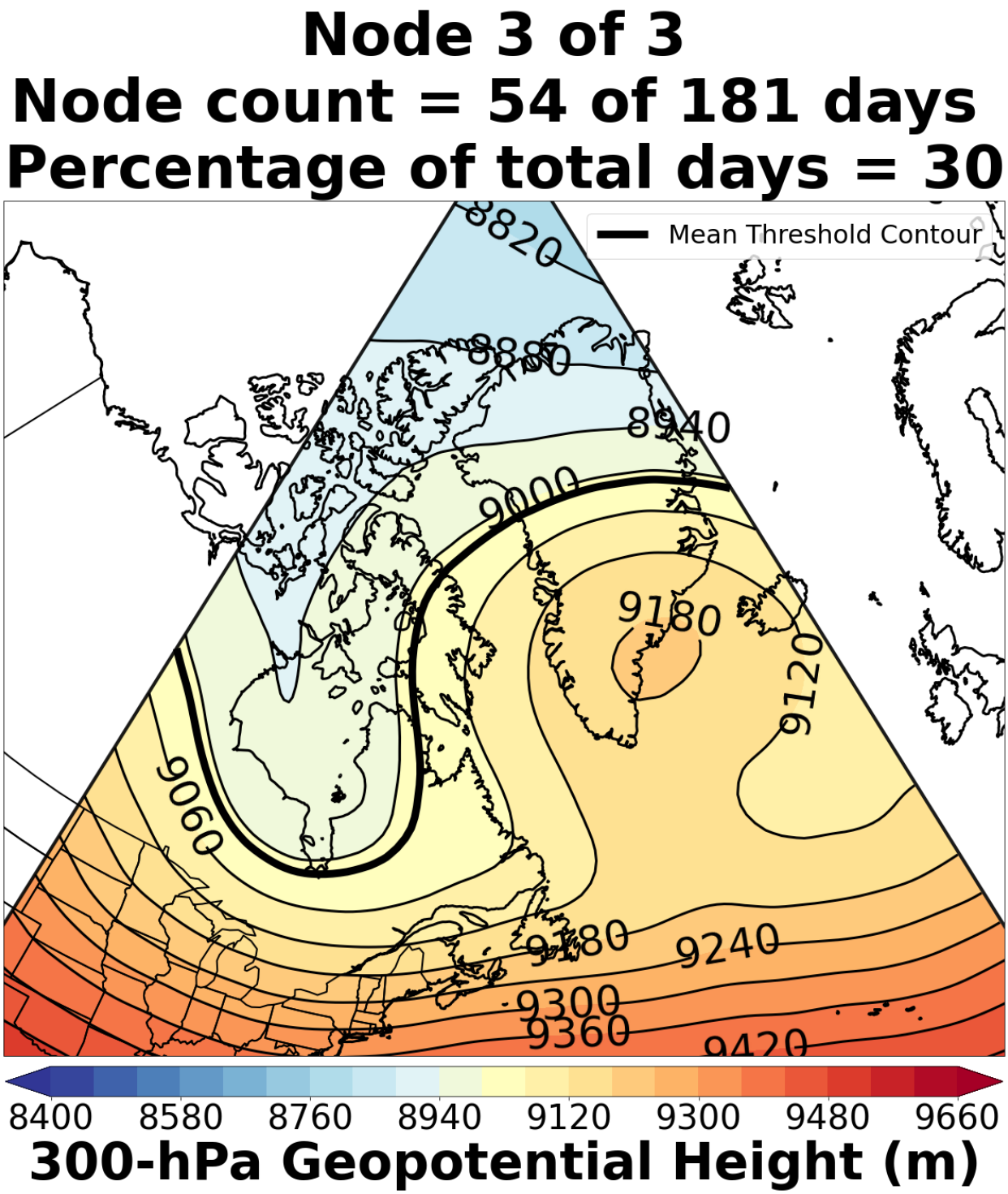

Fig. 44. Node 3 corresponding to sinuosity group 3 of characteristic 300-hPa geopotential height pattern identified by the SOMs.

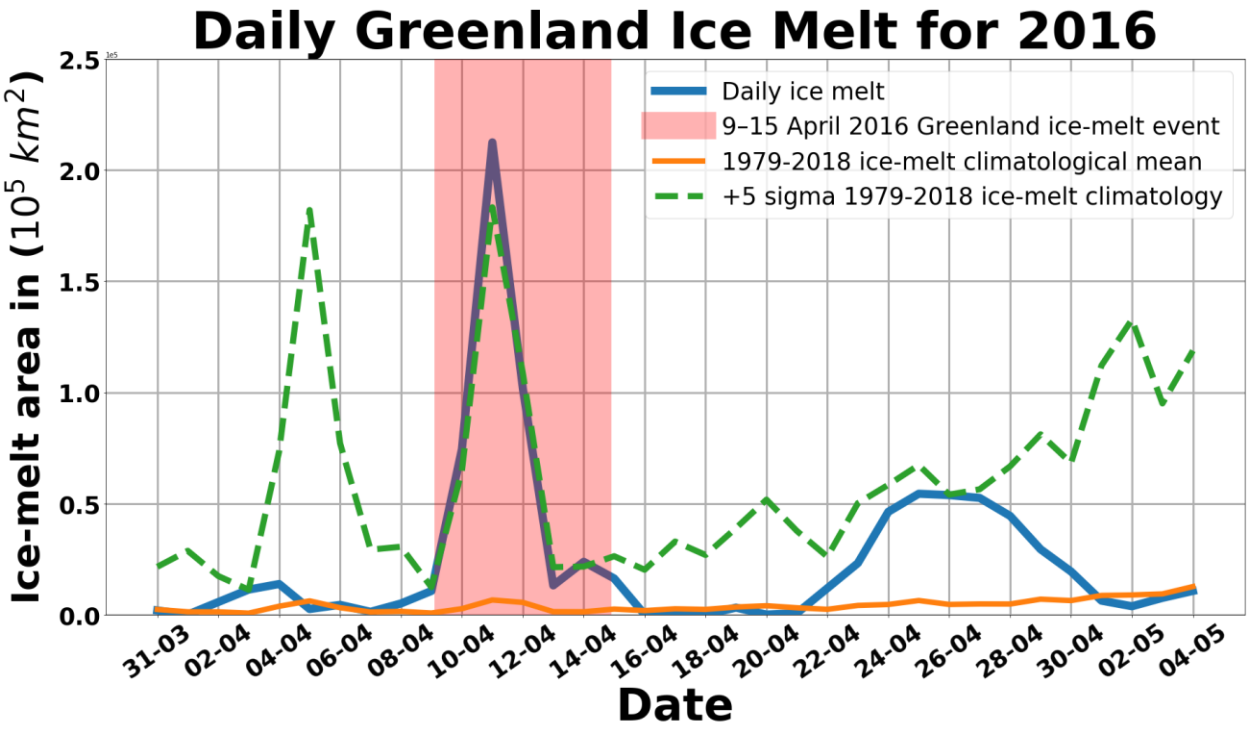

Fig. 45. As in Fig. 28, except for 9–15 April 2016 Greenland ice-melt event.

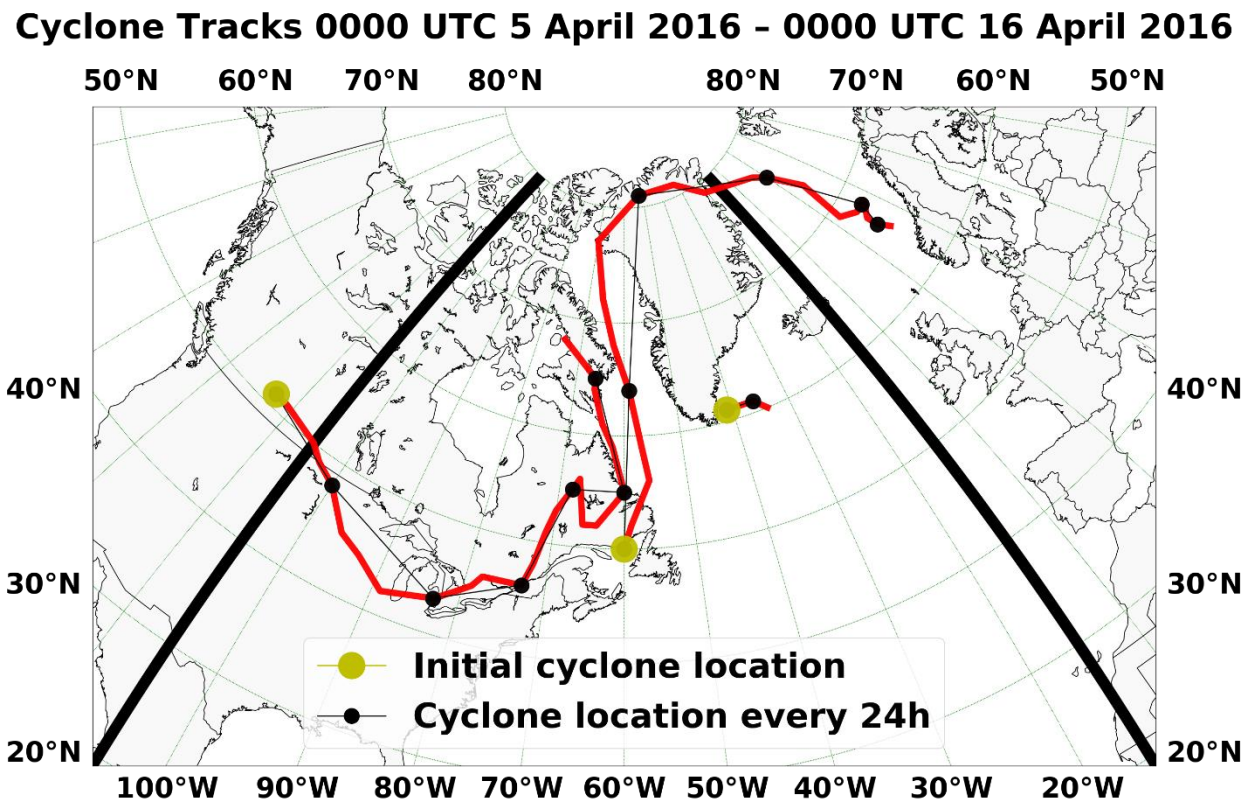

Fig. 46. Cyclone tracks (red line) for period between 0000 UTC 5 April 2016 and 0000 UTC 16 April 2016, initial cyclone location (yellow dot), and cyclone location every 24 h (black dot).

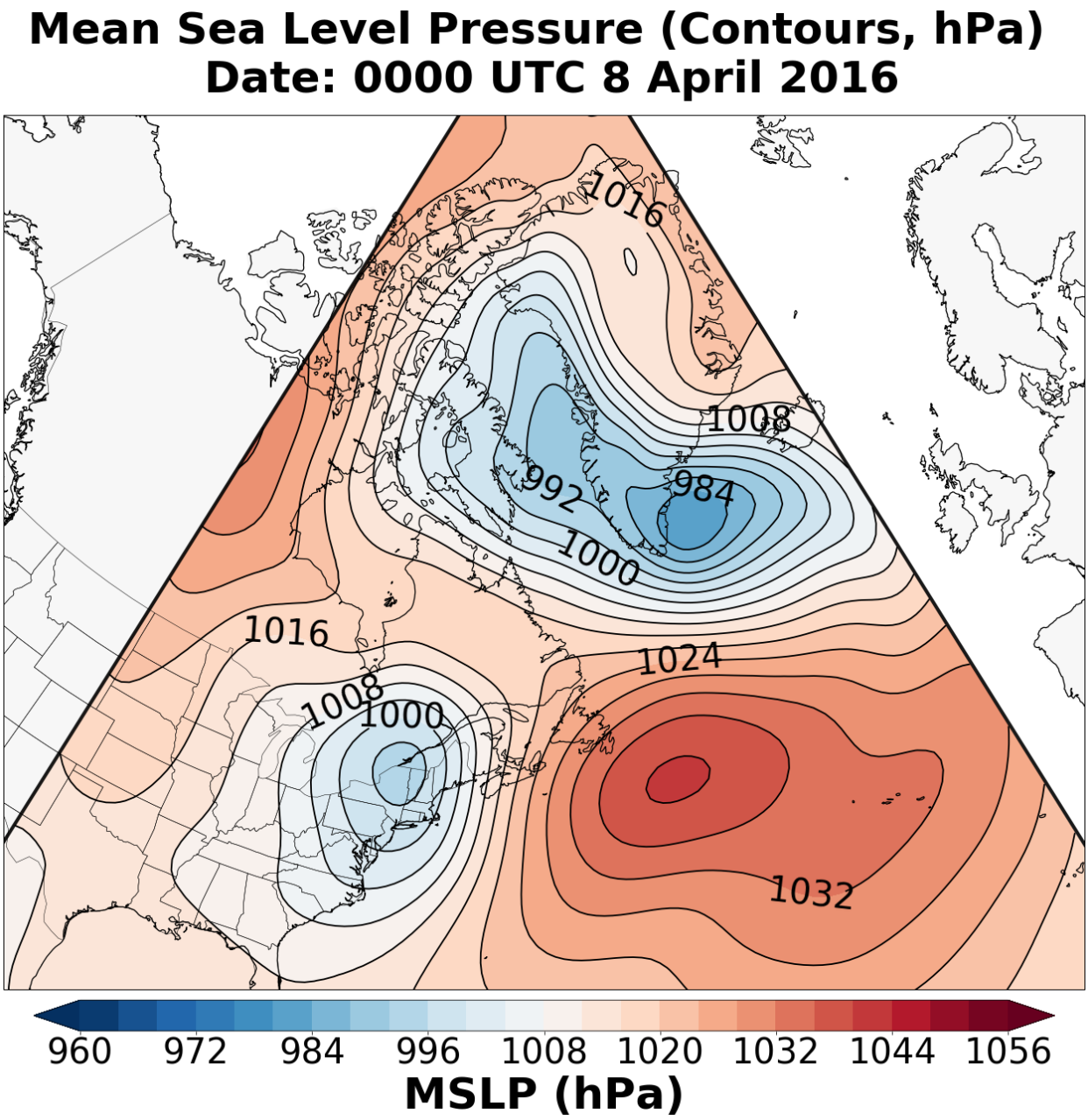

Fig. 47. As in Fig. 30, except for 0000 UTC 8 April 2016.

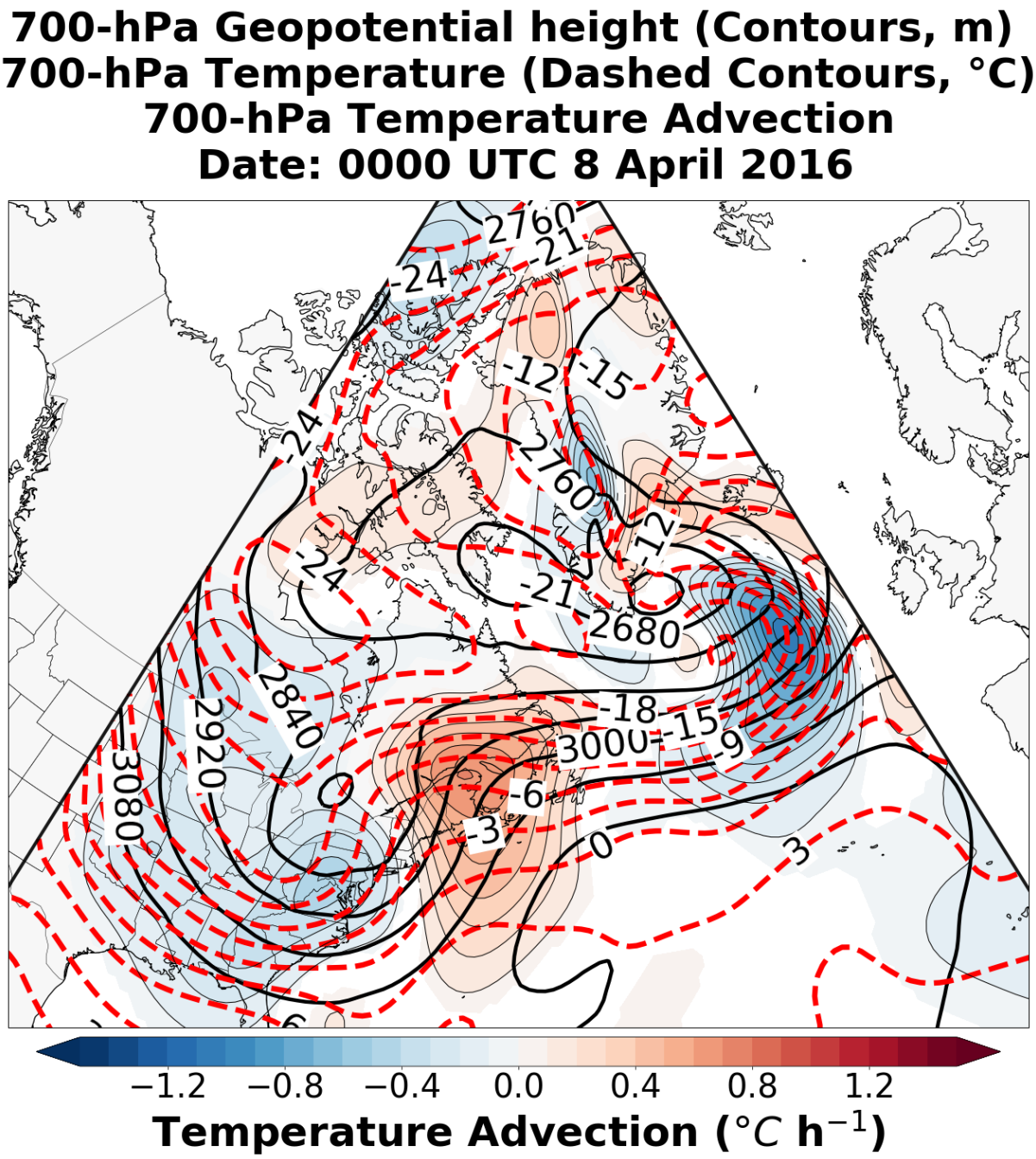

Fig. 48. As in Fig. 31, except for 0000 UTC 8 April 2016.

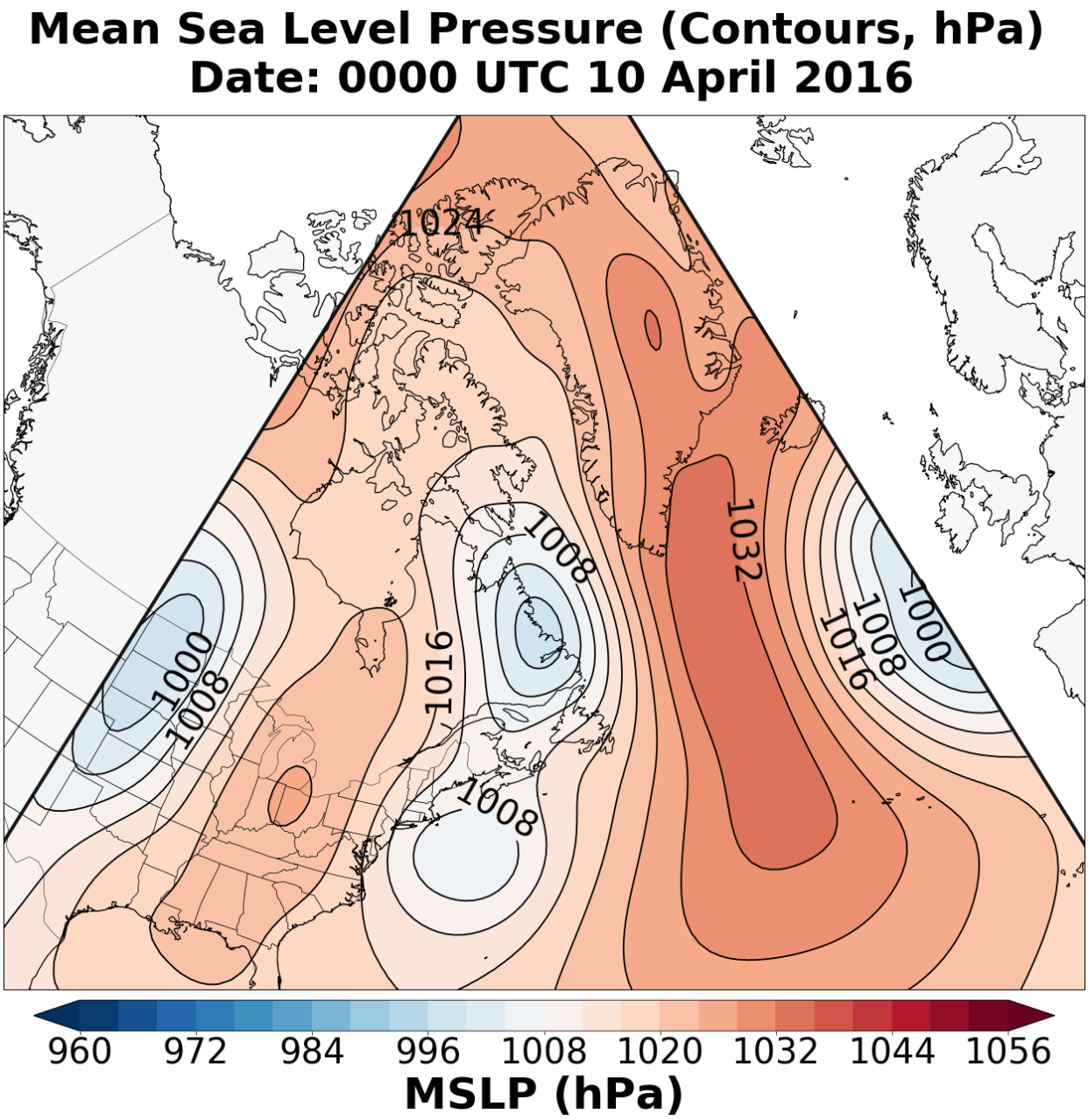

Fig. 49. As in Fig. 30, except for 0000 UTC 10 April 2016.

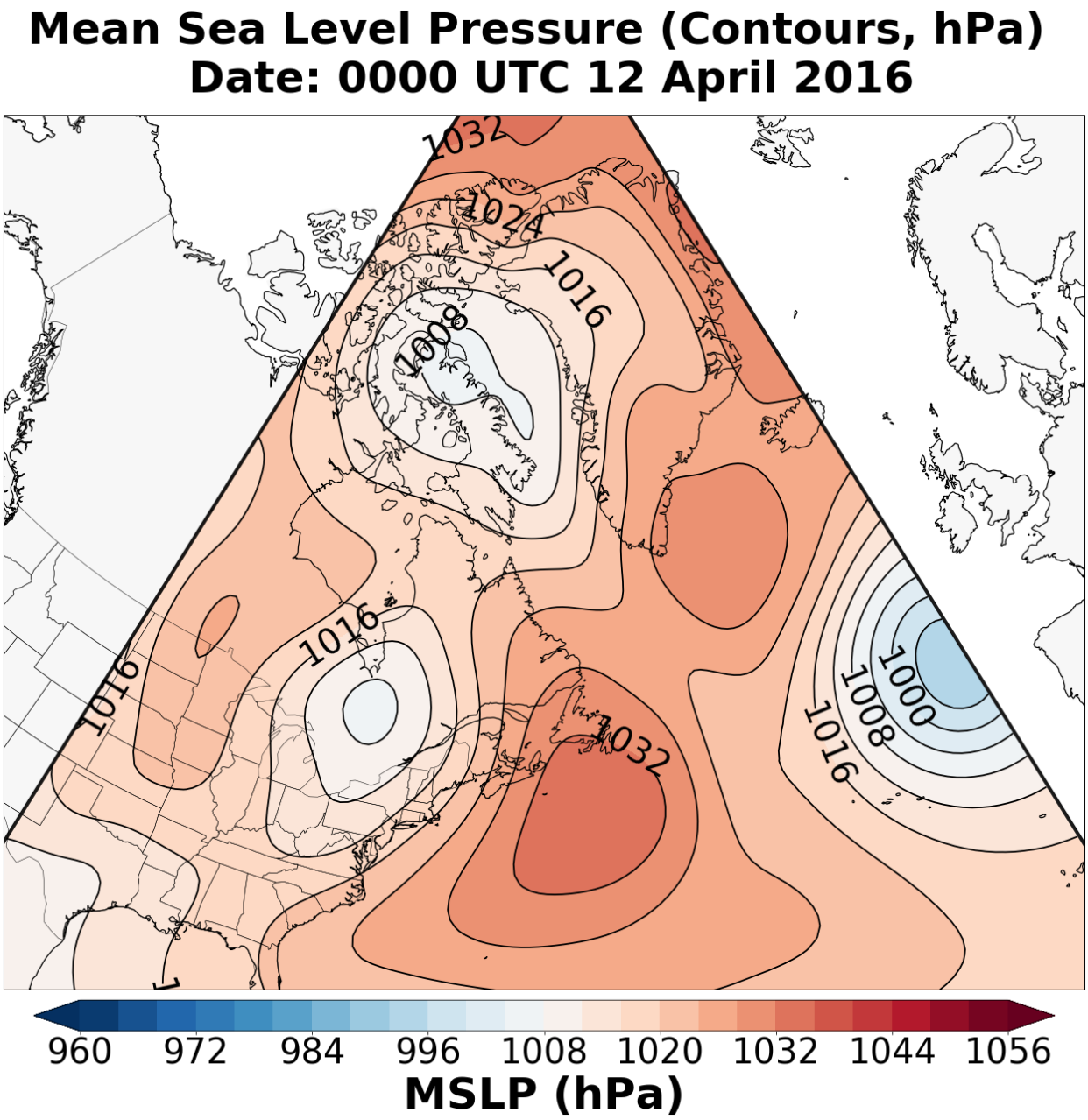

Fig. 50. As in Fig. 30, except for 0000 UTC 12 April 2016.

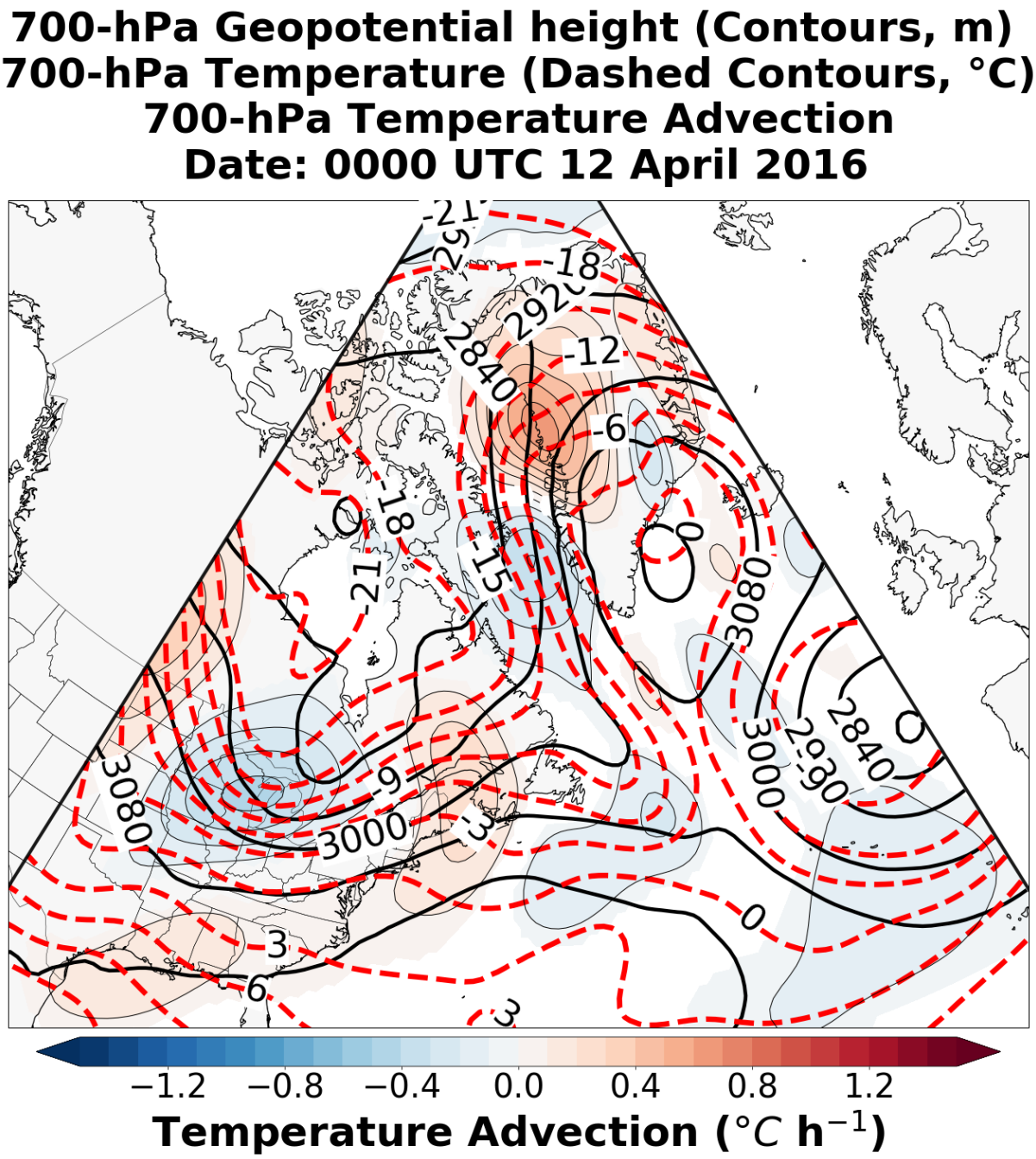

Fig. 51. As in Fig. 31, except for 0000 UTC 12 April 2016.

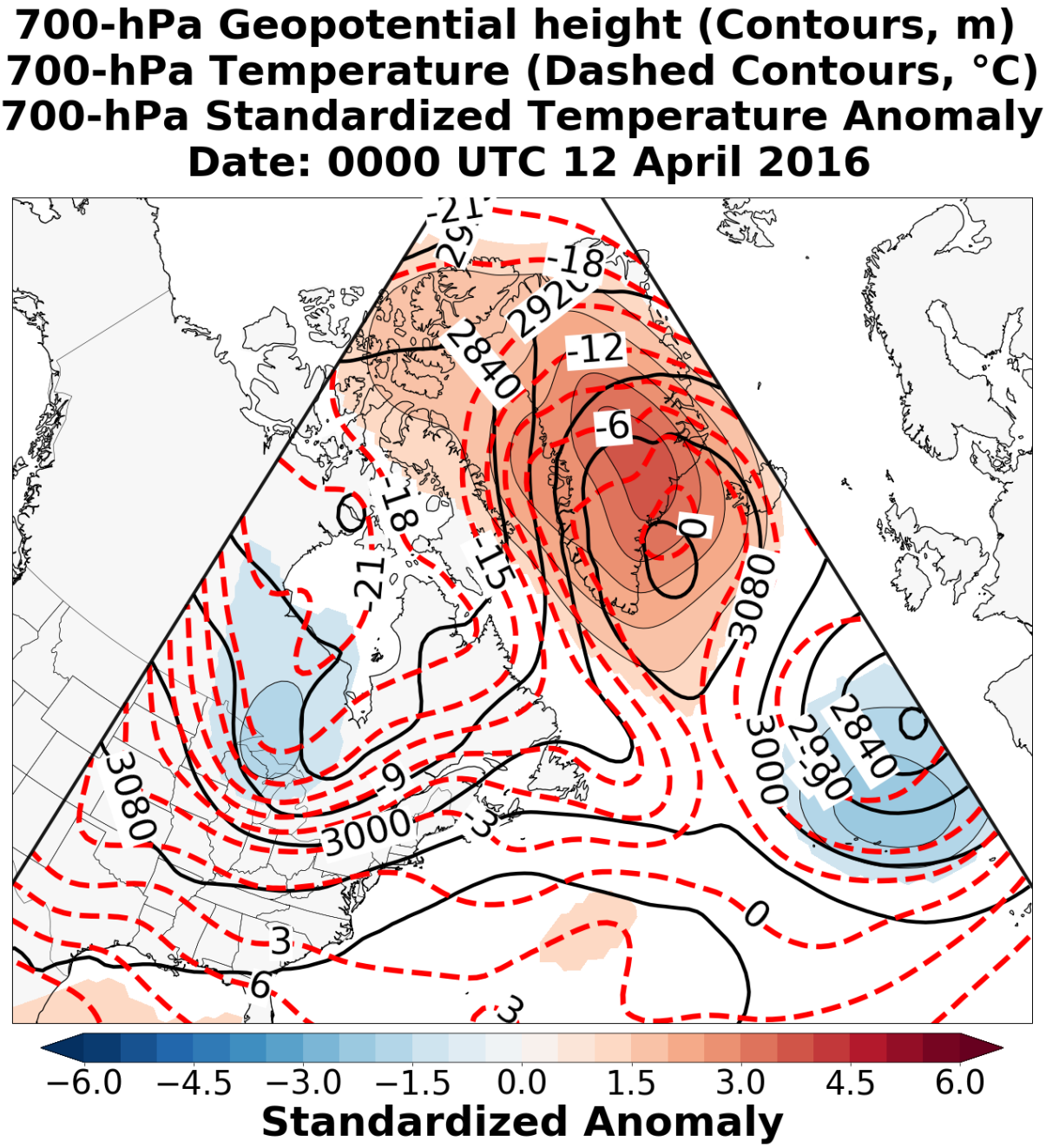

Fig. 52. As in Fig. 32, except for 0000 UTC 12 April 2016.

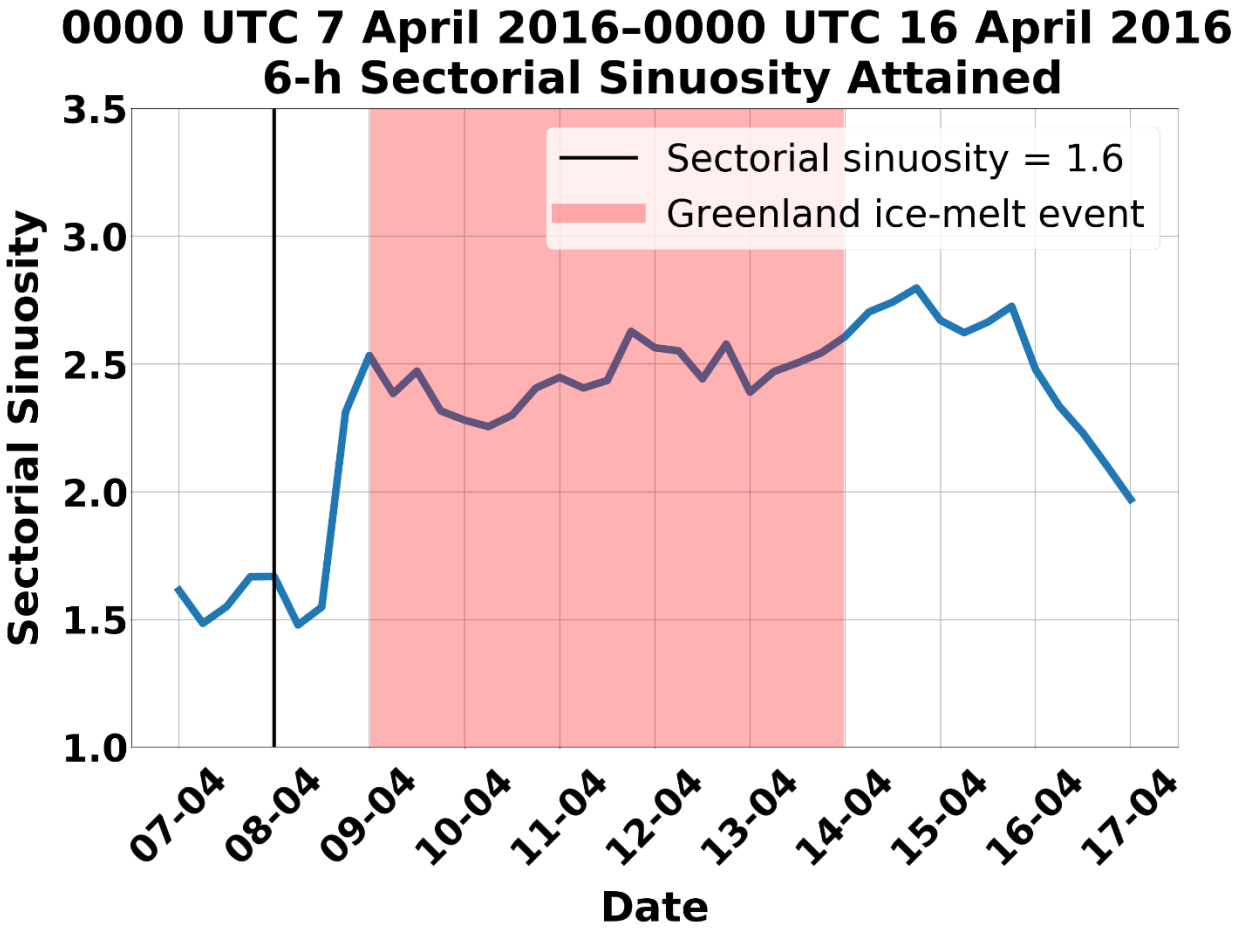

Fig. 53. 6-h sectorial sinuosity (blue curve) for period between 0000 UTC 7 April 2016 and 0000 UTC 17 April 2016, sectorial sinuosity at 0000 UTC 8 April 2016 (vertical black line), and 9–15 April 2016 Greenland ice-melt event (light red shading).

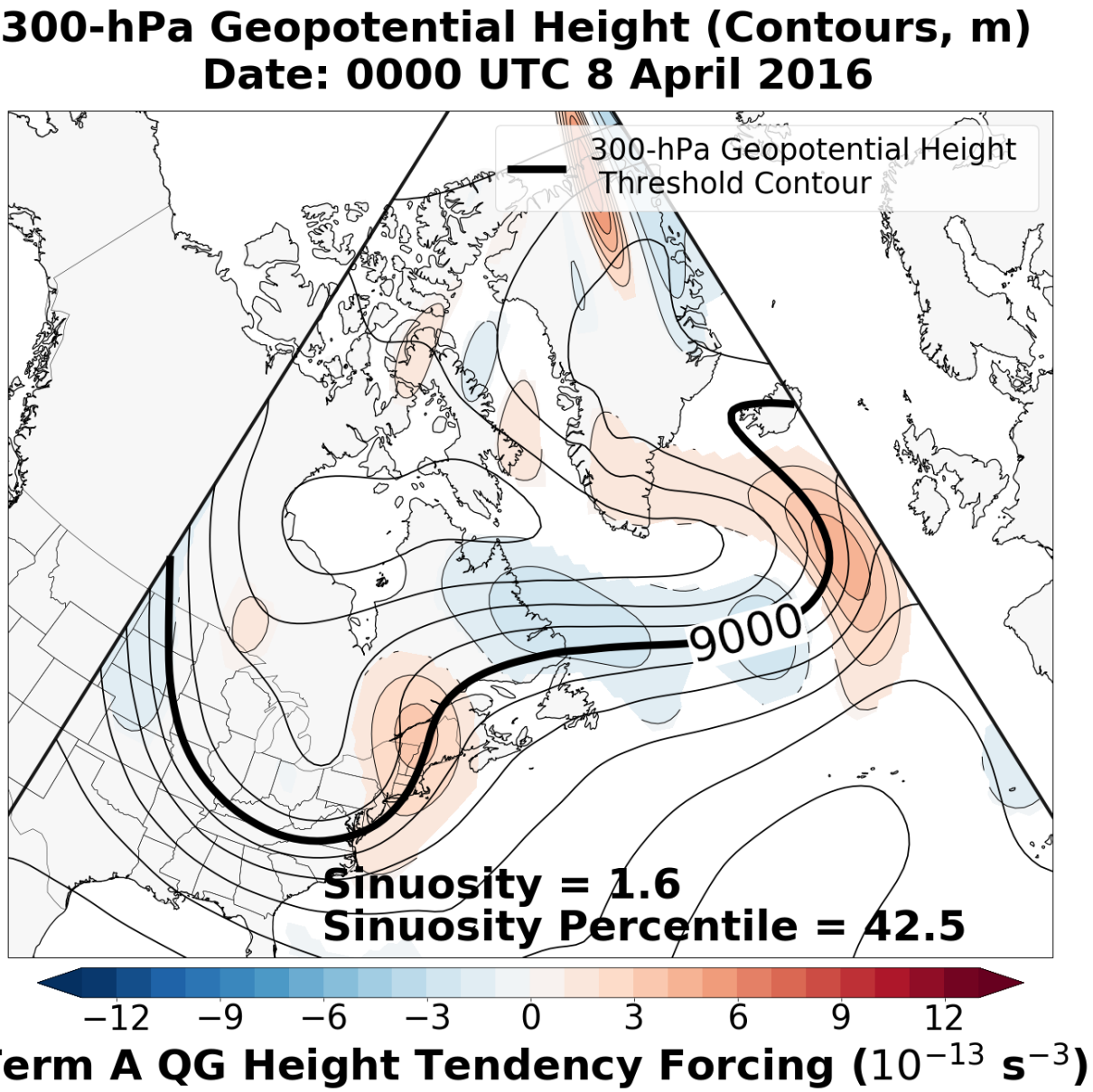

Fig. 54. As in Fig. 34, except for 0000 UTC 8 April 2016.

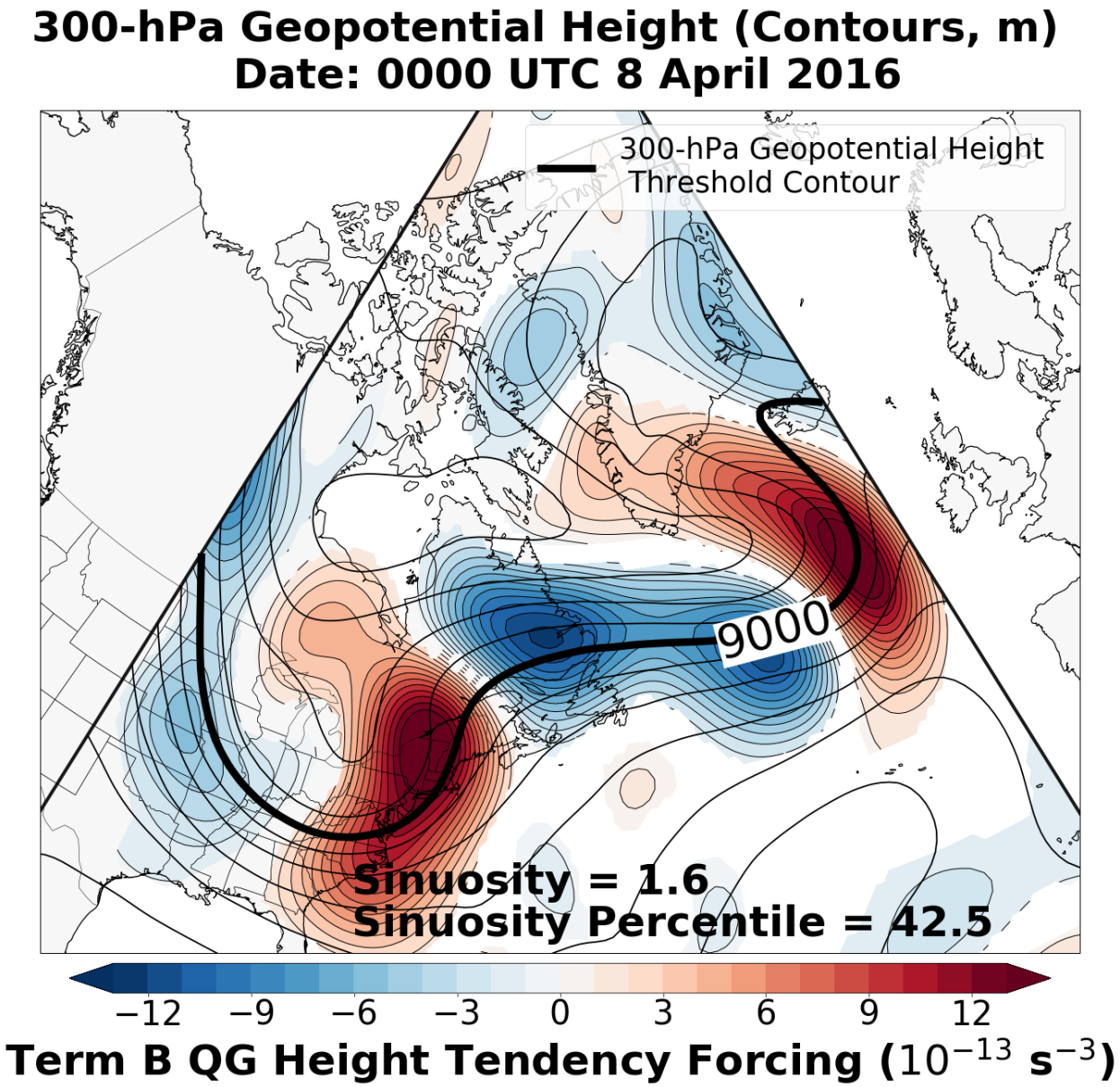

Fig. 55. As in Fig. 35, except for 0000 UTC 8 April 2016.

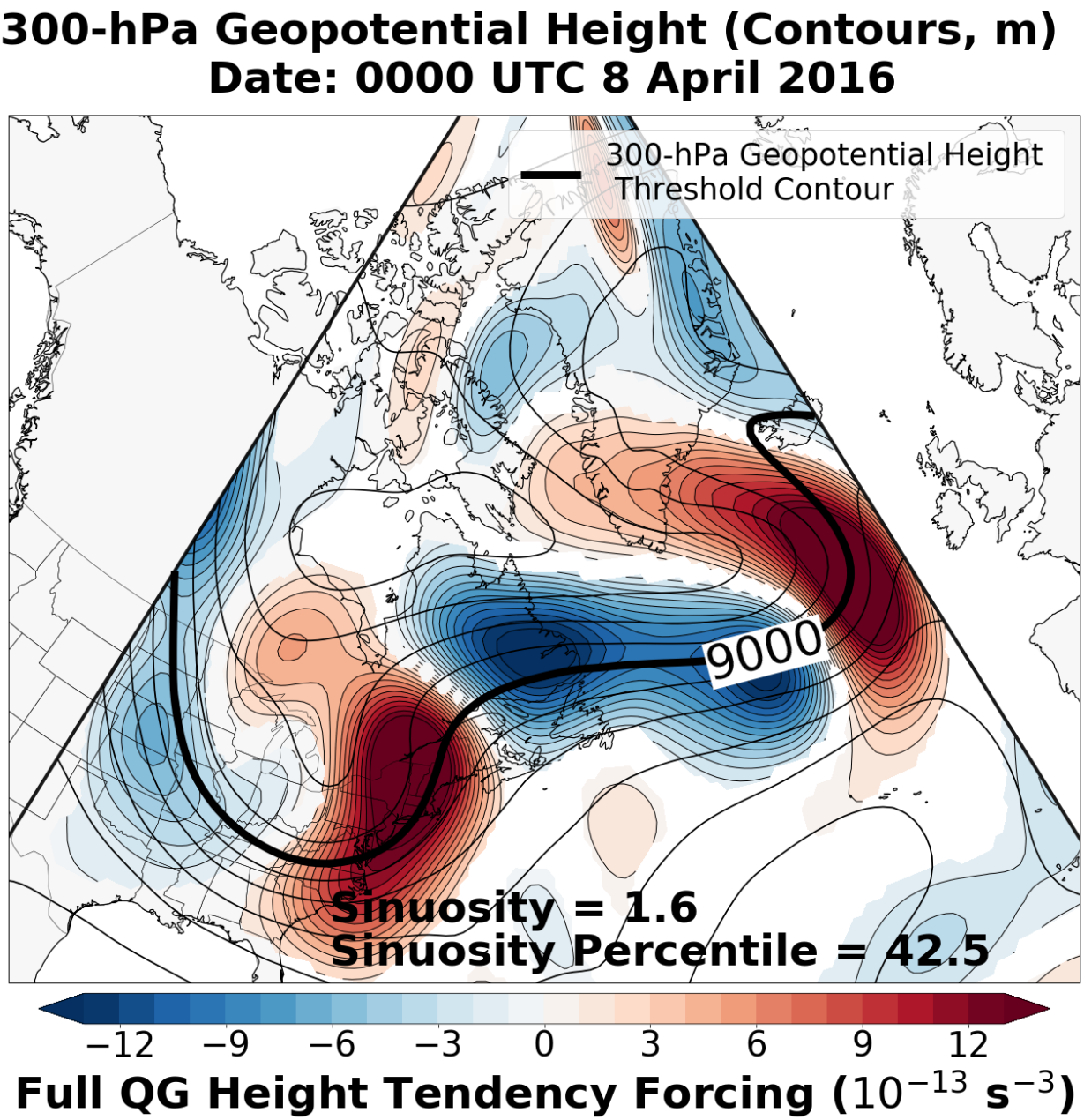

Fig. 56. As in Fig. 36, except for 0000 UTC 8 April 2016.

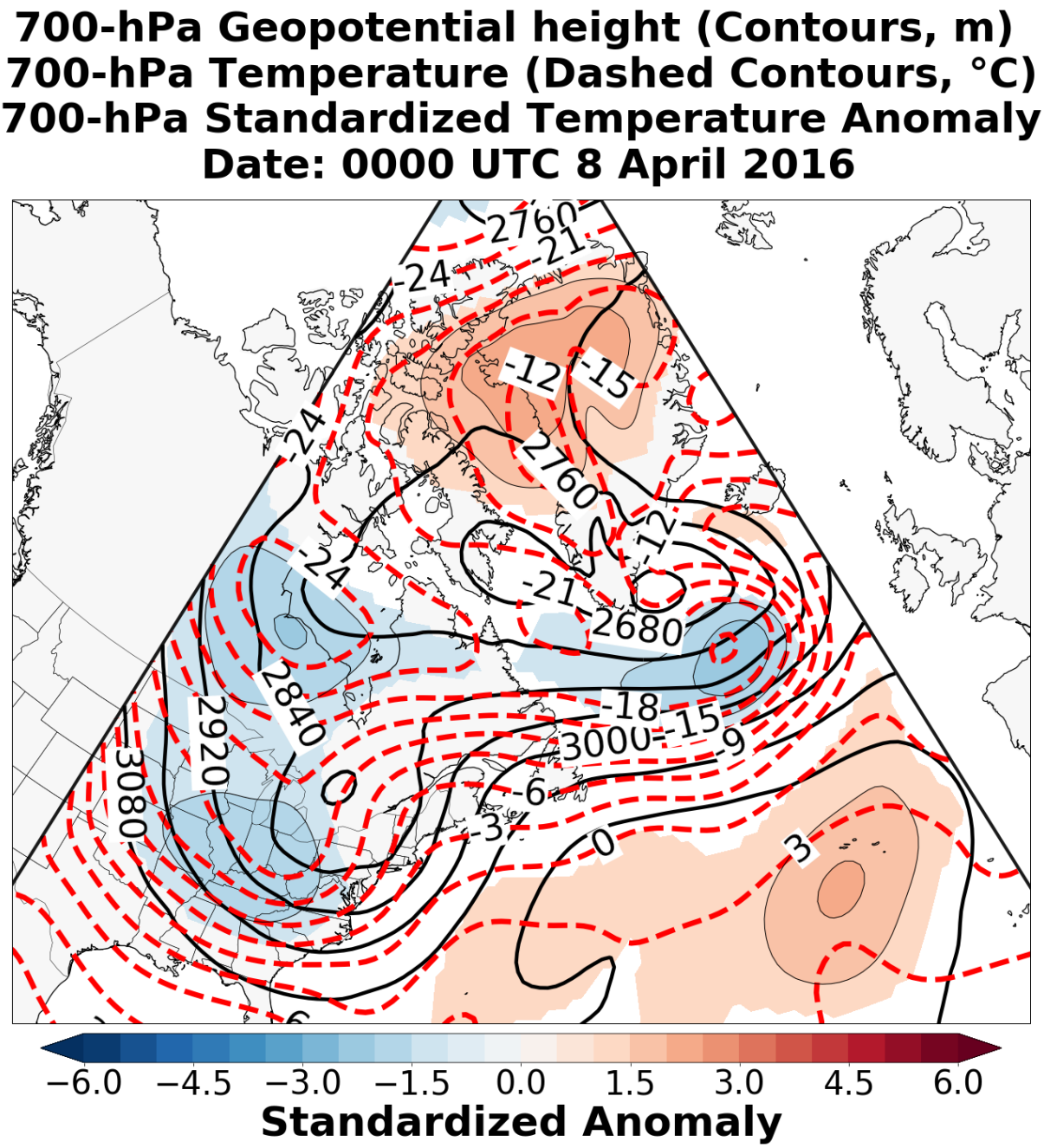

Fig. 57. As in Fig. 32, except for 0000 UTC 8 April 2016.

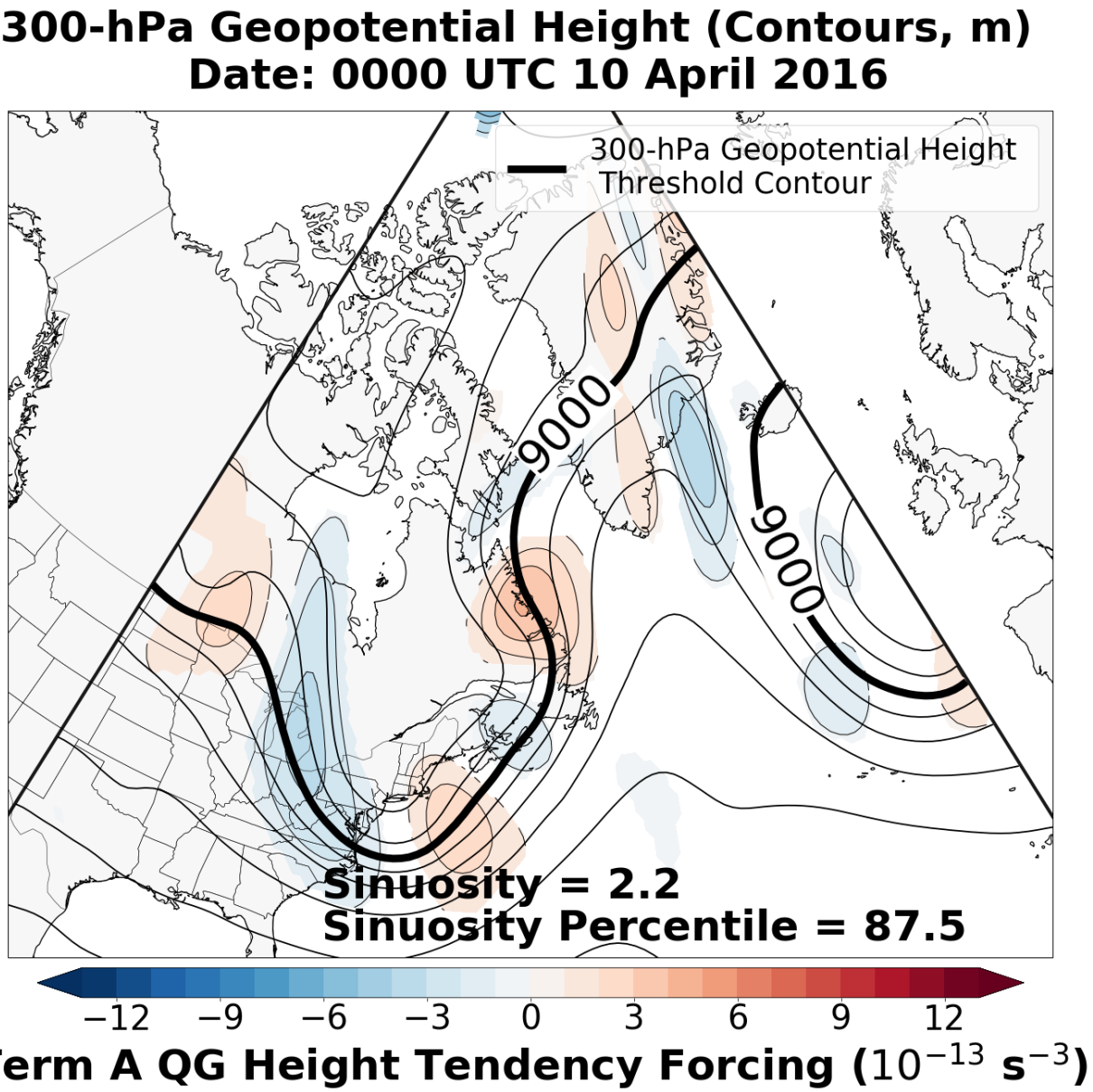

Fig. 58. As in Fig. 34, except for 0000 UTC 10 April 2016.

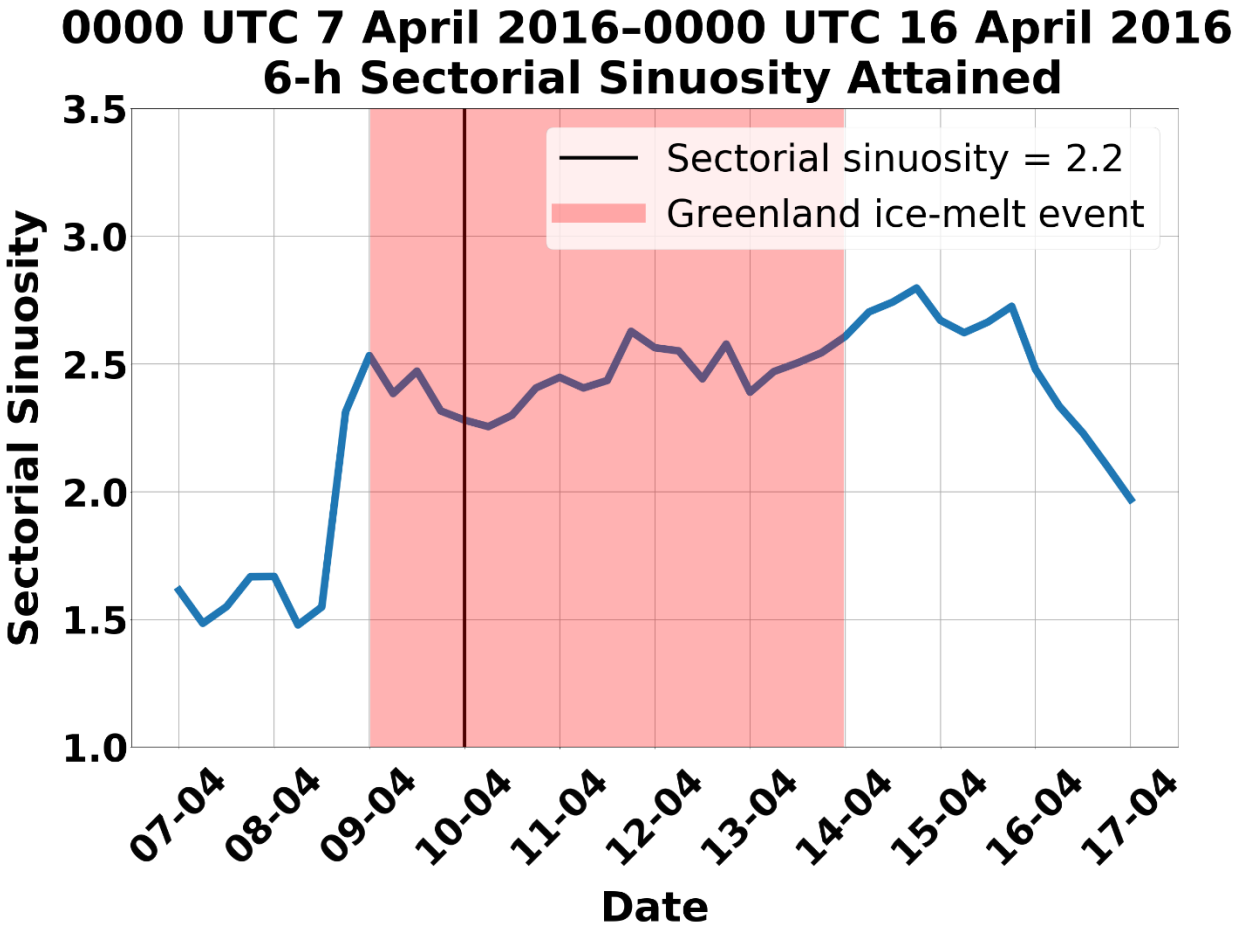

Fig. 59. As in Fig. 53, except for 0000 UTC 10 April 2016.

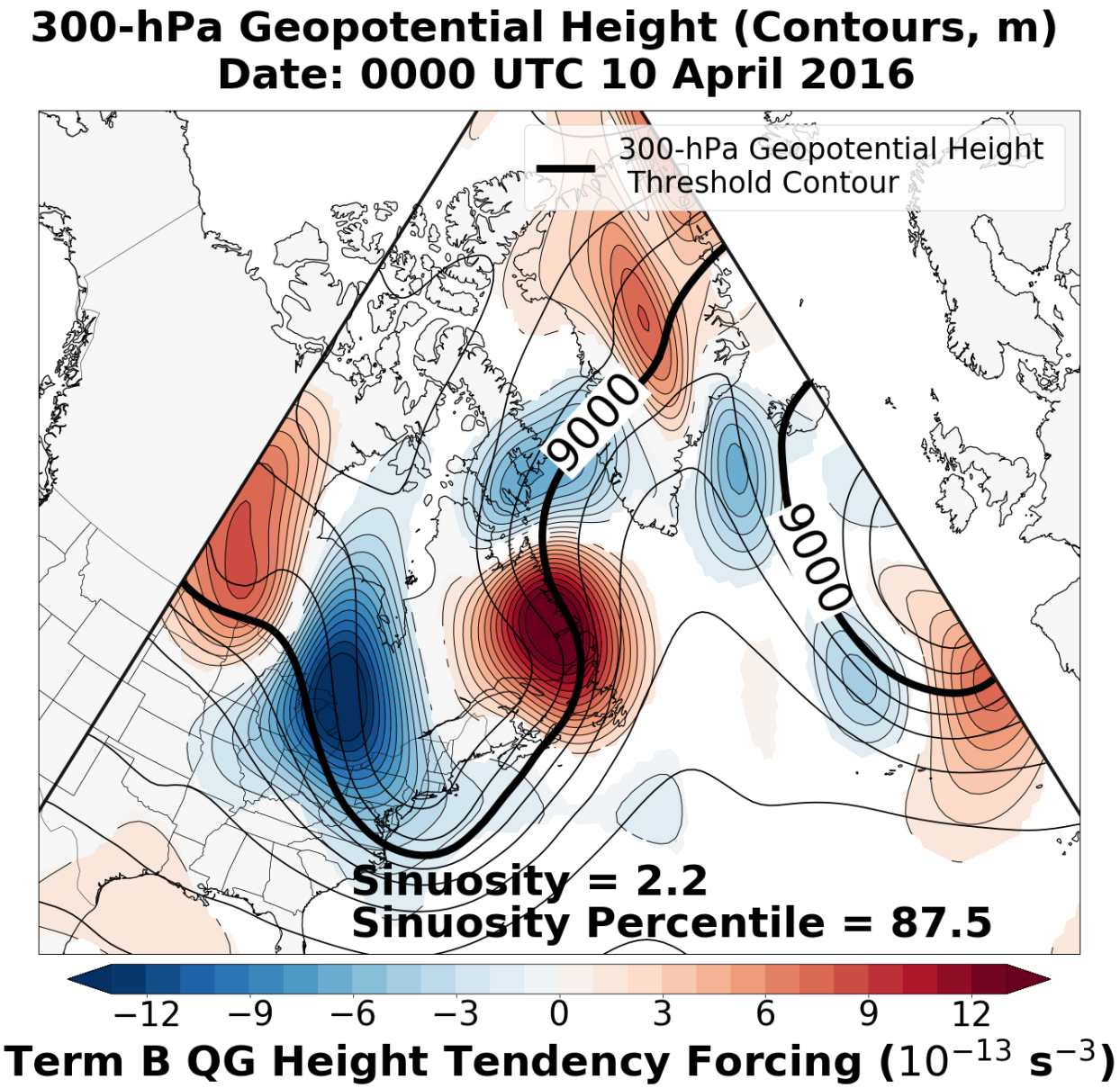

Fig. 60. As in Fig. 35, except for 0000 UTC 10 April 2016.

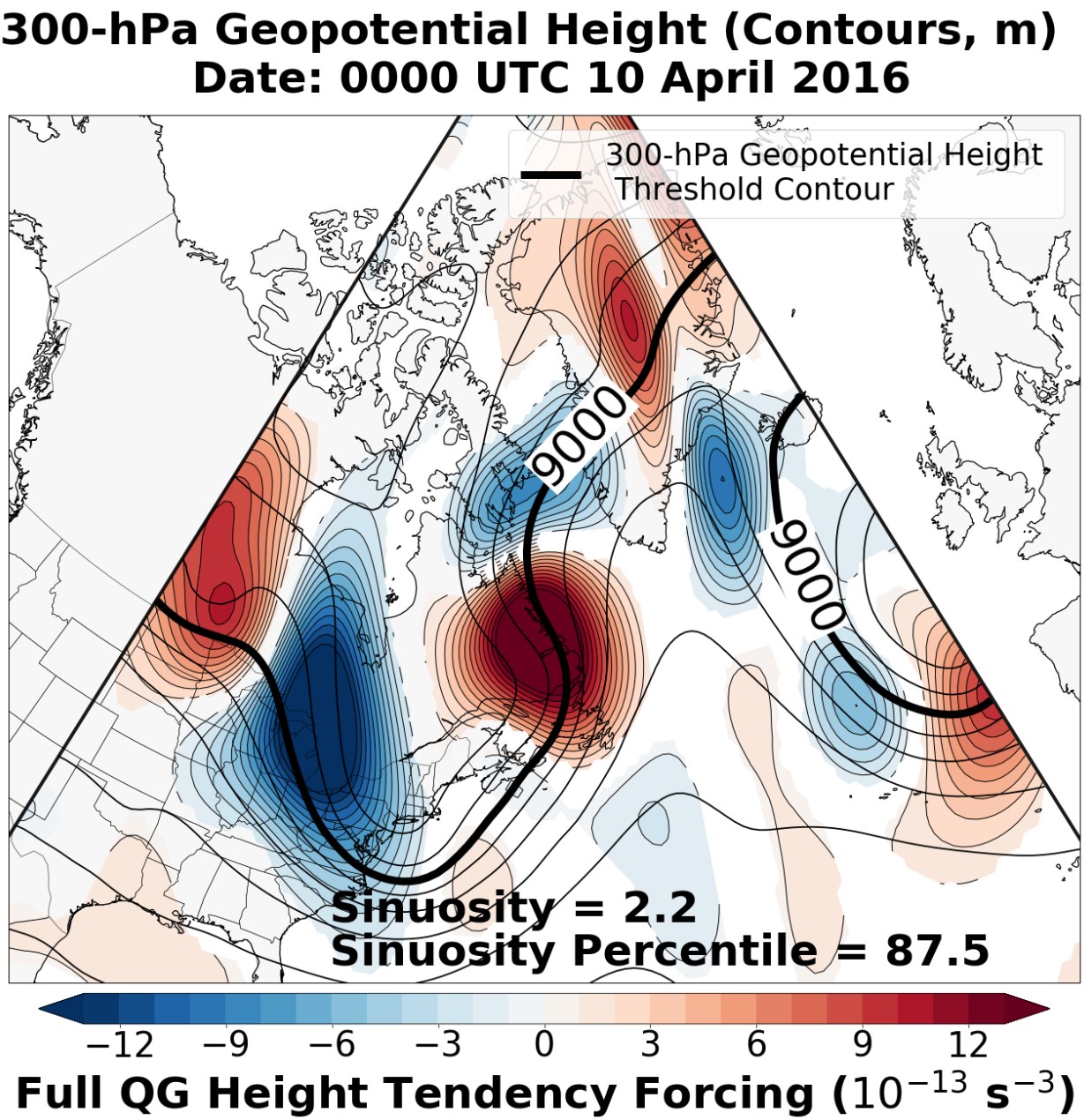

Fig. 61. As in Fig. 36, except for 0000 UTC 10 April 2016.

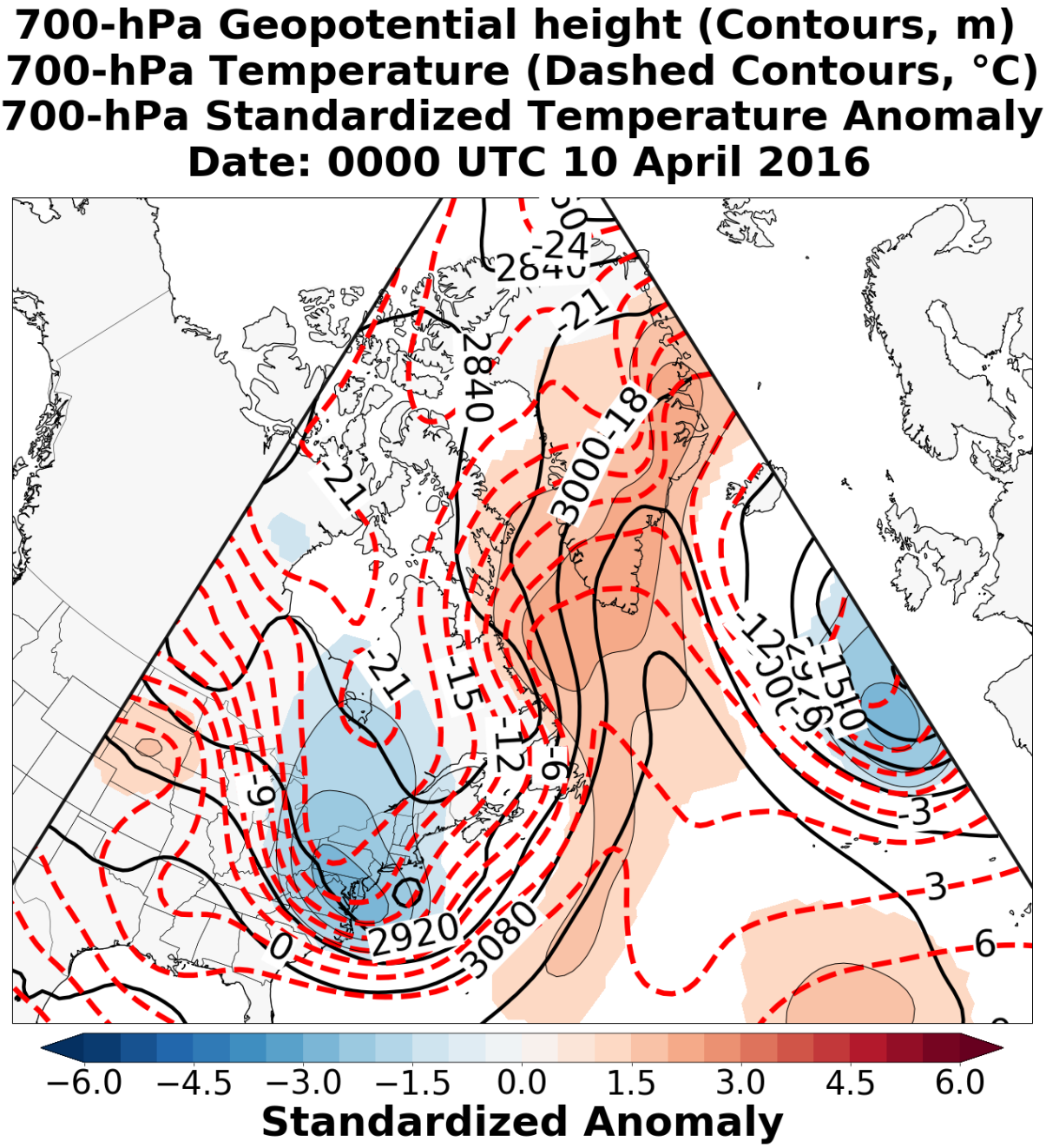

Fig. 62. As in Fig. 32, except for 0000 UTC 10 April 2016.

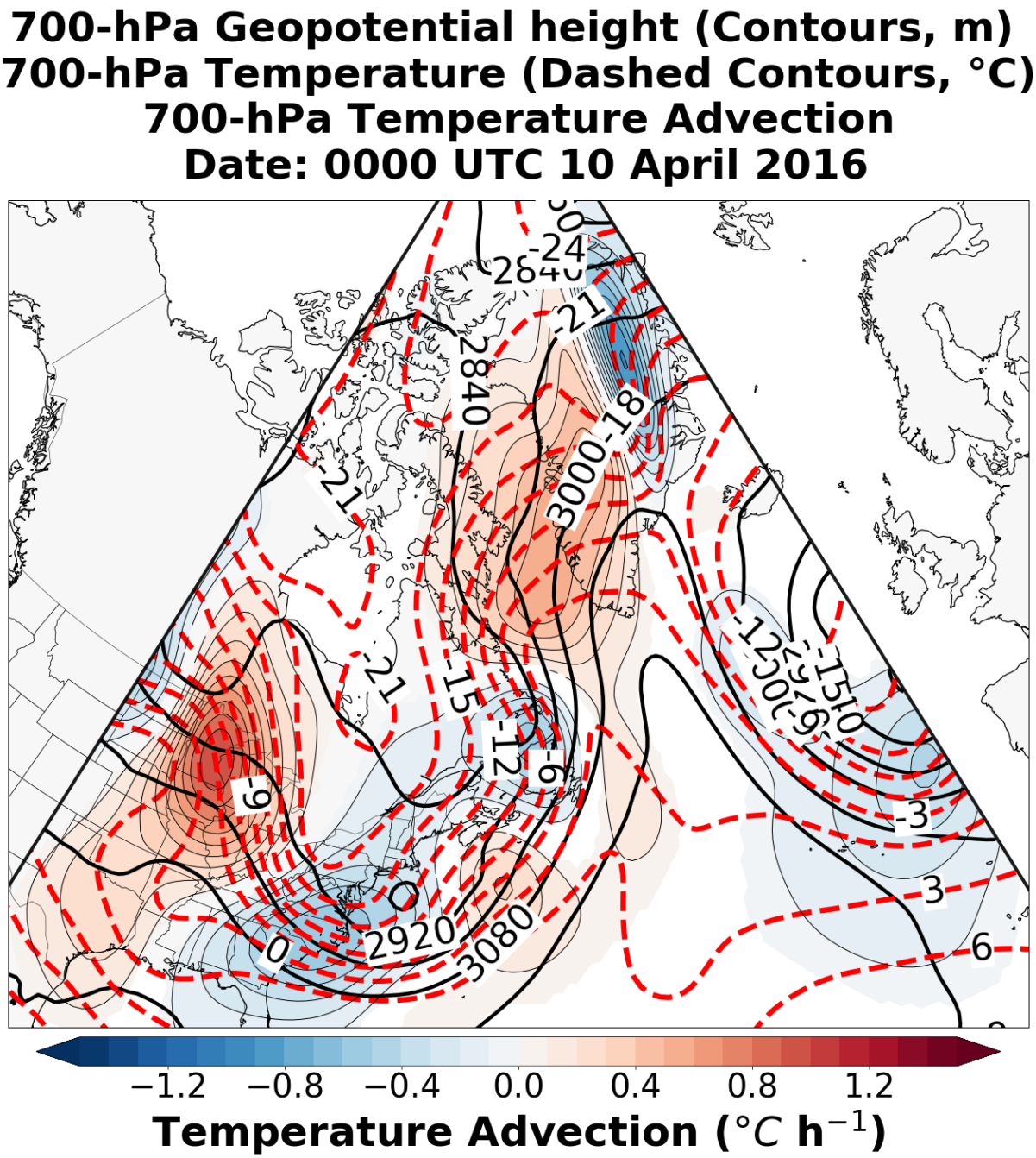

Fig. 63. As in Fig. 31, except for 0000 UTC 10 April 2016.

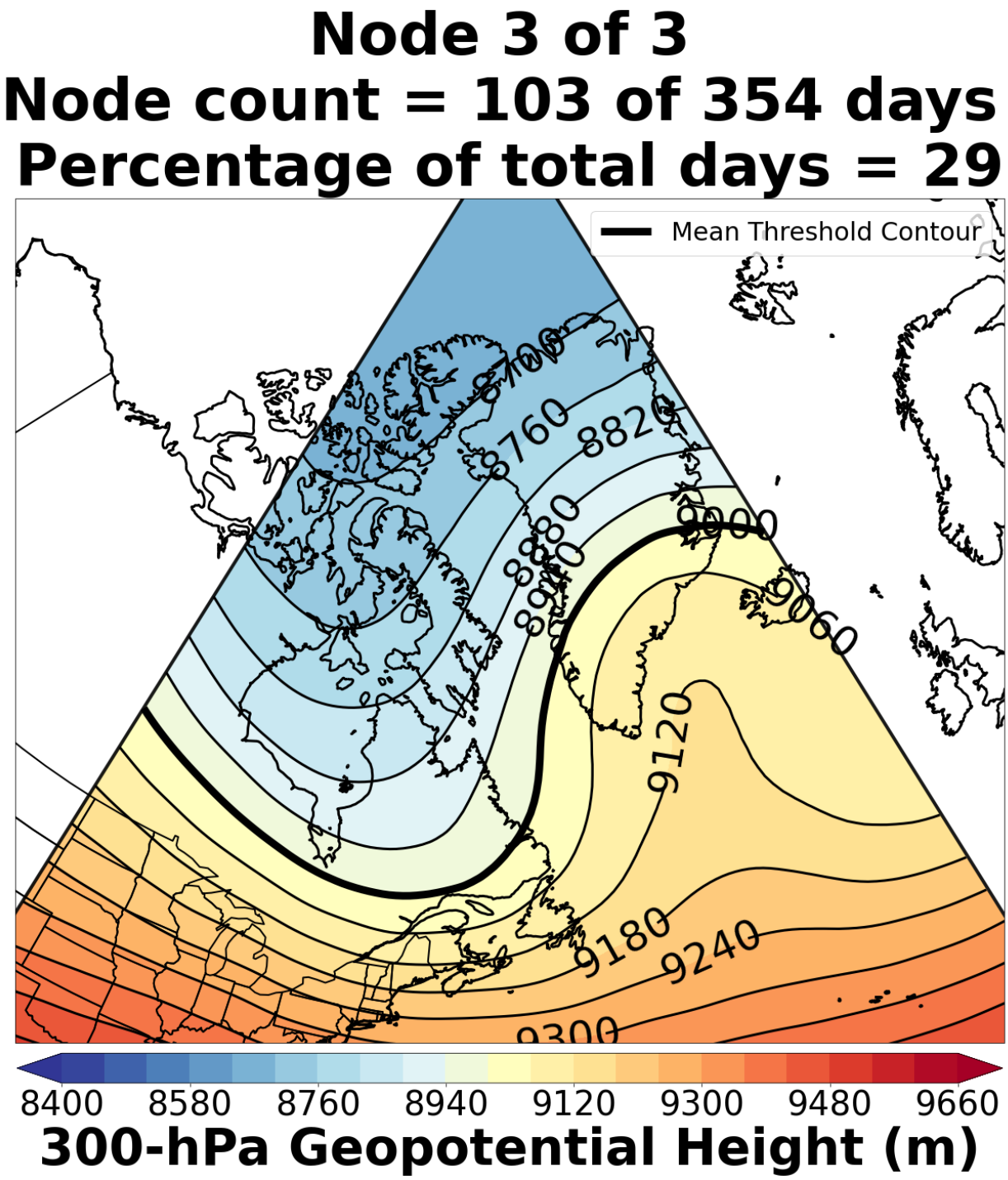

Fig. 64. As in Fig. 44, except for sinuosity group 2.

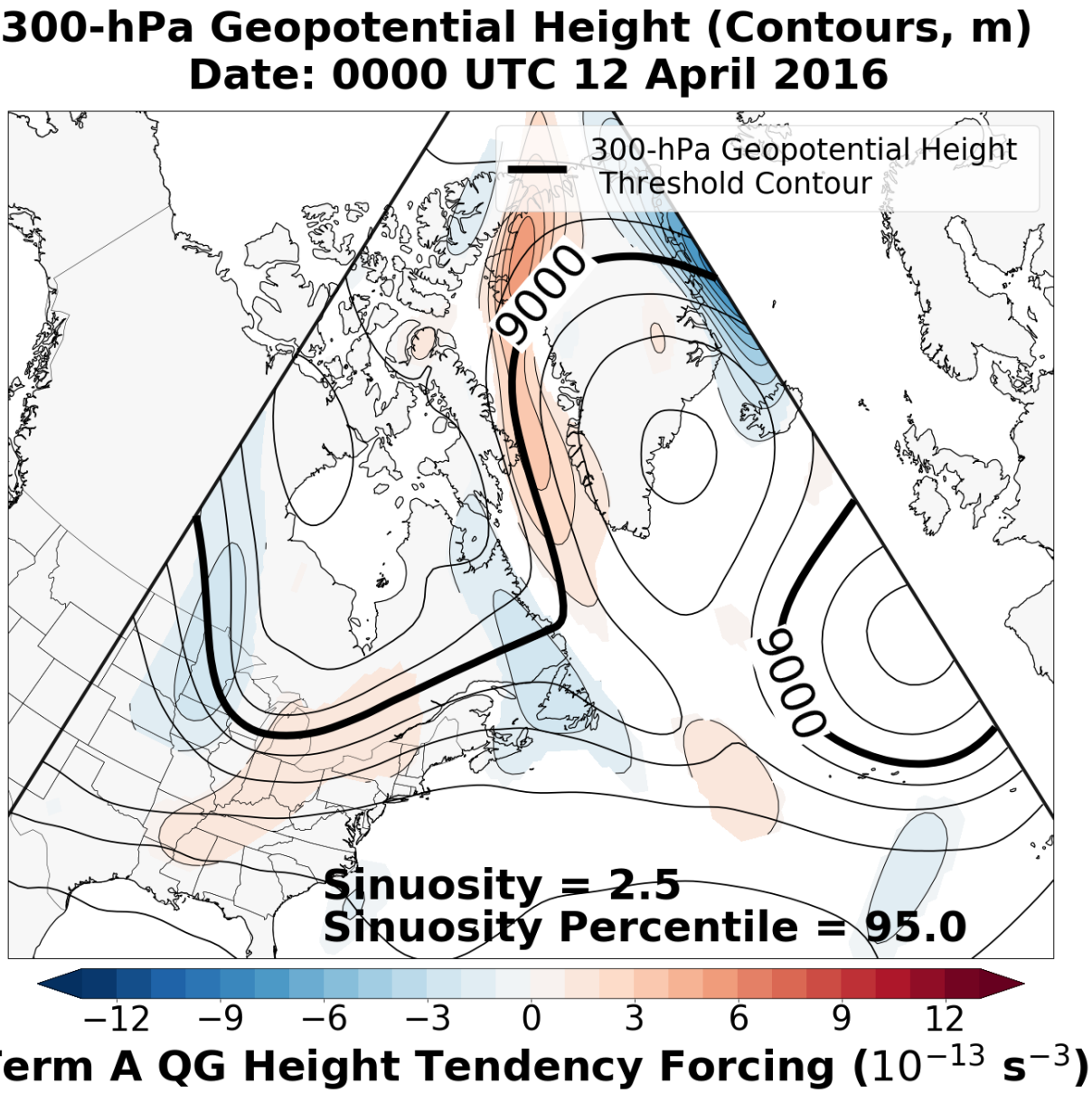

Fig. 65. As in Fig. 34, except for 0000 UTC 12 April 2016.

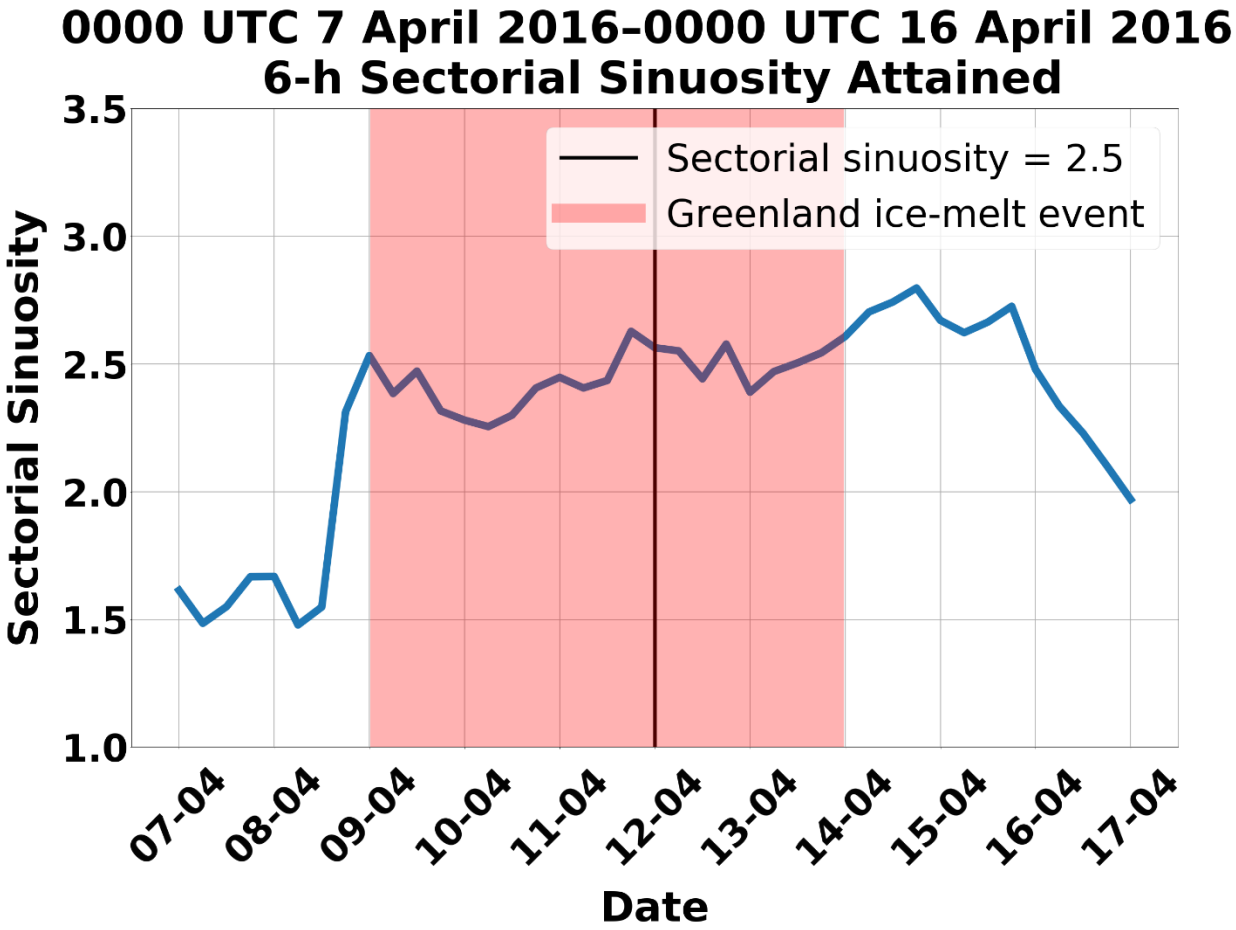

Fig. 66. As in Fig. 53, except 0000 UTC 12 April 2016.

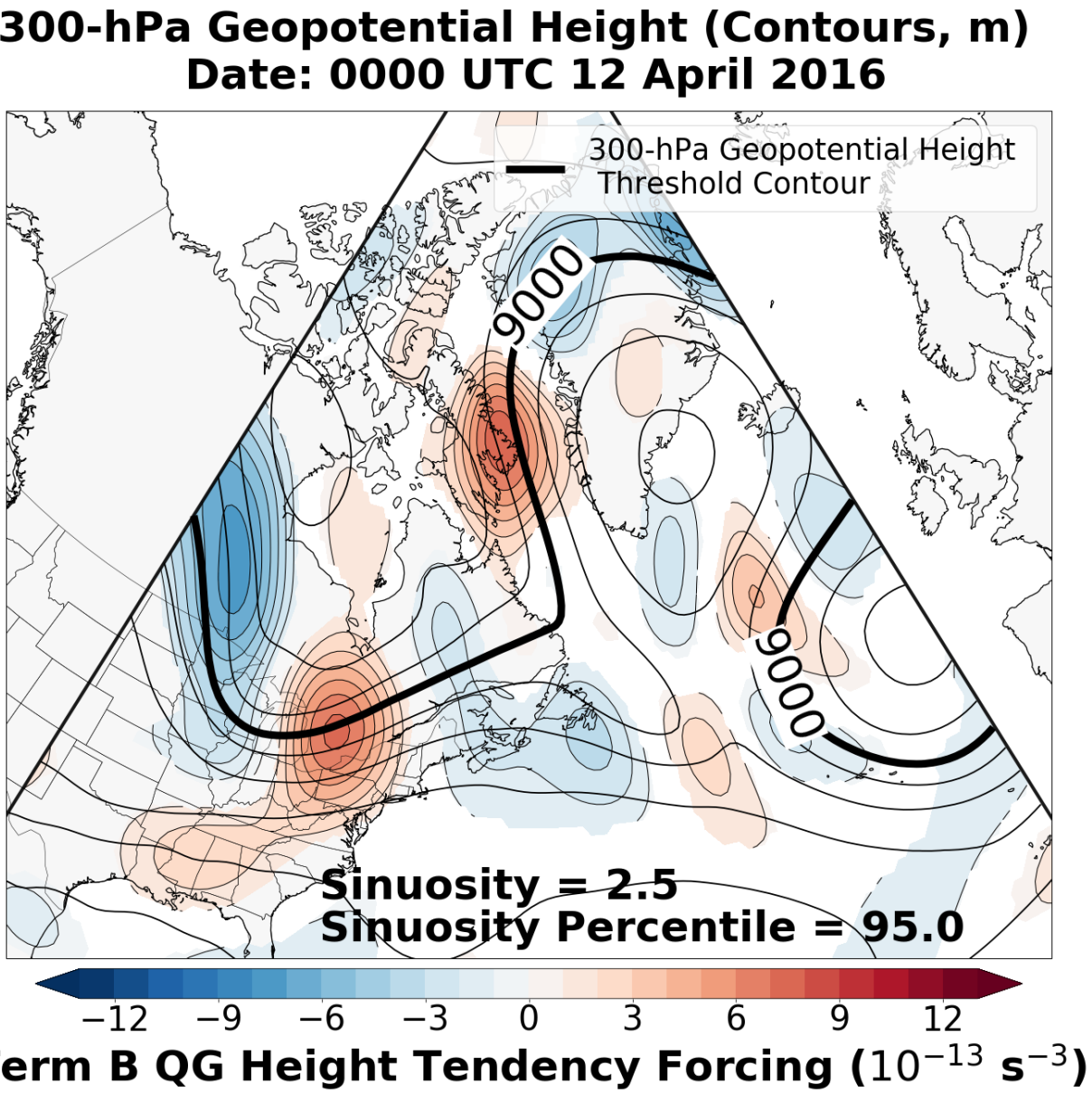

Fig. 67. As in Fig. 35, except for 0000 UTC 12 April 2016.

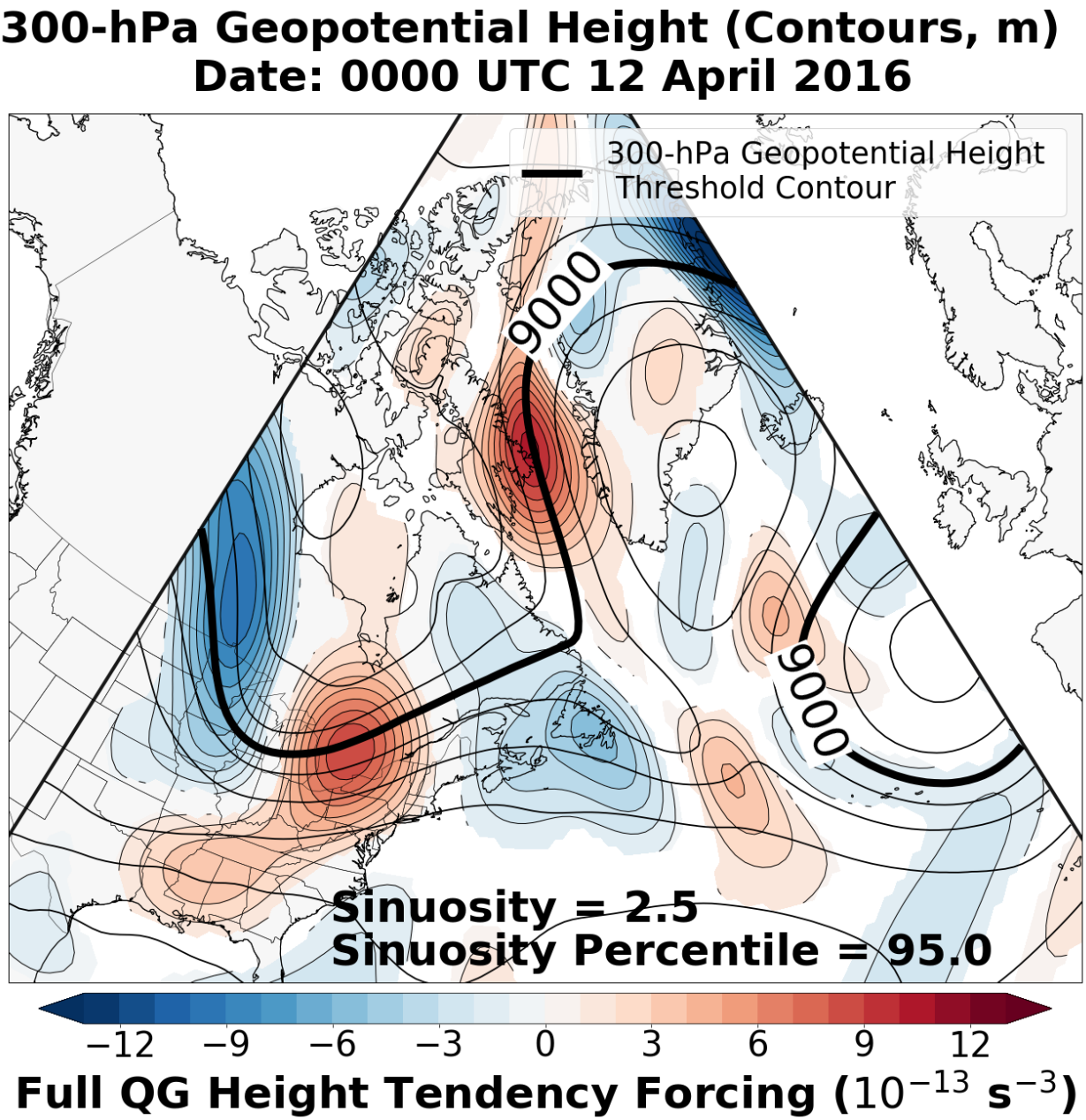

Fig. 68. As in Fig. 36, except for 0000 UTC 12 April 2016.

5 Summary

5.1 Summary

The goals of this research were to: 1) identify favorable longitudinal corridors characterized by a high frequency of ACs tracking into the Arctic from middle latitudes; 2) quantify disruptions

within the identified longitudinal sectors of the tropospheric polar vortex by warm, moist air intrusions from lower latitudes using sectorial sinuosity, a metric that describes the waviness of the flow within a longitudinal sector; 3) classify synoptic flow patterns conducive to anomalous Greenland ice-melt events into groups of flow amplitude quantified in terms of sectorial sinuosity; 4) identify, for each group of flow amplification, characteristic 300-hPa synoptic flow patterns conducive to anomalous Greenland ice-melt events using SOMs; 5) diagnose 700-hPa thermal and precipitable water characteristics over Greenland associated with anomalous Greenland ice-melt events; and 6) diagnose the disruptions by warm, moist air intrusions from lower latitudes of the tropospheric polar vortex during anomalous Greenland ice-melt events by computing the forcing terms in the QG geopotential height tendency equation. Although previous studies have adopted SOMs to investigate synoptic patterns conducive to Greenland ice sheet surface melt during summer (e.g., Mioduszewski et al. 2016), especially from a lower-tropospheric perspective, in this thesis we focus on upper-tropospheric circulation patterns and use the sectorial sinuosity metric to classify Greenland ice-melt events into groups segregated by flow amplitude.

A climatology of ACs was constructed for the 1979–2018 period using the cyclone climatology constructed by Sprenger et al. (2017) to identify favorable longitudinal corridors characterized by a high frequency of ACs tracking into the Arctic from middle latitudes. From the AC climatology, we identified four corridors of high AC track frequency, on which we centered 90° longitudinal sectors: Pacific, West of Greenland, Atlantic, and Asian. A sectorial sinuosity climatology was constructed for the 1979–2018 period using ERA-Interim reanalyses to quantify disruptions of the tropospheric polar vortex according to sector for the equatorward boundary of the tropospheric polar vortex defined by a threshold geopotential height contour on the 300-hPa surface. In this thesis, the focus was on the West of Greenland sector, where a climatology of Greenland ice-melt

events that have 3 consecutive days or more of ice melt greater than or equal to +1 standard deviation was constructed. SOMs were adopted to identify characteristic 300-hPa synoptic flow patterns conducive to anomalous Greenland ice-melt events. Two case study events, one from the 10th percentile and the other from the 90th percentile of standardized Greenland ice-melt anomaly, were randomly selected and compared in terms of their corresponding value of the thermal metric, i.e., the area-averaged value of standardized 700-hPa temperature anomaly over a defined domain over Greenland. These events were investigated to gain further understanding of the similarities and differences between events at the 10th and 90th percentiles of standardized Greenland ice-melt anomaly. These two events were also analyzed according to the evolution of the amplitude of the flow quantified in terms of sectorial sinuosity and interpreted in terms of the QG geopotential height tendency forcing.

5.1.1 Climatologies

This thesis focused on the West of Greenland sector where the sectorial sinuosity climatology, along with the Greenland ice-melt event climatology, were used to quantify the modification of the tropospheric polar vortex by localized incursions of warm, moist air from middle latitudes.

A total of 942 days with melting equal to or above +1 standard deviation of Greenland ice melt constitute the upper 40th percentile of the 2351 identified days from the climatology of Greenland ice-melt events. Probability density functions of sectorial sinuosity associated with ±1 sigma Greenland ice-melt days show that it is more likely for +1 sigma ice-melt days to occur in high sectorial sinuosity regimes compared to −1 sigma ice-melt days.

The 690 days that constitute 129 Greenland ice-melt events were identified and classified into three groups according to the magnitude of the sectorial sinuosity of the threshold 300-hPa geopotential height contour: 155 days with sectorial sinuosity between 1 and 2 (group 1), 354 days with sectorial sinuosity between 2 and 3 (group 2), and 181 days with sectorial sinuosity greater than 3 (group 3). SOMs identified a total of 9 nodes, with each sectorial sinuosity group divided into three nodes of characteristic 300-hPa geopotential height patterns constructed from ERA-Interim reanalysis data associated with anomalous Greenland ice-melt events. Each node consisted of similar 300-hPa geopotential height patterns identified by the SOMs and is described below:

I. Node 1 is associated with a low-amplitude negatively tilted trough–ridge pattern.

II. Node 2 is associated with a low-amplitude positively tilted trough–ridge pattern.

III. Node 3 is associated with a low-amplitude neutrally tilted trough–ridge pattern.

IV. Nodes 4–6 are associated with medium-amplitude trough–ridge patterns.

V. Nodes 7 and 9 are associated with a high-amplitude omega block ridge pattern.

VI. Node 8 is associated with a high-amplitude Rex block ridge pattern.

A thermal metric and a precipitable water metric were calculated by taking the area-averaged values of standardized 700-hPa temperature anomaly and standardized precipitable water anomaly, respectively, for a domain over Greenland for the 942 days with melting greater than or equal to +1 standard deviation of Greenland ice melt. These respective metrics describe 700-hPa temperature and precipitable water patterns associated with each node. The best-fitting regression line relating each metric to Greenland ice melt was calculated using linear regression for each node to diagnose the relationship between the two metrics and Greenland ice melt. The days for each node were sorted by increasing order of standardized Greenland ice-melt anomaly for each day. The regression analysis shows that nodes associated with days that occur in the colder months of

the ice-melt season (April, May, September, and October) exhibit a weak dependence (i.e., low R-values) of each of the metrics on ice melt, whereas nodes associated with days that occur in the warmer months of the ice-melt season (June, July, and August) exhibit a strong dependence (i.e., high R-values) of each of the metrics on ice melt.

5.1.2 Case Studies

From section 3.2.4, events at the 10th percentile of standardized Greenland ice-melt anomaly were found to be associated with low positive mean values of the thermal metric compared to events at the 90th percentile. Two case study events were randomly selected from the 10th and 90th percentile and then compared in terms of their corresponding value of the thermal metric. The forcing terms from the QG geopotential height tendency equation [Eq. (5.6.13) in Bluestein (1992, p. 330)], denoted by Eq. (2) in section 4.1.1, were calculated at 300-hPa. These forcing terms were used to diagnose the evolution of the tropospheric polar vortex for the two selected events. In Eq. (2) of section 4.1.1, Term A refers to the advection of geostrophic absolute vorticity by the geostrophic wind (i.e., the propagation term), and Term B refers to the differential advection of temperature by the geostrophic wind (i.e., the amplification term).

The 5–7 June 2009 event, randomly selected from the 10th percentile of standardized Greenland ice-melt events, was associated with a standardized Greenland ice-melt anomaly reaching ~+1.1 sigma on 0000 UTC 5 June 2009. During this event, a surface cyclone initially located over western Canada on 0000 UTC 28 May 2009 tracked to the eastern coast of Newfoundland by 1200 UTC 5 June 2009. The surface cyclone moved slowly into Newfoundland and was located downstream of a 300-hPa trough over eastern Canada and upstream of a 300-hPa ridge over southern Greenland. The poleward-moving surface cyclone was concurrent with 300-hPa ridge amplification over

Greenland. The evolution of the amplitude of the ridge was quantified in terms of sectorial sinuosity, which increased from 2.3 on 0000 UTC 3 June 2009 to 3.7 on the day of the standardized Greenland ice-melt anomaly event, 1200 UTC 5 June 2009.

The amplitude of the 300-hPa flow pattern on 1200 UTC 5 June 2009 was characterized as high, i.e., sectorial sinuosity greater than or equal to 3. The aforementioned increase in sectorial sinuosity was associated with 300-hPa ridge amplification over southern Greenland, resulting in a flow pattern that is favorable for the transport of warm air poleward. Ridge amplification at 300 hPa was dominated by geopotential height tendency forcing from the amplification term (Term B), where negative values imply geopotential height rises. Negative values of Term B were located along the poleward side of the 300-hPa ridge located over Hudson Bay and extending over the western coast of Greenland on 0000 UTC 3 June 2009 and leading up to 1200 UTC 5 June 2009 when the flow reached maximum amplitude corresponding to a sectorial sinuosity value of 3.7. This event was also associated with an area-averaged 700-hPa temperature value of −6.5 °C, which corresponds to a value of the thermal metric, defined in section 3.2.2, of +0.5. This value of the thermal metric represents the mean value of the standardized area-averaged 700-hPa temperature anomaly for all days within the event. All of the days from the 5–7 June 2009 event correspond to the characteristic 300-hPa geopotential height pattern identified by SOMs node 3 (node 9 from Fig. 15) from group 3, consisting of a high-amplitude omega block ridge pattern over Greenland.

The 9–15 April 2016 event, randomly selected from the 90th percentile of standardized Greenland ice-melt events, was associated with three surface cyclones. One surface cyclone was initially located over western Canada on 0000 UTC 5 April 2016 and moved into Newfoundland and eventually to the Labrador Sea by 0000 UTC 16 April 2016. A second, quasi-stationary surface

cyclone located at the southern tip of Greenland was associated with 700-hPa poleward-directed warm-air advection over the southeastern coast of Greenland on 0000 UTC 8 April 2016. A third surface cyclone, which developed to the south of Nova Scotia, and the surface cyclone over the Labrador Sea were moving poleward and were concurrent with a blocking surface anticyclone over the North Atlantic on 0000 UTC 10 April 2016. A strong pressure gradient set up between the blocking surface anticyclone and the two poleward-moving cyclones to its west and was favorable for strong southerly flow concurrent with 700-hPa poleward-directed warm-air advection and larger positive 700-hPa standardized temperature anomaly values over all of Greenland relative to those in the previous case study. The standardized temperature anomaly values were concurrent with a standardized Greenland ice-melt anomaly reaching ~+5.7 sigma on 0000 UTC 12 April 2016 compared with the ~+1.1 sigma value from the previous case study on 1200 UTC 5 June 2016. The poleward-moving surface cyclones on 0000 UTC 10 April 2016 concurrent with the blocking surface anticyclone were associated with 300-hPa ridge amplification over Greenland. The evolution of the amplitude of the 300 hPa ridge was quantified in terms of sectorial sinuosity, which increased from 1.6 on 0000 UTC 8 to April 2016 to 2.5 on the first day of the standardized Greenland ice-melt anomaly event, on 0000 UTC 9 April 2016.

The amplitude of the 300-hPa flow pattern was characterized as medium, i.e., with sectorial sinuosity values between 2 and 3. This increase in sectorial sinuosity was associated with 300-hPa ridge amplification over southern Greenland, resulting in a flow pattern that is favorable for the transport of warm air poleward. Ridge amplification at 300 hPa was dominated by geopotential height tendency forcing from Term B, where negative values imply geopotential height rises. Negative values of Term B were located along the poleward side of the 300-hPa ridge located over Newfoundland and extending east into the North Atlantic on 0000 UTC 8 April 2016 and over the

Labrador Sea and extending over the western coast of Greenland on 0000 UTC 10 April 2016 leading up to 0000 UTC 12 April 2016 when the flow reaches its maximum amplitude corresponding to a sectorial sinuosity value of 2.5. This event is also associated with an area-averaged 700-hPa temperature value of −8.7 °C, which corresponds to a relatively high mean value of the thermal metric of +1.7 compared to events from the 10th percentile of standardized Greenland ice-melt anomaly where values of the thermal metric do not exceed +1 sigma. All of the days from the 9–15 April 2016 event correspond to the characteristic 300-hPa geopotential height pattern identified by SOMs node 3 (node 6 from Fig. 15) from group 2, consisting of a medium-amplitude trough–ridge pattern over Greenland.

Both events from chapter 4 show that 300-hPa ridge amplification over Greenland was dominated by geopotential height tendency forcing from Term B and are associated with flow patterns favorable for the transport of warm air poleward into Greenland. A main difference between the two events lies in the magnitude of the thermal advection and the value of the thermal metric. The 9–15 April 2016 event, from the 90th percentile of standardized Greenland ice-melt events, was associated with stronger poleward-directed warm-air advection of 0.7 °C h^{-1}, located ahead of the two surface cyclones in the Labrador Sea over the southwestern coast of Greenland and extending into central Greenland. Whereas the 5–7 June 2009 event from the 10th percentile of standardized Greenland ice-melt events, was associated with weaker poleward-directed warm-air advection ahead of the surface cyclone over the eastern coast of Newfoundland of 0.3 °C h^{-1}, located over the western coast of Greenland. Also, the 9–15 April 2016 event was associated with a thermal metric of +1.7 and a standardized 700-hPa temperature anomaly reaching +2 sigma over most of Greenland and +4 sigma over eastern Greenland. The 5–7 June 2009 event, from the 10th

percentile of standardized Greenland ice-melt events, was associated with a thermal metric of +0.5 and a standardized 700-hPa temperature anomaly reaching +1 sigma and extending over southern and eastern Greenland. The larger values of the thermal metric and the standardized 700-hPa temperature anomaly over Greenland from the 9–15 April 2016 event may be attributed to the stronger thermal advection. The stronger thermal advection was occurring ahead of two poleward-moving surface cyclones upstream of Greenland concurrent with a 700-hPa ridge over southeastern Greenland that is enhancing the poleward transport of warm air compared to one surface cyclone for the 5–7 June 2009 event concurrent with a 700-hPa ridge centered over southeastern Greenland, where the poleward transport of warm air was weaker.

REFERENCES

Barnes, E. A., and D. L. Hartmann, 2012: Detection of Rossby wave breaking and its response to shifts of the midlatitude jet with climate change. *Journal of Geophysical Research: Atmospheres*, **117**, doi:10.1029/2012jd017469.

——, and L. M. Polvani, 2015: CMIP5 Projections of Arctic Amplification, of the North American/North Atlantic Circulation, and of Their Relationship. *Journal of Climate*, **28**, 5254–5271, doi:10.1175/jcli-d-14-00589.1.

Bowley, K. A., E. H. Atallah, and J. R. Gyakum, 2018: Synoptic-Scale Zonal Available Potential Energy Increases in the Northern Hemisphere. *Journal of the Atmospheric Sciences*, **75**, 2385–2403, doi:10.1175/jas-d-17-0292.1.

——, J. R. Gyakum, and E. H. Atallah, 2019: A New Perspective toward Cataloging Northern Hemisphere Rossby Wave Breaking on the Dynamic Tropopause. *Monthly Weather Review*, **147**, 409–431, doi:10.1175/mwr-d-18-0131.1.

Box, J. E., and Coauthors, 2006: Greenland Ice Sheet Surface Mass Balance Variability (1988–2004) from Calibrated Polar MM5 Output*. *Journal of Climate*, **19**, 2783–2800, doi:10.1175/jcli3738.1.

Broeke, M. V. D., and Coauthors, 2009: Partitioning Recent Greenland Mass Loss. *Science*, **326**, 984–986, doi:10.1126/science.1178176.

Cullather, R. I., and S. M. J. Nowicki, 2018: Greenland Ice Sheet Surface Melt and Its Relation to Daily Atmospheric Conditions. *Journal of Climate*, **31**, 1897–1919, doi:10.1175/jcli-d-17-0447.1.

Fettweis, X., M. Tedesco, M. V. D. Broeke, and J. Ettema, 2011: Melting trends over the Greenland ice sheet (1958–2009) from spaceborne microwave data and regional climate models. *The Cryosphere*, **5**, 359–375, doi:10.5194/tc-5-359-2011.

Francis, J. A., and S. J. Vavrus, 2012: Evidence linking Arctic amplification to extreme weather in mid-latitudes. *Geophysical Research Letters*, **39**, doi:10.1029/2012gl051000.

Frauenfeld, O. W., 2003: Northern Hemisphere circumpolar vortex trends and climate change implications. *Journal of Geophysical Research*, **108**, doi:10.1029/2002jd002958.

Giuseppe Vettigli. (2018). MiniSom: minimalistic and NumPy-based implementation of the Self Organizing Map. *GitHub*. https://github.com/JustGlowing/minisom/. Accessed 12 April 2020

Hahn, L. C., T. Storelvmo, S. Hofer, R. Parfitt, and C. C. Ummenhofer, 2020: Importance of Orography for Greenland Cloud and Melt Response to Atmospheric Blocking. *Journal of Climate*, **33**, 4187–4206, doi:10.1175/jcli-d-19-0527.1.

Hanna, E., J. M. Jones, J. Cappelen, S. H. Mernild, L. Wood, K. Steffen, and P. Huybrechts, 2012: The influence of North Atlantic atmospheric and oceanic forcing effects on 1900-2010 Greenland summer climate and ice melt/runoff. *International Journal of Climatology*, **33**, 862–880, doi:10.1002/joc.3475.

Hanna, E., and Coauthors, 2013: Atmospheric and oceanic climate forcing of the exceptional Greenland ice sheet surface melt in summer 2012. *International Journal of Climatology*, **34**, 1022–1037, doi:10.1002/joc.3743.

Häkkinen, S., D. K. Hall, C. A. Shuman, D. L. Worthen, and N. E. Digirolamo, 2014: Greenland ice sheet melt from MODIS and associated atmospheric variability. *Geophysical Research Letters*, **41**, 1600–1607, doi:10.1002/2013gl059185.

Kapsch, M.-L., R. G. Graversen, and M. Tjernström, 2013: Springtime atmospheric energy transport and the control of Arctic summer sea-ice extent. *Nature Climate Change*, **3**, 744–748, doi:10.1038/nclimate1884.

Liu, C., and E. A. Barnes, 2015: Extreme moisture transport into the Arctic linked to Rossby wave breaking. *Journal of Geophysical Research: Atmospheres*, **120**, 3774–3788, doi:10.1002/2014jd022796.

Liu, J., J. A. Curry, H. Wang, M. Song, and R. M. Horton, 2012: Impact of declining Arctic sea ice on winter snowfall. *Proceedings of the National Academy of Sciences*, **109**, 4074–4079, doi:10.1073/pnas.1114910109.

Martin, J. E., S. J. Vavrus, F. Wang, and J. A. Francis, 2016: Sinuosity as a measure of middle tropospheric waviness. http://marrella.aos.wisc.edu/SIN_paper_JCLIM_FIN.pdf

Martius, O., C. Schwierz, and H. C. Davies, 2007: Breaking Waves at the Tropopause in the Wintertime Northern Hemisphere: Climatological Analyses of the Orientation and the Theoretical LC1/2 Classification. *Journal of the Atmospheric Sciences*, **64**, 2576–2592, doi:10.1175/jas3977.1.

Mioduszewski, J. R., A. K. Rennermalm, A. Hammann, M. Tedesco, E. U. Noble, J. C. Stroeve, and T. L. Mote, 2016: Atmospheric drivers of Greenland surface melt revealed by self-organizing maps. *Journal of Geophysical Research: Atmospheres*, **121**, 5095–5114, doi:10.1002/2015jd024550.

Mote, T. L., and M. R. Anderson, 1995: Variations in snowpack melt on the Greenland ice sheet based on passive-microwave measurements. *Journal of Glaciology*, **41**, 51–60, doi:10.1017/s0022143000017755.

——, 2007: Greenland surface melt trends 1973–2007: Evidence of a large increase in 2007. *Geophysical Research Letters*, **34**, doi:10.1029/2007gl031976.

Neff, W., G. P. Compo, F. M. Ralph, and M. D. Shupe, 2014: Continental heat anomalies and the extreme melting of the Greenland ice surface in 2012 and 1889. *Journal of Geophysical Research: Atmospheres*, **119**, 6520–6536, doi:10.1002/2014jd021470.

Nghiem, S. V., and Coauthors, 2012: The extreme melt across the Greenland ice sheet in 2012. *Geophysical Research Letters*, **39**, doi:10.1029/2012gl053611.

Oliveira, J. C., E. Zorita, V. Koul, T. Ludwig, and J. Baehr, 2020: Forecast opportunities for European summer climate ensemble predictions using Self-Organising Maps. *Proceedings of the 10th International Conference on Climate Informatics*, doi:10.1145/3429309.3429319.

Rivière, G., 2011: A Dynamical Interpretation of the Poleward Shift of the Jet Streams in Global Warming Scenarios. *Journal of the Atmospheric Sciences*, **68**, 1253–1272, doi:10.1175/2011jas3641.1.

Screen, J. A., and I. Simmonds, 2010: The central role of diminishing sea ice in recent Arctic temperature amplification. *Nature*, **464**, 1334–1337, doi:10.1038/nature09051.

Sherman, P., E. Tziperman, C. Deser, and M. Mcelroy, 2020: Historical and Future Roles of Internal Atmospheric Variability in Modulating Summertime Greenland Ice Sheet Melt. *Geophysical Research Letters*, **47**, doi:10.1029/2019gl086913.

Solomon, A., M. D. Shupe, and N. B. Miller, 2017: Cloud–Atmospheric Boundary Layer–Surface Interactions on the Greenland Ice Sheet during the July 2012 Extreme Melt Event. *Journal of Climate*, **30**, 3237–3252, doi:10.1175/jcli-d-16-0071.1.

Sprenger, M., and Coauthors, 2017: Global Climatologies of Eulerian and Lagrangian Flow Features based on ERA-Interim. *Bulletin of the American Meteorological Society*, **98**, 1739–1748, doi:10.1175/bams-d-15-00299.1.

Strong, C., and G. Magnusdottir, 2008: How Rossby wave breaking over the Pacific forces the North Atlantic Oscillation. *Geophysical Research Letters*, **35**, doi:10.1029/2008gl033578.

——,and——, 2008: Tropospheric Rossby Wave Breaking and the NAO/NAM. *Journal of the Atmospheric Sciences*, **65**, 2861–2876, doi:10.1175/2008jas2632.1.

Tang, Q., X. Zhang, and J. A. Francis, 2013: Extreme summer weather in northern mid-latitudes linked to a vanishing cryosphere. *Nature Climate Change*, **4**, 45–50, doi:10.1038/nclimate2065.

Tedesco, M., X. Fettweis, T. Mote, J. Wahr, P. Alexander, J. E. Box, and B. Wouters, 2013: Evidence and analysis of 2012 Greenland records from spaceborne observations, a regional climate model and reanalysis data. *The Cryosphere*, **7**, 615–630, doi:10.5194/tc-7-615-2013.

Vaughan, D. G., and Coauthors, 2013: Observations: Cryosphere. Climate Change 2013: The Physical Science Basis, T. F. Stocker et al., Eds., Cambridge University Press, 317–382.

Vellinga, M., and R. A. Wood, 2007: Impacts of thermohaline circulation shutdown in the twenty-first century. *Climatic Change*, **91**, 43–63, doi:10.1007/s10584-006-9146-y.

Woods, C., R. Caballero, and G. Svensson, 2013: Large-scale circulation associated with moisture intrusions into the Arctic during winter. *Geophysical Research Letters*, **40**, 4717–4721, doi:10.1002/grl.50912.

Woollings, T., B. Hoskins, M. Blackburn, and P. Berrisford, 2008: A New Rossby Wave–Breaking Interpretation of the North Atlantic Oscillation. *Journal of the Atmospheric Sciences*, **65**, 609–626, doi:10.1175/2007jas2347.1.

Yang, W., and G. Magnusdottir, 2017: Springtime extreme moisture transport into the Arctic and its impact on sea ice concentration. *Journal of Geophysical Research: Atmospheres*, **122**, 5316–5329, doi:10.1002/2016jd026324.